Erasmus Mundus Programme
M.Sc. programme in
Coastal and Marine Management

CoMEM

Freeze-bond strength

Analysis of experiments and FE modeling of a shear test on freeze bonds

Ekaterina Kim

July 2009

Thesis work done at NTU

The Erasmus Mundus Master in Coastal and Marine Engineering and Management (CoMEM) is a two-year, English taught international Master's programme, in which five high-rated European universities participate. Focus is on the key issues involved in providing sustainable, environmentally friendly, legally and economically acceptable solutions to various problems in the CoMEM field.

The CoMEM MSc course is taught at five European universities:

* NTNU, Trondheim, Norway
* Delft Technical University, Delft, The Netherlands
* UPC, Barcelona, Spain
* City University, London, United Kingdom
* University of Southampton, Southampton, United Kingdom

The first year comprises two semesters of 30 ECTS each (course and project work), which will be spent at NTNU,Trondheim and Delft University respectively. This year provides academic and social coherence through a choice of compulsory and optional courses. It will establish a broad common foundation and prepare for the final year.

For the first half of the second year (one semester of 30 ECTS course and project work), three main routes with a particular emphasis are offered: either in environmental engineering at UPC, Barcelona, Spain, in environment and management at City University, London, or in business and management at the University of Southampton, Southampton, both in the United Kingdom. The third semester allows for specialisation in one of these three subjects. In the fourth and final semester a master's thesis at one of the three universities has to be made. The CoMEM programme therefore offers the following posibilities as illustrated in the diagram below:

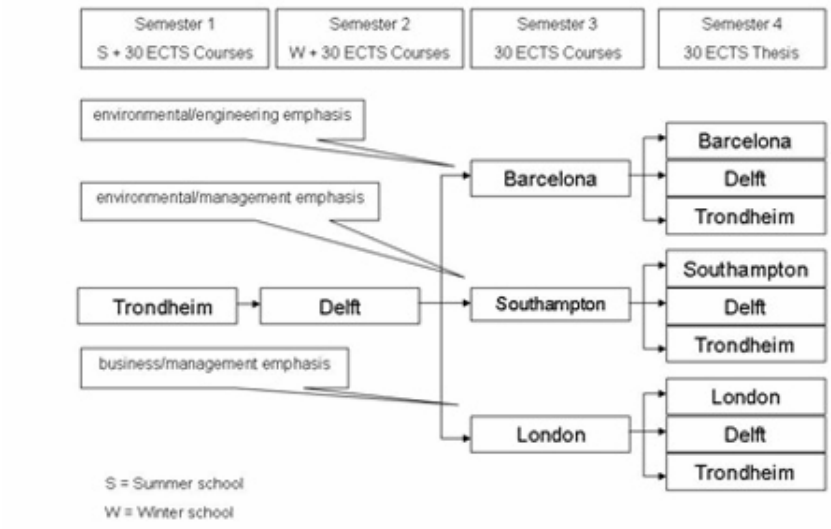

Information regarding the CoMEM programme can be obtained from the programme director'
prof.dr. Marcel J.F. Stive
Delft University of Technolgoy
Faculty of Civil Engineering and Geosciencese
PO Box 5048
2600 GA Delft
The Netherlands
comem@tudelft.nl

Ekaterina Kim

Freeze-Bond Strength. Analysis of Experiments and FE Modeling of a Shear Test on Freeze-Bonds

Trondheim, June 2009

Master´s thesis

NTNU
Norwegian University of
Science and Technology
Faculty of Engineering Science and Technology
Department of Civil and Transport Engineering

Ekaterina Kim

Freeze-Bond Strength

Analysis of Experiments and FE Modeling of a Shear Test on Freeze-Bonds

Master's thesis

Trondheim, June 2009

Norwegian University of Science and Technology
Faculty of Engineering Science and Technology
Department of Civil and and Transport Engineering

Academic supervisor: Sveinung Løset, Knut V. Høyland

NTNU
Norwegian University of
Science and Technology

NORWEGIAN UNIVERSITY OF SCIENCE AND TECHNOLOGY
DEPARTMENT OF CIVIL AND TRANSPORT ENGINEERING

THE UNIVERSITY CENTRE IN SVALBARD
DEPARTMENT OF ARCTIC TECHNOLOGY

Report Title: **Freeze-Bond Strength. Analysis of Experiments and FE Modeling of a Shear Test on Freeze-Bonds**	Date: 2009-JUNE-15 Number of pages (incl. appendices): 128			
	Master Thesis	X	Project Work	
Name: Ekaterina Kim				
Professor in charge/supervisor: Prof. Sveinung Løset, Dr. Knut V. Høyland				
Other external professional contacts/supervisors:				

Abstract:

The objective of this study was to contribute to the knowledge on ice-ridges structures interactions. This work is a follow-up of previous research on simulations of ice-structure interaction using finite element method (Gürtner, 2009b; Konuk, et al., 2009a,b) and a preliminary study of freeze-bond (FB) shear strength (Repetto-Llamazares, et al., 2009b). The presented data should be regarded as illustrative rather than exhaustive. Many important aspects of ice-ridges structures interactions have not been addressed in this thesis.

An analysis of experiments with FBs was performed, and a finite element model was built in order to simulate these experiments. Within the framework of the classical theory of elasticity, the numerical model incorporates a cohesive model in order to simulate ice fracture along the FB during shear test. The cohesive behavior of the FB was described by the bilinear traction-separation law. The approach of Camanho and Davila (2002) was applied in order to calculate stresses in the FB under mixed-mode loading conditions. A 6-node cohesive finite element was used for implementation of assumed behavior of the FB. Information obtained via detailed analysis of the FB shear strength experiments and via their numerical simulation can be used for a better understanding of FB failure processes and for a numerical modeling of ice-ridges.

The results of numerical simulation confirmed that the finite element model could reproduce phenomena commonly observed in actual shear tests of FBs, including the shear strength hardening and partly softening behavior. The peak load in simulations was completely determined by the maximum traction strength and the initial part of a traction-separation law. This study also showed that from the conducted experiments intended to study FB strength in model ice, it is also possible to study ice fracture processes as well as post-failure behavior. By improving the experimental procedure as described in Repetto-Llamazares, et al. (2009b) it will be possible to study not only FB shear strength but also the frictional behavior of ice after the FB failure. By video monitoring of the crack initiation and growth it will be possible to study a fracture process inside the FB. This work is of appeal to different scientists actively participating in investigations in, and possibly also on the standardization of methods for, measuring strength of freeze-bonds in order to improve existing analytical and numerical models, which are used nowadays for calculation of loads for scenarios of ice-ridges interactions with structures.

Keywords:

1. ice-ridges
2. freeze-bond
3. finite element modeling
4. cohesive zone model

(signature)

Norwegian University of Science and Technology
Faculty of Engineering Science and Technology
Department of Civil and and Transport Engineering

NTNU

Postal adress

Høgskoleringen 7a
7491 Trondheim
Telephone +47 73 59 46 40
Telefax +47 73 59 70 21

The University Centre in Svalbard
Department of Arctic Technology

UNIS

Postal adress

P.O. Box 156
N-9171 Longyearbyen
Telephone +47 79 02 33 00
Telefax +47 79 02 33 01

MASTER DEGREE THESIS
Spring 2009
for
Student: Ekaterina Kim

Freeze-Bond Strength. Analysis of Experiments and FE Modeling of a Shear Test on Freeze-Bonds

Background

When two ice sheets interact with each other, they may form a new ice feature called *an ice-ridge*. Large ice-ridges can be a significant problem for navigation; they can also control the design load levels for sea-ice interactions with offshore structures. Besides they can scour the sea floor in relatively shallow waters. Despite the fact that ice-ridges play an important role in planning of a structure in ice infested waters, both properties of ice-ridges and their failure processes are poorly investigated. There is no consensus among researchers either on which method to use for estimating ice loads on structures or on which parameters of the ice-ridge are important during ice-ridge failure. Previous research showed that *freeze-bonds* (newly created ice between adjoining ice pieces due to thermodynamic processes in the ice-ridge) contribute to the peak value of load at failure of the ice-ridge. Recently Konuk, et al. (2009a) proposed a framework for studying the ice-ridge structure interactions, which takes into account the effect of freeze-bonds via use of cohesive zone models within the conventional finite element method. For the future development of this modelling technique and any other analytical or numerical models, taking into consideration the effect of freeze-bonds, both experimental studies of freeze-bonds and numerical simulations, validating material properties of freeze-bonds are needed.

Task description

The objective of the work is to contribute to knowledge on ice-ridge interactions with structures, focusing mainly on the behaviour of freeze-bonds under shear conditions and trying to incorporate knowledge from previous experiments of Repetto-Llamazares,

et al. (2009b) into a finite element model using ABAQUS version 6.8 with a study on the capability of the software to model ice fracture.

General about content, work and presentation

The text for the master thesis is meant as a framework for the work of the candidate. Adjustments might be done as the work progresses. Tentative changes must be done in cooperation and agreement with the supervisor and professor in charge at the Department. (Also including external cooperative partners where this is applicable).

The norm for the work load of this thesis work is defined as 30 studypoints (ECTS). The work must be completed within 21 weeks (Easter included).

In the evaluation thoroughness in the work will be emphasized, as will be documentation of independence in assessments and conclusions. Furthermore the presentation (report) should be well organized and edited; providing clear, precise and orderly descriptions without being unnecessary voluminous.
The report shall include:

→ Standard report front page.
Title page with abstract and keywords (signed by the student).
Text of the Thesis (these pages) signed by professor in charge.

→ Summary and acknowledgement. Table of content including list of figures, tables, enclosures and appendices. If useful and applicable a list of important terms and abbreviations should be included. List of symbols is strongly recommended.

→ The main text.

→ Clear and complete references to material used, both in text and figures/tables. This also applies for personal and/or oral communication and information.

→ The report musts have a complete page numbering.

Advice and guidelines for writing of the report is given in: "Writing Reports" by Øivind Arntsen. Additional information on report writing is found in "Råd og retningslinjer for rapportskriving ved prosjekt og masteroppgave ved Institutt for bygg, anlegg og transport" (in Norwegian) posted on http://www.ntnu.no/bat/skjemabank.

Submission procedure

- The complete, original report (un-bounded).
- Three copies (bounded).
- If applicable: X additional copies if agreed upon for instance with external partner (to be paid for by the Department or the external partner)
- CD with the complete report (pdf-format) and all assisting or underlying material.
- A brief (one to two A4 pages including possible illustrations) popular science summary of the work, on the *MSc_web* template (found on It's-learning subject

TBA4290) - aiming at publication on the Department's web-page. Include a copy of this html document on the CD.

The summary shall include the objectives of the work, explain how the work has been conducted, present the main results achieved and give the main conclusions of the work.

Documentation collected during the work, with support from the Department, shall be handed in to the Department together with the report.

According to the current laws and regulations at NTNU, the report is the property of NTNU. The report and associated results can only be used following approval from NTNU (and external cooperation partner if applicable). The Department has the right to make use of the results from the work as if conducted by a Department employee, as long as other arrangements are not agreed upon beforehand.

Tentative agreement on external supervision, work outside NTNU, economic support etc

Separate description to be developed, if and when applicable.

Health, environment and safety (HMS)

NTNU emphasizes the safety for the individual employee and student. The individual safety shall be in the forefront and no one shall take unnecessary chances in carrying out the work. In particular, if the student is to participate in field work, visits, field courses, excursions etc. during the Master Thesis work, he/she shall make himself/herself familiar with "*Feltarbeid HMS retn.linje*" (This is in Norwegian, and shall be explained to the student if applicable). The document is found on the NTNU HMS-pages http://www.ntnu.no/adm/hms/handbok/retningslinjer

The students do not have a full insurance coverage as a student at NTNU. If you as a student want the same insurance coverage as the employees at the university, you must take out individual travel and personal injury insurance.

Start and submission deadlines

The work on the Master Thesis starts on January 19, 2009
The thesis report as described above shall be submitted at the latest on June 15, 2009

Professor in charge: Sveinung Løset
Other supervisors: Dr. Knut V. Høyland

_____
(signature)
Prof. Sveinung Løset
Department of Civil and Transport Engineering

"...If I had my way for the world to end in fire or ice,
It seems that ice would be the compromise..."

Orli A.

ACKNOWLEDGMENTS

I would like to thank the Norwegian University of Science and Technology for giving me a chance to work on this interesting and challenging research topic, especially Prof. Sveinung Løset and Dr. Knut V. Høyland for their hospitality and support during the period of this study.

I deeply thank PhD student Ada Repetto-Llamazares and Dr. Jenny Trumars for their great help and advice and with whom it has been a pleasure to work.

I also thank Prof. Mauri Määttänen for his comments regarding history of ice-structure interactions; Prof. Thomas Benz for the discussion of ABAQUS capabilities in ice modeling; Dr. Arne Gürtner and PhD student Jani Paavilainen for their advice regarding cohesive zone model and Master student Gurvinder Singh for his technical help.

Special thanks to Dr. Vigdis Olden, Nicolas Serre, Raed Lubbad, Haiyan Long and Siddharth Narayan without whom this work could not be completed.

Finally thanks to Ice that made this research possible.

CONTENTS

Abstract i
Acknowledgments ix
Contents xi
List of figures xiii
List of tables xvii
List of abbreviations and symbols xix

INTRODUCTION 1

General 1
Objective and organization of the thesis 3
Limitations of the thesis 3

THEORY AND METHODS 4

1.1 Overview of Ice - Ridges Structure Interaction 4
1.1.1 General 4
1.1.2 Ice-ridge structure interaction 6
1.1.3 Uncertainty summary 12
1.2 Importance of Freeze-bonds (Theory) 13
1.2.1 General 13
1.2.2 FB creation, FB importance 14
1.2.3 Uncertainty summary 18
1.3 Finite Element Method in Ice-ridges Structure Interaction (Theory) 19
1.3.1 General 20
1.3.2 Background and basic equations of finite element method 26
1.3.3 Formulation of cohesive model in ABAQUS 29
1.3.4 ABAQUS solution to finite element equations 33
1.4 Analysis of Freeze-Bond Shear Strength Experiments 37
1.4.1 Experiment description 37
1.4.2 Ice characteristics 39
1.5 Finite Element Modeling of the Freeze-bond Shear Strength Experiments 39
1.5.1 Initial data 39
1.5.2 Finite element model 41

RESULTS 48

2.1 Analysis of Freeze-bond Shear Strength Experiments 48
2.1.1 Freeze-bond shear strength 48
2.2.2 Failure type 49

2.2.3 F(t) behavior (as visual observation) 56
2.2.4 Post-peak force 58
2.2.5 Fracture energy 65
2.2 Numerical Results of the Freeze-bond Shear Strength Simulations 70
3.2.1 Three-dimensional model (3 elements) 70
3.2.2 Considerations on the effect of the problem formulation 71
3.2.3 Influence of the boundary conditions 74
3.2.4 Influence of the finite element mesh 75
3.2.5 Effect of the material parameters on the fracture behavior 77

ANALYSIS AND DISCUSSION **84**

3.1 Freeze-Bond Shear Strength 84
3.1 Ice-Ice Friction in Freeze-Bonds 85
3.2 Analysis of Uncertainties 89
3.2.1 Experimental uncertainties 89
3.2.2 Model ice uncertainties 90
3.2.3 Stick-sleep behavior or effect of the sampling frequency 90
3.2.4 FB development as a function of submersion time and temperature 92
3.2.5 Uncertainties of finite element model 93
3.3 Model Ice and Freeze-bond Failure Mode 93
3.4 Numerical Simulations 94
3.5 Modeling of Ice-ridge Structure Interactions 97
3.6 Summary 98

CONCLUSIONS and RECOMMENDATIONS for FUTURE WORK **100**

4.1 Conclusions 100
4.1 Recommendations for Future Work 101

REFERENCES **103**

APPENDIX **112**

A - History of the Freeze-Bond Experimental Setup A1
B - Estimated Parameters B1
C1 - Power-Law Fit C1
C2 - Post-failure Behavior C1
D1 - Cohesive Element Verification D1
D2 - Input Files D4
E - Scheme for Predicting Ice Loads on Structure E1
F - Data Normality Test F1

LIST OF FIGURES

Figure 1 - The first icebreakers 1

Figure 1.1 - Geometry of a first year ridge 4

Figure 1.2 - Interlocking effect and spatial orientation of ice blocks 6

Figure 1.3 - Predictions for scenario of a first-year ridge interacting with a structure .. 7

Figure 1.4 - Main elements of a numerical simulation 10

Figure 1.5 - Development state. 12

Figure 1.6 - Qualitative forms of the Mohr-Coulomb diagram 14

Figure 1.7 - Scheme of freezing over an ice block 15

Figure 1.8 - Scheme for estimating ice block temperature variation with time 16

Figure 1.9 - Temperature of ice as a function of time 16

Figure 1.10 - Increase of volume as a function of temperature 17

Figure 1.11 - Scheme of frozen together spheres 17

Figure 1.12 - A crack model 24

Figure 1.13 - A cohesive zone 24

Figure 1.14 - Cohesive laws adopted for the modeling of ice failure 25

Figure 1.15 - A mixed-mode softening law 31

Figure 1.16 - A traction-separation law 31

Figure 1.17 - The procedure of the frontal solution algorithm 34

Figure 1.18 - The procedure of the multifrontal solution algorithm 34

Figure 1.19 - Scheme of how the ice blocks were loaded during submersion 38

Figure 1.20 - Vertical thin section of a consolidated layer 40

Figure 1.21 - Geometry of the tested ice sample. 40

Figure 1.22 - Model of tested ice sample with solid parts and a cohesive layer. 41

Figure 1.23 - Tuning procedure of CE stiffness 42

Figure 1.24 - Tuning procedure of CE maximum traction 42

Figure 1.25 - Tuning procedure of cohesive fracture energy 43

Figure 1.26 - Geometry of the element COH2D4 44

Figure 1.27 - Geometry of the element COH3D8 and C3D8 44

Figure 1.28 - Geometry of the elements CPE4 and CPS4 45

Figure 1.29 - Three-dimensional finite element model used to simulate shear test 45

Figure 1.30 - Two-dimensional finite element model used to simulate shear test. 46

Figure 2.1 - Freeze-bond shear strength distribution. 48

Figure 2.2 - Representative plot of curves obtained when testing freeze-bonds 51

Figure 2.3 - Shear strength of freeze-bonds as a function of normal pressure 52

Figure 2.4 - Temperature dependence of averaged shear capacity 53

Figure 2.5 - Averaged shear capacity versus time for ductile fractures 53

Figure 2.6 - Averaged shear capacity versus normal pressure for brittle fractures 54

Figure 2.7 - Distribution of approximated loading slope. 54

Figure 2.8 - Summary of the obtained results for the ductile samples 55

Figure 2.9 - Typical types of *F(t)* behavior 57

Figure 2.10 - Measured force versus time 57

Figure 2.11 - Post-failure behavior of ice samples from series 10140 58

Figure 2.12 - A summary of the obtained results of series 10100 and 10200 59

Figure 2.13 - Ice-ice friction coeffisient similitude versus time and normal pressure 60

Figure 2.14 - Ice-ice friction coefficient similitude as a function of time (13_17_1) 60

Figure 2.15 - Relation between the post-peak shear stress and the normal stress 62

Figure 2.16 - Coulomb friction coefficient and cohesion 62

Figure 2.17 - Internal friction coefficient and cohesion 63

Figure 2.18 - Shear stress versus normal pressure 64

Figure 2.19 - Energy evolution with time for ductile sample 13_17_1 66

Figure 2.20 - Summary obtained for the ductile samples. 67

Figure 2.21 - Grouped plot matrix 68

Figure 2.22 - A bivariate joint frequency distribution 69

Figure 2.23 - A bivariate joint frequency distribution for ductile samples. 69

Figure 2.24 - Area under the curve $F(t)$ versus post-peak force (ductile samples) 70

Figure 2.25 - A force history during experiment and during simulations. 71

Figure 2.26 - A finite element model for the pure shear test. 72

Figure 2.27 - Static versus dynamic analysis. 73

Figure 2.28 - Numerical solution 74

Figure 2.29 - Finite element discretizations. 75

Figure 2.30 - Influence of the finite element mesh on the reaction force 76

Figure 2.31 - von Mises stress 76

Figure 2.32 - A plot of effects for F_{max}. 79

Figure 2.33 - A plot of effects for $t(F_{max})$. 79

Figure 2.34 - A plot of effects for S_l'. 80

Figure 2.35 - Interaction plot of E versus K*. 81

Figure 2.36 - Effect of cohesive element stiffness on loading slope. 82

Figure 2.37 - Effect of maximum traction on maximum load. 82

Figure 2.38 - Effect of fracture energy on evolution of reaction force in time. 83

Figure 3.1 - Force versus time at the beginning of deformation (Sample 13_17_1) 90

Figure 3.2 - Force versus time, one second prior to failure (Sample 13_17_1) 91

Figure 3.3 - Force amplitude versus time 91

Figure 3.4 - Hypothetic development of freeze-bond strength 92

Figure 3.5 - A force measured during freeze-bond shear experiments (1_13kg_2) 97

LIST OF TABLES

Table 1.1 - Parameters used in each experiment 38

Table 1.2 - Properties of HSVA ice..... 39

Table 1.3 - Elastic material properties 41

Table 1.4 - Finite elements used in numerical simulations..... 43

Table 2.1 - Distribution parameters. 49

Table 2.2 - Unloading slope data 52

Table 2.3 - Change in the percentage of brittle and ductile samples..... 56

Table 2.4 - Estimated parameters. 68

Table 2.5 - Summary of problem size 75

Table 2.6 - List of factors and their ranges for the numerical experiments. 77

Table 2.7 - Uncoded design matrix with response values 78

Table 3.1 - Comparative table 86

Table 3.2 - Fracture properties of ice in assumption of cohesion zone model 95

Note: Tables and Figures in appendixes does not included in the Lists above.

LIST OF ABBREVIATIONS AND SYMBOLS

Abbreviations

API RP	American Petroleum Institute, Recommended Practice
BFGS	Broyden, Fletcher, Goldfarb, Shanno method
CE	Cohesive Element
CERN	European Organization for Nuclear Research
CSA	Canadian Standards Association
CZM	Cohesive Zone Model
DEM	Discrete Element Method
DNV	Det Norske Veritas
DOF	Degree of Freedom
DS	Danish Standards
FB	Freeze Bond
FE	Finite Element
FEM	Finite Element Method
FETI	Finite Element Tearing and Interconnecting
FZP	Fracture Process Zone
GLO	Germanischer Lloyd (Rules for Offshore Installations)
HSVA	Hamburgische Schiffbau-Versuchsanstalt (Hamburg Ship Model Basin)
IALA	International Association of Lighthouse Authorities
IEC	International Electrotechnical Commission
ISO	International Organization for Standardization
NDP	Norwegian Petroleum Directorate
NORSOK	Norsk Sokkels Konkuranseposisjon (The Competitive Standing of the Norwegian Offshore Sector)
NPP	Normal Probability Plot
PCG	Preconditioned Conjugate Gradient
PDE	Partial Differential Equations
PIC	Particle in Cell method
Q/HSn	Chinese Code
RIL	Suomen Rakennusinsinööorien Liitto (Finnish Association of Civil Engineers)
SniP	Stroitelnie Normi i Pravila (Construction Norms and Regulations)
TSL	Traction-Separation Law
VSN	Vedomstvennye Stroitelnie Normi (Industry Building Code)
2D	Two-dimensional
3D	Three-dimensional

Scalar quantities

a, b	coefficients of the freeze-bond shear model
c_p	heat capacity of ice

d	damage evolution function
$f_{Vk}, k = 1,2,3$	component of a body force vector along the direction k
h	thickness of ice
h_c	thickness of a consolidated layer
h_{fb}	freeze-bond thickness
h_k	keel depth
h_s	sail height
n	number of data points
n_e	number of finite elements
n_p	number of nodes
r_{fb}	surface radius
r^2	measure of reliability of a linear relationship
t	time
t_f	failure time, corresponding to a peak force
t_{sf}	start time of a failure process
$u_k, k = 1,2,3$	component of a displacement vector along the direction k
v	velocity
$x_k, k = 1,2,3$	component of a radius-vector along the direction k

A	area under the loading curve
A_{fb}	freeze-bond contact area
C	cohesive intercept (cohesion)
C_{fb}	cohesion due to freeze-bonding forces
C_i	cohesion due to interlocking
C_s	shear resistance in the ridge model
E	elastic modulus
F	force registered during freeze-bond experiments
$F1$	post-peak force
F_b	buoyancy force
F_f	frictional force during sliding of de-bonded ice samples
F_{fb}	freeze-bond force
F_{load}	force exerted by the weight on the top of ice
F_{max}	maximum reaction force in a numerical simulation
F_n	normal force
F_N	confining load in the ridge model
F_p	peak force
F_T	force resisting to shear in the ridge model
F_{wi}	total weight of ice

F_{wp}	weigh of the wooden plate
I_1	first invariant
K^*	cohesive-element penalty stiffness
L	latent heat of sea ice
N	reaction force
Q	cold energy
R	radius of an ice block
R_c	freeze-bond compressive strength
R_s	freeze-bond shear strength
R_t	freeze-bond tensile strength
S	surface
S_u	unloading slope
S_l'	loading slope
S_{cr}	critical unloading slope
S_{cr}'	critical loading slope
S_1, S_2	parts of a surface
T	cohesive-element traction
T_{av}	average ice temperature
$T_i, i = N, S, T$	traction stresses in the direction i
T_0	maximum traction
T_{0eff}	effective traction at the damage initiation
$T_{0i}, i = N, S, T$	maximum traction in the direction i
$\overline{T}_i, i = N, S, T$	stress component in the direction i predicted by elastic traction-separation behavior for strains without damage
U	total potential energy
U_a	elastic energy caused by introducing a crack in the plate
U_0	elastic energy of the uncracked plate
U_γ	elastic energy caused by formation of crack surfaces
V	volume
V_S	sliding velocity

α, β, γ	parameters of the Hilber-Hughes-Taylor operator
γ_{fb}	freeze-bond shear strain
δ	separation
δ_m^d	mixed-mode effective displacements corresponding to the damage initiation
δ_m^{max}	maximum mixed-mode separation

δ_N	normal separation
δ_p	thickness of the an additional ice layer
δ_T, δ_S	tangential separations
δ_{ij}	Kronnecker delta
δU	change in potential energy
δ_0	critical separation
δ_m	effective displacement
δ_{0m}	effective displacement, corresponding to complete failure of a cohesive element
η_k	keel porosity
θ	melting temperature of ice
θ_k	keel angle
λ	thermal conductivity of an ice block
μ	coefficient of friction
μ^*	friction coefficient similitude
μ_0^*, z	constants of the frictional model
ν	Poisson's ratio
ξ	tolerance in an iteration method
ρ	density
ρ_i	sea ice density
σ	confining pressure
τ	shear strength
τ_i	temperature
τ_{fb}	freeze-bond shear stress
τ_{ice}	shear strength of ice in the discrete model of an ice-ridge
υ	salinity
ϕ	angle of internal friction
ϕ_i	angle of internal friction of ice
ϕ_r	angle resisting to shear in the ridge model
χ_1, χ_2	separation measures
Γ^C	critical mixed-mode energy
$\Gamma_N, \Gamma_T, \Gamma_S$	work done by the traction and its conjugate relative displacement in the normal, the first, and the second shear directions, respectively
Γ_0	cohesive energy
$\Gamma_{0N}, \Gamma_{0T}, \Gamma_{0S}$	critical fracture energies required to cause failure in the normal, the first, and the second shear directions, respectively.
Ω	area

Vector and tensor notation

$\boldsymbol{a}_f^{(ce)}$	transformation tensor in a cohesive crack model
$\boldsymbol{a}_f^{(e)}, \boldsymbol{a}_g^{(e)}$	incidence matrix (connectivity matrix)
$\boldsymbol{e}_k, k = 1,2,3$	orthogonal unit vectors (base vectors)
$\boldsymbol{f}_S$	vector of surface forces
$\boldsymbol{f}_V$	vector of body forces
$\boldsymbol{f}_V^{(e)}, \boldsymbol{f}_S^{(e)}$	vectors of nodal forces
$\boldsymbol{f}_{\varepsilon_0}^{(e)}, \boldsymbol{f}_{\sigma_0}^{(e)}$	vectors of nodal forces
$\boldsymbol{k}$	element stiffness matrix
$\boldsymbol{k}^{(ce)}$	cohesive element stiffness matrix
$\boldsymbol{n}$	unit vector of the outward pointing normal to a body surface
$\boldsymbol{r}$	radius-vector of a point (position vector)
$\boldsymbol{rs}$	residual vector in the Newton's method
$\boldsymbol{r}_n$	vector in an iteration method
$\boldsymbol{u}$	displacement vector
$\boldsymbol{u}^{(ce)}$	vector of cohesive-element nodal displacements
$\boldsymbol{u}^{(e)}$	local vector of nodal unknowns of an element
$\boldsymbol{u}_S$	displacement vector prescribed on a boundary
$\boldsymbol{u}^+$	displacement vector of top nodes
$\boldsymbol{u}^-$	displacement vector of bottom nodes
$\boldsymbol{x}$	position vector of an arbitrary point of a finite element
$\boldsymbol{x}^{(e)}$	coordinate vector of finite element nodes

$\boldsymbol{B}^{(ce)}, \boldsymbol{B}^{(e)}$	matrix, defining strains from nodal variables
${}^4\boldsymbol{C}$	fourth - rank tensor of a material stiffness
$\boldsymbol{D}^{(ce)}$	constitutive matrix of a cohesive element
$\boldsymbol{D}^{(e)}$	elasticity matrix containing material properties
$\boldsymbol{F}$	global vector of nodal forces
$\boldsymbol{G}$	transition matrix in an iterative method
$\boldsymbol{I}$	unit tensor
$\boldsymbol{J}$	Jacobi matrix
$\boldsymbol{K}$	global stiffness matrix
$\boldsymbol{L}$	sum of all Lagrange multiplier forces
$\boldsymbol{M}$	mass matrix
$\boldsymbol{N}^{f(e)}$	matrix of finite-element shape functions
$\boldsymbol{N}^{f(ce)}$	matrix of cohesive-element shape functions

$\boldsymbol{N}^{g(e)}$	matrix of finite-element approximate functions
${}^{4}\boldsymbol{S}$	fourth-rank tensor of the elastic complaisance
$\boldsymbol{T}$	vector of cohesive-element tractions
$\boldsymbol{U}$	displacement vector in global coordinates
$\boldsymbol{X}$	global coordinate vector
$\boldsymbol{\delta}$	vector of cohesive-element separations in local coordinates
$\delta\boldsymbol{u}$	vector of infinitesimal displacement increments
$\boldsymbol{\varepsilon}$	strain tensor
$\boldsymbol{\varepsilon}_0$	vector of initial strains
$\boldsymbol{\sigma}$	stress tensor
$\boldsymbol{\sigma}_0$	vector of initial stresses
Δ	vector of cohesive-element separations in global coordinates

INTRODUCTION

"... The ice was here, the ice was there,
The ice was all around:
It cracked and growled, and roared and howled,
Like noises in a swound! ..."

Samuel Taylor Coleridge
"The Rime of the Ancient Mariner", 1797–98

General

The history of ice-structure[1] interaction probably dates back to the times when engineers were involved with design of the research vessel *Fram* as it is mentioned by Gürtner (2009b). The first Finnish icebreaker *Murtaja* (Figure 1a) was built in 1890. Before that, winter navigation between Finland and Sweden had been started by *Express II* in 1877 as mentioned by Prof. M. Määttänen (personal communication, 2009). The first Russian icebreaker *Pilot* (Figure 1b) was built in 1864 by the bow conversion of the steam-powered propeller tug ("Pilot (Icebreaker)," Wikipedia, 2009).

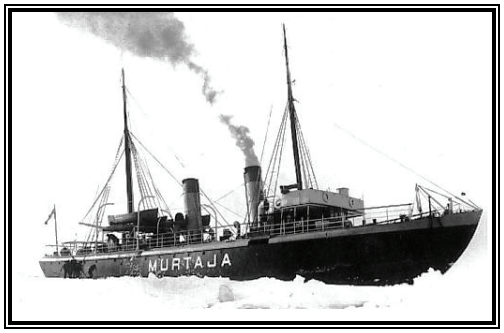

(a) (Brady, 2009)

(b) ("Jaanmurtajien historia," Wikipedia, 2009)

Figure 1 - The first icebreakers in Finland (a) and in Russia (b).

Wikipedia defines icebreakers history from the 1830 century, when the development of steam engine and reinforced inclined bows enabled oar powered postal ships and sail boats to break the ice ("Jäänmurtajien historia," Wikipedia, 2009). In many cities of Europe there are old bridges over rivers that have wedged shapes and inclined leading edges to break the ice during the spring ice runoff, but maybe it had been a long process of errors and trials (Prof. M. Määttänen, personal communication, 2009).

[1] Structure - any man-made obstacle exposed to ice action (sub-sea pipeline, hull of a vessel, legs of the oil platform, etc.)

It is a fact that knowledge on ice was gained by man over many centuries, and ice-structure interaction discipline has a much longer tradition that it is usually assumed. As reported in Johannessen, et al. (2006), as early as in the late 9th century Ottar started a voyage of discovery lasting months, along the coast of Norway and Russia up to the White Sea. As reported in Suhanovsky and Slobodyanyuk (2007) the world map had not yet been drawn in parallels and meridians, but the Arctic was already known to men. At present, in connection with constantly rising human demands and climate change, investigations of ice influence on structures become widely practiced. Recently books (Vershinin, et al., 2005; Løset, et al., 2006; Gudmestad, et al., 2007; Vershinin, et al., 2008) are published, where authors generalized stored knowledge and experience on ice and its influence on structures. "Arctic sea routes opening up with climate change" says the People & the Planet website. "Water ice was found to be one of the most abundant minerals in the outer Solar System by Voyager spaceprobes. The disruptive properties of the ice must be studied in order to make clear the formation process of outer planets and satellites" says Kato, et al. (1995).

Nowadays ice science is mainly technology driven. Besides open to general use literature on ice, some experimental data and technical reports are inaccessible due to their privacy. Often it happens, that confidential investigations repeat a work done by a PhD student and the other way around. To date, the problem of ice-ridge[2] influence on structures is one of importance. From an engineering perspective large ice-ridges control the design load levels for sea ice interactions with offshore structures. Also they can be a significant navigation problem in ice covered waters. In addition they can scour the seafloor in relatively shallow waters. Ice scouring has an influence on the design of pipelines and other sub-sea facilities. For big lakes such as Minnesota's lakes the result of ice ridging may include significant damage to retaining walls, docks and boat lifts and even cabins. Ice information is required by a wide spectrum of users operating at high latitudes. These include fishing activities in areas such as the Barents Sea and the region around Svalbard, and merchant vessels on-route through ice-infested regions in the Baltic or the Canadian, Alaskan and European Arctic. Greater exploitation of the Arctic for its offshore oil and gas reserves has lead to a requirement not only for accurate and timely monitoring but also reliable design statistics for offshore construction.

In spite of the importance of ice-structure interaction and the availability of a large amount of literature on ice, the process of ice failure is not yet completely understood; data of ice force from full-scale measurements available for research are lacking (Gürtner, 2009b). Many doubts still remain regarding the action of ice-ridges on structures (Løset, et al., 2006). "It is believed, that in order to understand the failure of ice and ice loads on structures, the ice-structure interaction should be studied as a process and simulated" says Paavilainen, et al. (2009).

[2] Ice-ridge - line or wall of broken ice forced up by pressure (World Meteorological Organization (WMO) sea ice nomenclature WMO/OMM/BMO - No.259 Suppl.No.5)

Objective and organization of the thesis

The main intent of this work has been to contribute to the knowledge on ice-ridges interaction with structures by (i) gathering information via face-to-face discussions, email communication and survey of literature including project reports, news articles, Web pages, and other resources, (ii) study the behavior of adfrozen ice via detailed analysis of the freeze-bond (FB) shear strength experiments (Repetto-Llamazares, et al., 2009b). Another aim of this work was to build a finite element model to simulate direct shear test on adfrozen ice samples in order to extract material parameters of the model ice. These parameters are needed to simulate the processes of ice fracture. One part of the present work is a follow-up of previous research on ice-structure interaction by Gürtner (2009b) and Konuk, et al. (2009a,b). These authors introduced a methodology for simulating different ice-structure interactions scenarios that was investigated within the present study. Another part of this work is a follow-up of the preliminary study of the FB shear strength (Repetto-Llamazares, et al., 2009b). The objective of this part of the work was to analyze earlier obtained trends for FB shear strength, and, despite the fact that the conducted experiments were intended to study freeze-bond shear strength, to try and extract any additional information which could be used for better understanding of FB failure processes and for numerical modeling of the ice-ridges.

The thesis is divided into four chapters. Chapter 1 comprises a state-of-the-art knowledge on ice-ridges structures interactions; a theory, explaining the importance of the FB in ice-ridges; a basic theory behind the algorithm proposed in Gürtner (2009b) and Konuk et al. (2009a,b) for the modeling of ice-ridges structure interactions. Chapter 1 also gives a summary of the experimental setup used to study the FB shear strength and describes the finite element model, which was built to study material properties of ice, and the algorithm proposed for modeling ice-ridges structure interactions. Chapter 2 presents the results from interpretation of model tests presented in Repetto-Llamazares, et al. (2009b), and the results of simulations of the FB shear tests. Chapter 3 concerns the discussion of the results in Chapter 2 and summarizes work which has been done. In Chapter 4 conclusions and recommendations for future work are given.

Limitations of the thesis

The data presented in this study should be regarded as illustrative rather than exhaustive. The main focus of the work has been the investigation of freeze-bond behavior under shear conditions and incorporation of knowledge, gained during the experiment, into the finite element (FE) model with additional investigation of FE software capabilities in modeling ice fracture. Many important aspects of ice-ridge structure interaction have not been addressed in this thesis. Knowledge on ice-structure interaction discipline is at a particularly dynamic stage in the world, which means that there are new developments and announcements happening on a monthly basis. Therefore, this work need to be seen as "snapshot" that was current at the time it was taken; it is expected that specific facts and figures presented in this work may become dated very quickly.

THEORY AND METHODS 1

1.1 Overview of Ice - Ridges Structure Interaction

1.1.1 General

First year ridges are formed due to relative motion of level ice sheets. Under pressure an entire ice sheet may buckle and break in bending, creating two interacting ice sheets. The edges of the floes break into smaller pieces, called ice rubble. While the ice fields continue to collide against each other the thickness of the rubble pile at the interaction zone increases and gradually forms a ridge type formation. The resulting floating ridge consists of two parts: the sail and the keel (Figure 1.1). The ridge keel can be divided into two parts: the consolidated layer and the rubble (unconsolidated or partly consolidated part). The ridge sail is located above the waterline and it is composed of floes that are only partly frozen together. Often the ridge sail is covered by the snow. The consolidated layer is just below the waterline. In this layer water between the ice blocks is completely frozen resulting in a conglomerate ice plate. The thickness of the consolidated layer develops with time depending on temperature history. The rubble consists of broken ice blocks with irregular shapes. Blocks are found to be in contact with each other, and can freeze together, creating freeze-bonds, thus changing the contact conditions with time.

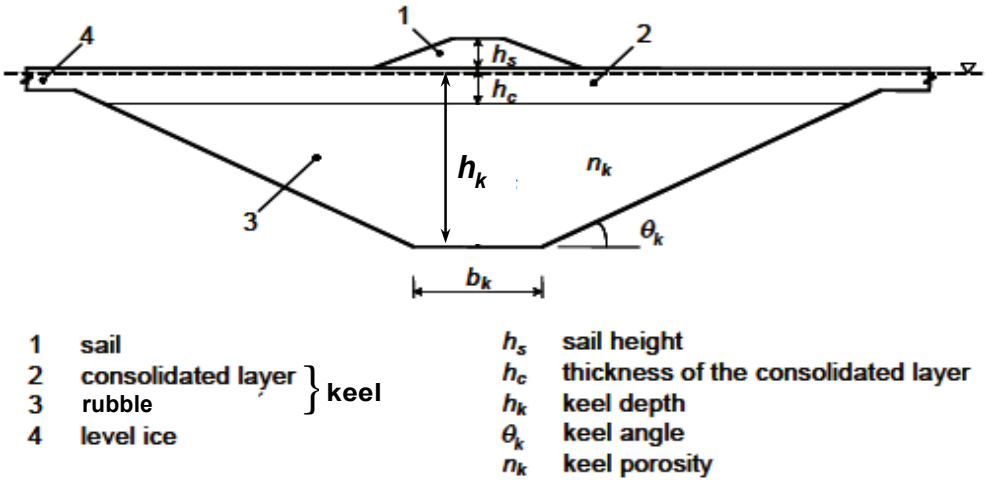

Figure 1.1 - Geometry of a first year ridge (Määttänen and Lija, 2005).

Multi-year ridges develop in high Arctic from the first year ridges. During summer season the shape of the first year ridge is smoothed, salinity of ice decreases and fresh water pools form at upper parts. If during summer the temperatures variations of the environment surrounding the ridge are not enough to completely melt the ridge, then

during next winter this mixture of low salinity ice and fresh water freezes together forming a stronger ice conglomerate, called multi-year ridge.

Many analytical models of a ridge keel exist. One of them is given by Vershinin, et al. (2005) and described below.

Immediately after ridge formation, unconsolidated keel is characterized by initial cohesion (C_i), called interlocking and a friction between the ice blocks. As soon as the rubble comes to rest after its formation, adjacent ice blocks start to freeze together at their points of contacts and freeze-bonds are formed. The keel parameters are changed and the internal friction as well as cohesion of such medium have a more complex meaning. Formation of freeze-bonds results in a partial or complete loss of interlocking forces. Anisotropy rises during process of ridge formation and during creep (vertical ridge recomposing). Stronger freeze-bonds (bigger contact area) appear to be horizontally oriented. Due to peculiarities in behavior of discrete medium under the load and due to failure of definitions such as "*internal friction*" and "*cohesion*" (Vershinin, et al., 2005) introduces new parameters: ϕ_r - angle, resisting to shear and C_s - structural shear resistance. Both ϕ_r and C_s exist only prior to the moment of irreversible fracture. C_s is the sum of interlocking force and freeze-bond force. Force, resisting to shear (F_T) of discrete medium is:

$$F_T = C_s + F_N \tan(\phi_r(F_N)), \tag{1.1}$$

where F_N is the confining load.

Internal resistance appears due to frictional forces acting between the ice blocks. It exists only at the limited zones of contact. Structural resistance appears due to interlocking of the blocks and their further rotation and due to presence of freeze-bonds forces. Quantitative values of these parameters depend on many factors such as ridge porosity, ice block thickness, level of consolidation, etc. Ice-ridges, built artificially, might not correspond to the natural ice-ridges even if similitude has been fulfilled.

The spatial orientation of the blocks (Figure 1.2) can be divided into two main classes: the orientation type "*end-side*", (*E-S*), and the orientation type "*side-side*", (*S-S*). The type of orientation is defined by the angle between the axes of the two blocks. The *E-S* type is for angles more than 45°, and *S-S* is for angles less then 45°. The *E-S* orientation is unstable and changes to *S-S* with a shear displacement of the ice-ridge. Field measurements in the Sakhalin area show that the *S-S* orientation dominates in ridges. This might allow one to consider that the internal structure of the ice-ridge is stable. The ice-ridges found in nature can be described with a discrete cohesive model. In this model the ice properties, the porosity of the medium, quantity and quality of contacts are the same as for the 'real' ridge. If a continuum model is used to describe the ice-ridge, then it is necessary to control the criteria governing equivalence between the discrete and the continuum model.

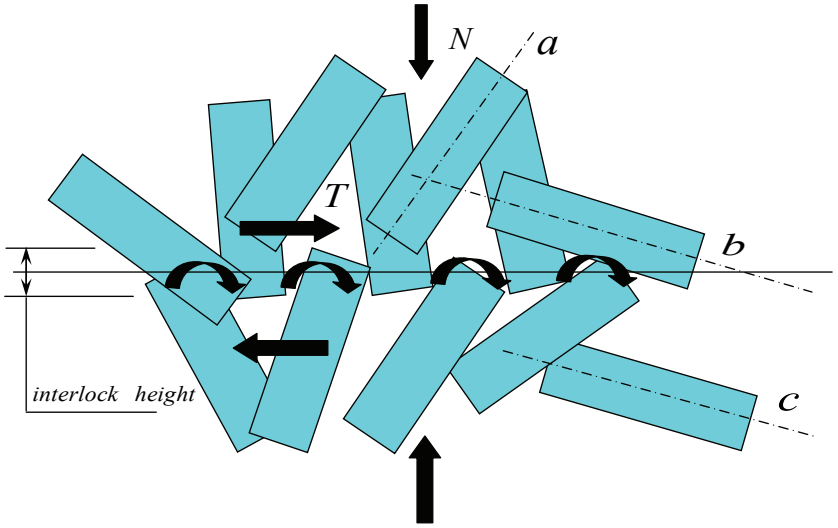

Figure 1.2 - Interlocking effect and spatial orientation of ice blocks (the *E-S* orientation is between the blocks with axes *a* and *b*; the *S-S* orientation is between the blocks with axes *b* and *c*) (Vershinin, et al., 2005).

Thus, ridge formation and its aging process play an important role. They result in variation in ridge porosity, keel strength, pressure, and cohesion between ice blocks. Mechanical and physical properties of ice-ridges are one of the main parameters defining the design level of ice load. These properties are relatively well understood for the level ice but less for the ice-ridge (Timko, et al., 2000; Heinonen and Määttänen, 2001). At the same time measuring strength parameters is an almost insuperable problem under field conditions. In order to define ice-ridge mechanical and physical properties in-situ full-scale, in-situ small scale, laboratory tests or numerical simulations can be used.

1.1.2 Ice-ridge structure interaction

Unfortunately, designing a structure against ice loads is not yet a mature engineering discipline. Currently in the world there is no common technique for ice-ridge load estimation. A study has been performed by Timco and Croasdale (2006) to investigate the general level of agreement when predicting ice loads from various international experts. They reported a large range of predicted loads from first-year ridges (factor of five) and multi-year floes (factor of seven) interacting with a vertical-sided structure. Four different approaches can be used to define an ice-ridge load on a structure: (1) use of Codes, (2) full-scale data, (3) analytical models, or (4) numerical models. Timco and Croasdale (2006) show that using full-scale data or analytical models as the basis for determining ice-ridge load on vertical structure is the dominating approach used by international experts (Figure 1.3). Each from the four aforementioned approaches is discussed below.

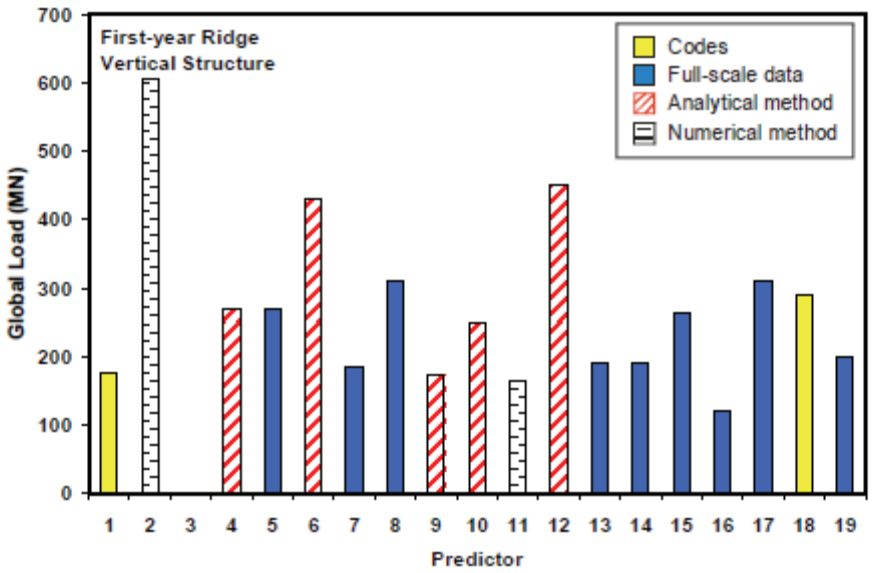

Figure 1.3 - Predictions for scenario of a first-year ridge interacting with a vertical-sided structure. "*An analytical model based on full-scale data*" is categorized as full-scale data (Timco and Croasdale, 2006).

1.1.2.1 Codes

The ridge load estimations techniques used vary from country to country. Estimation techniques are influenced by different local knowledge about local ice conditions. Northern European countries, Russia and China have their own national design practices and recommendations for ice-ridge loads calculations. Timco, et al. (1999a), Määttänen and Lija (2005), Bruun and Gudmestad (2006), Masterson and Frederking (2006) compared different calculation algorithms realized in national design practises, recommendations and standards for calculating ice-ridge loads. Among them are API, CSA, DNV, DS, GLO, IALA, IEC, ISO, NORSOK, NPD, Q/HSn 3000-2002, RIL, SNiP, and VSN.

Coverage of ice-ridge forces in different codes differs considerably. According to Määttänen and Lija (2005) some codes give detailed guidelines how to calculate the forces from the ice-ridges while others may just warn of the significant ice forces exerted on a structure. They reported that the multi-year ridge scenario is missing in IEC, RIL, SNiP and VSN. For the first-year ridge scenario GL does not give design guidelines. CSA does not suggest any method for first-year ridge keel loads. SNiP, VSN, IEC suggest a ridge load to be calculated similar to a crushing load. Many codes do not have clear guidelines for ice-ridge load calculations for different structure geometries (vertical/conical structure, wide/narrow structure). The solutions in the codes are given by formulas, while graphs represent the coefficients. All these solutions include a number of parameters, which are hard to define in a real situation. As a matter of fact, calculation principles in national design practises, recommendations and standards mainly come from the experience of the authors. Basically, such experience is gained from full-scale observations. Let us consider the Baltic Sea. Only first-year

sea ice exists there (Toikka and Hallikainen, 1992), and an ice-ridge building process is mainly dominated by rafting, therefore, it is reasonable that RIL does not have any guidelines for the multi-year ridge scenario. In the Barents Sea ice-ridge building processes mainly dominated by ridging and, therefore, differences between calculation algorithms and recommendations in NORSOK and RIL are to be expected.

1.1.2.2 Full-scale measurements

Full-scale investigations of actions from first-year ridges in the Beaufort Sea were done by Wright and Timco (1994) and Timco, et al. (1999b). According to Gürtner (2009b), only limited full-scale data of ice forces are available for research. For more than ten years leading oil companies around the world have been using advanced technology, like underwater sonars, for the automated and continuous monitoring of the ridges geometry. Data obtained from such monitoring are confidential and are published only after several years.

Full-scale observations on ridge interactions with offshore structures show that the details of the ridge failure mechanism are variable. Therefore, an accurate theoretical estimation of the forces caused by ice-ridges is not feasible (Määttänen and Lija, 2005). "First-year ice actions in sub-arctic (or temperate) Bothnian Bay of the Baltic Sea are often different from what is commonly assumed in literature" writes Dr. T. Kärnä (personal communication, 2009). And he continues: "Some of the observations of mine include:

- → The sail-area of an ice-ridge was the weak link in all ridges that I observed. So, what is the consolidated layer here?
- → All ridges that I observed had an area of rafted ice adjacent to the ridge sail. This rafted ice provided the highest load - not the area of the ridge sail where the strong part is usually assumed to exist. Ice-induced vibrations were also caused by the rafted and refrozen part of an ice-ridge.
- → Ice-ridges never failed in the manner that we are postulating in simple formulas, such as Dolgopolov's formula. Instead, several kind of load-releasing mechanism restricted the ice load.
- → The relatively thin ice (< 0.5 m) did not keep its integrity at a low ice speed - so bending failure or a mixed-modal failure was common. Ice crushing all over the ice-structure interface was common at higher ice speeds (> 0.1 m/s)."

Full-scale measurements are expensive, not always possible and time consuming, but can we rely on the measurements? Reported full-scale data might not reflect reality due to an inaccuracy in measuring devices (Jefferies, et al., 2008).

1.1.2.3 Analytical models

Several approaches and theories have been proposed to calculate the forces that a first-year ridge of sea ice would exert on an offshore structure. The theoretical approaches vary widely and depend upon the shape of the structure (vertical or sloped) and the

(assumed) failure mode of the ice. Vershinin, et al. (2005) comment that methods for estimating ice-ridge loads on vertical-sided structures are most developed. Analytical models referred to vertical-sided structures are discussed in Timco, et al. (1999a). Loads predicted by analytical models of Korzhavin (for a consolidated layer), Dolgopolov, Prodanovic, Mellor, Hoikkanen, and Weaver (for the local failure), and models of Croasdale, Prodanovic (for the global failure) were compared with the full-scale measured load. Authors conclude that although there appeared to be a reasonable agreement between the predicted and measured loads, a large number of assumptions had to be made to predict the load. Although there are a number of calculation models available for determining ridge keel forces, they all have the following inadequacies (Timco, et al., 1999a):

- → Results depend very much on the shape and position of the failure plane assumed.
- → They are over-simplified in their treatment of a ridge and structure geometry.
- → They depend very much on ridge properties that are difficult to determine.
- → There are significant disagreements between the models.

Use of analytical models, reviewed in Timco, et al. (1999a), for predicting the loads due to ridge keels and sails should also be viewed with caution.

It is conveniently to treat ice-ridge loads as the sum of loads from a consolidated layer and ice rubble (Vershinin, et al., 2005). This approach allows applying separately methods for calculating loads from level ice and methods for calculating pressure of Coulomb medium. When ridges interact with conical structures (as in the level ice case scenario) the mechanism of ice failure is changed. The method to treat ice load as the sum of loads from a consolidated layer and rubble is no more feasible. Ice-ridge actions on conical structure in field conditions have been poorly investigated. In case of an ice-ridge interaction with conical structures model tests are usually used in order to estimate the loads. Such tests with conservation of the Froude number leads to technical difficulties. Therefore if the ice-ridge interacts with a conical structure, then the computational methods based on mechanics and involvement of experimental data plays a special role. Vershinin, et al. (2005) gives different methods for calculating both loads form ice-ridge on vertical structures and loads form ice-ridges on conical structures. Wang (2000) gives an analytical method for ice-ridge crack loads on a multifaceted conical structure. Nevel (2001) presents analytical methods for calculating ice-ridge forces on a downward breaking cone.

Still many questions remain unresolved regarding properties of ridge keels and their interaction with structures. The process of an ice-ridge interaction with a structure is not well understood yet.

1.1.2.4 Numerical models

The main elements of a numerical simulation are illustrated in Figure 1.4.

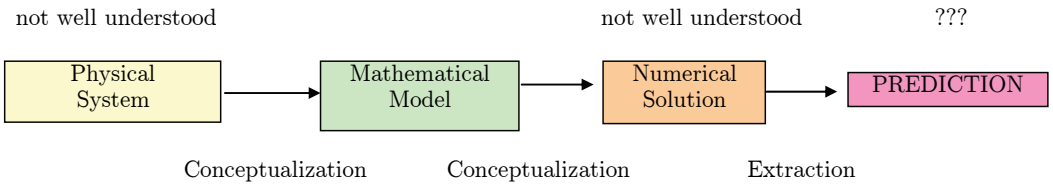

Figure 1.4 - Main elements of a numerical simulation (Szabó 2007).

The first and the most important step in a numerical simulation is the description of the physical system. After the first step is accomplished a mathematical model has to be defined. This second step is very important in the numerical simulation. The choice of the mathematical model depends on the level of accuracy required and the targets of computation. The process between the first and the second step is called conceptualization. Here, decisions have to be made about the level of topological details to be included, material properties, boundary conditions, solution algorithms, etc. In the third step it is important to ensure that a numerical solution is an adequate representation of the 'exact' solution, associated with the mathematical model.

Solving the problem of an ice-ridge structure interaction is a difficult task, which requires high computational power. These days a processor's clock speed reaches its peak because more clock speed will generate more heat and require more power. Therefore, researchers built processors with more than one processing unit in it e.g. dual core to get more processing power. Also to do complex computational tasks, supercomputers are usually used as they provide a processing power equal to the sum of their clients. For example, to do the computational work needed for the Large Hadron Collider, CERN developed a system in which any user on internet could provide the idle cycle of their processor, which could then be used for processing information. Currently researchers are trying to build a quantum computer to make computations even faster. But it is in research phase at the moment (G. Singh, personal communication, 2009). With development of technology new possibilities are opening for modeling of ice-structure interactions.

Nowadays, it is common for relatively new ice science to borrow some modeling techniques from state-of-the-art mechanics in soil and rock, metal science, concrete science, etc. For example, a relatively new technique to simulate crack initiation and crack growth was used by Gürtner (2009b) to simulate the ice fracture process. In his simulations a cohesive zone approach was implemented into a multi-material model of ice, structure and water. The applicability of such approach for ice related problems was shown in examples. Konuk, et al. (2009a) suggests that frozen ice rubble in the ridge sail/keel can be modeled with the help of cohesive element technique. The discretization algorithm proposed by Konuk, et al. (2009a) will be discussed later.

Not so many attempts at simulating ice-ridge structure interaction have been made. On the other hand more work has been done to simulate ice failure against offshore structures and ice-ridge gouging. Sand and Horrigmoe (2001) built a finite element (FE) model to simulate multi-year ridge interaction with a conical structure. The FE Method (FEM) was used to simulate ice-ridge failure against offshore structure by

Martonen (2003). Numerical simulations of ice-structure interactions with FEM were done by Chehayeb, et al. (1986). Sand and Horrigmoe (1998) simulated level ice interactions with a sloping structure. In Gürtner (2009b) an overview of numerical methods used for simulating of ice accumulations in offshore structures is given. Among them are the Discrete Element Method (DEM) and the Particle in Cell (PIC) method. An attempt to simulate ridge keel failure by the FEM was made by Heinonen (1999) and Heinonen (2004). FEM was used to simulate punch tests on ice rubble by Liferov, et al. (2003). A 2D computer Finite Difference program "Inhomogeneity", which gives possibility to determine the load dependence on the ice strength heterogeneity, has been developed by Shkhinek, et al. (2007). FEM was used to model the ice-rubble behavior by Shafrova, et al. (2004) and Liferov (2005). Numerical simulations of dynamic ice forces on offshore structures were done by Blackerby (2006). FEM was used for modeling of ice-rubble accumulations and ice-structure interactions by Gürtner (2009b). McKenna, et al. (1997) used the discrete element code to model a force from pack ice, Løset (1994a, b) used DEM to simulate the ice forces on a boom. A combination of FEM and DEM is being used for modeling of ice interactions with sloping structures (a two-dimensional model) and the full-scale punch tests in ridges (a three-dimensional model) by J. Paavilainen (personal communication, 2009) and A. Polojärvi (personal communication, 2009) respectively. Numerical models of seabed scour by an ice-ridge are being developed by many researchers.

As numerical models are easy to change and control, there is a tendency to use verified numerical models to investigate some important effects which can not be found directly from experiments (Prof. J. Tuhkuri, personal communication, 2009). Commercial software such as ADINA, PAFEC (Varstad, 1983), ABAQUS, (Heinonen, 1999), ANSYS, (Horrigmoe, et al., 1994; Sand and Horrigmoe 1998; Sand and Horrigmoe, 2001; Martonen, 2003; Derraji-Aouat and Lau, 2005; Blackerby, 2006; Sand and Fransson, 2006), PLAXIS, (Liferov, et al., 2003; Shafrova, et al., 2004 and Liferov, 2005) and LS-DYNA (Derraji-Aouat and Lau, 2005; Yu, et al., 2007; Gürtner, 2009b) are often used for simulations of ice failure processes. The software package DECICE ("Making Waves", Oceanic Consulting Corporation, 2009), finite difference program "Inhomogeneity" (Shkhinek, et al. 2007), purpose-built finite difference code (Moslet, 2008) and probably many other programs were developed to model ice and solve ice impact problems.

Even though there is a large amount of literature on the subject of numerical modeling of ice-structure interactions there is no clear agreement among the authors regarding modeling of the ice-ridges. The numerical techniques used for predictions of design loads are unexplored. The most common approach is to divide the ice-ridge in three parts: a consolidated layer sail and rubble. The consolidated layer is usually modeled in the same way as the level ice. There are three different approaches to treat the sail and the rubble: (i) continuum, (ii) discrete, (iii) pseudo-discrete. It is not clear which approach is the best. No guidelines exist on which approach should be used. Many questions remain unsolved regarding modeling of crack growth in ice. In order to more accurately reflect real world conditions in the simulations a good constitutive model for sea ice is needed.

Besides the uncertainty in the "reality of ice-ridge structure interactions", there are three different types of errors in validated numerical models. They are: (i) errors in the mathematical model or hypothesis being tested, (ii) errors in the numerical approximation, (iii) errors in the experiment and statistical variations. Unless the errors in the numerical approximation and the experiment are controlled, it will not be possible to judge whether the problem, if any, is in the hypothesis being tested or in the model (Szabó, 2007).

From Figure 1.4 a simple question arises: if the process of an ice-ridge interaction with a structure is not well understood yet and if there are doubts regarding modeling of the ice fracture, then how accurate can simulated predictions be? Can we rely on them? The fundamental question of computational engineers regarding whether or not it is possible to predict the response of the structure to an ice-ridge excitation via numerical simulations with a high degree of reliability remains unanswered.

1.1.3 Uncertainty summary

Even if a large body of literature exists on the subject of the ice-ridge structure interaction, the physical process of the ice-ridge structure interaction is not well understood. No common techniques exist for estimation of loads exerted by an ice-ridge on a structure. Proposed calculation algorithms require initial data which is difficult to define in practice. Coverage of ice-ridge forces in different codes differs considerably. There is a lack of full-scale data available for research. Almost no numerical tools are available to model ice-ridges. Laboratory or full-scale tests are needed to validate the numerical models.

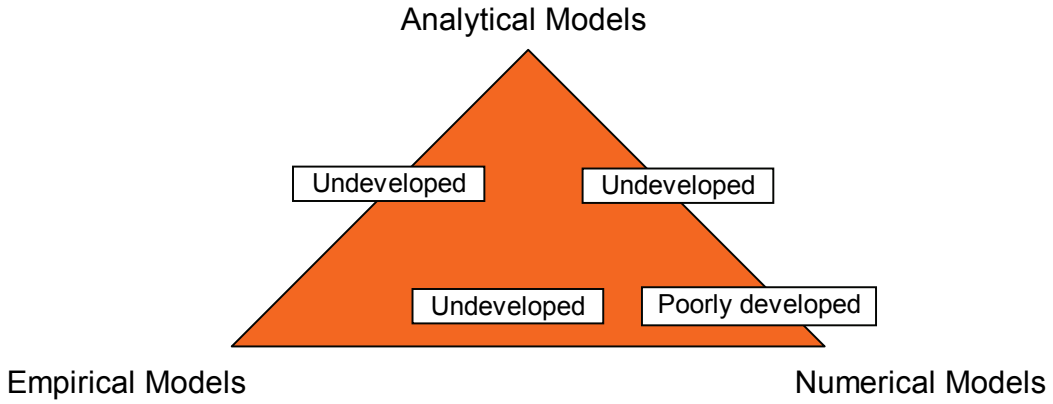

Figure 1.5 - Development state.

The state of the art in the knowledge of ice-ridge structure interaction is schematically shown in Figure 1.5. At present, much work has already been done in building analytical models, and many full-scale and laboratory tests have been carried out. But there is still a need for improvements. In comparison with analytical models numerical models are poorly developed. There is a need in both methodologies to solve ice-ridge interaction problem and experimental (full-scale) data for the validation of numerical models. As it can be seen from Figure 1.5 all three model families are interconnected. Unfortunately the knowledge field, directed towards connecting those modes, is almost

undeveloped. The reason for such uncertainties might be that historically in the general engineering discipline, designing for collision (impact) is done on the basis that an impact is an extremely unlikely event.

1.2 Importance of Freeze-bonds (Theory)

In Section 1.1 it was shown that the physical behavior of ice rubble and its thermo-mechanical properties are not well understood. There is no consensus among the experts regarding what load is exerted on a structure by an ice-ridge. The deformation process of ice-ridges remains unclear. Experiments show that the failure of the non-consolidated part of the ridge keel happens due to displacements at the contacts between the ice blocks (Vershinin, et al., 2005). Besides, the process of producing 'correct' model ridges seems undeveloped. The relation between model experiments and full-scale measurements is not straightforward (Repetto-Llamazares, et al., 2009b).

The importance of the freeze-bonds (FBs) during the ice-rubble failure is discussed by many authors (Ettema and Urroz, 1989; Surkov and Truskov, 1993; Surkov, et al., 2001; Shafrova, et al., 2004; Vershinin, et al., 2005; Liferov, 2005; Liferov and Bonnemaire, 2005; Repetto-Llamazares, et al., 2009b) as well as the FBs contribution to the peak-load value at failure of ice rubble. So, FBs seem to play an important role in the ice-ridge failure process but not many attempts have been made to study the appearance of FBs and their characteristics. Besides, the lack of data on the FBs and the different techniques used for the investigation of FB properties make the comparison of results complicated. Different FB test setups are given in the Appendix A.

1.2.1 General

Many analytical and numerical models attempt to describe a medium consisting of broken ice pieces by elastic-plastic behavior with a Mohr-Coulomb yield surface. Ettema and Urroz (1989) write: "Shear behavior of ice rubble cannot be adequately characterized in terms of linear Mohr-Coulomb criterion $\tau = \sigma tan\phi + C$ (τ - shear strength, σ - confining pressure, ϕ angle of internal friction, and C - cohesive intercept), as shear is subjected to the influence of freeze bonding, which causes individual pieces to fuse together, and ice piece deformation and disintegration". Vershinin, et al. (2005) suggest a Mohr-Coulomb diagram for the ice rubble as shown in Figure 1.6. The given diagram is based on the analytical solutions suggested by the authors, and postulates of the plasticity theory.

The Mohr-Coulomb diagram for the partly consolidated medium should be an envelope (the consolidation process doesn't decrease the strength of the medium) and a part, which is tangential to the Mohr-Coulomb diagram (for high values of σ - compression) for the unconsolidated medium. A decreasing degree of consolidation results in an increasing frictional angle, i.e. increase of slope of Mohr-Coulomb diagram. It can be presumed, that nonlinearity of Mohr-Coulomb diagram is a violation of Amonton's laws regarding the independence of friction coefficient on vertical confining load, due

to small contact areas and, thus, the medium has a nonlinear dependence on the hydrostatic confinement.

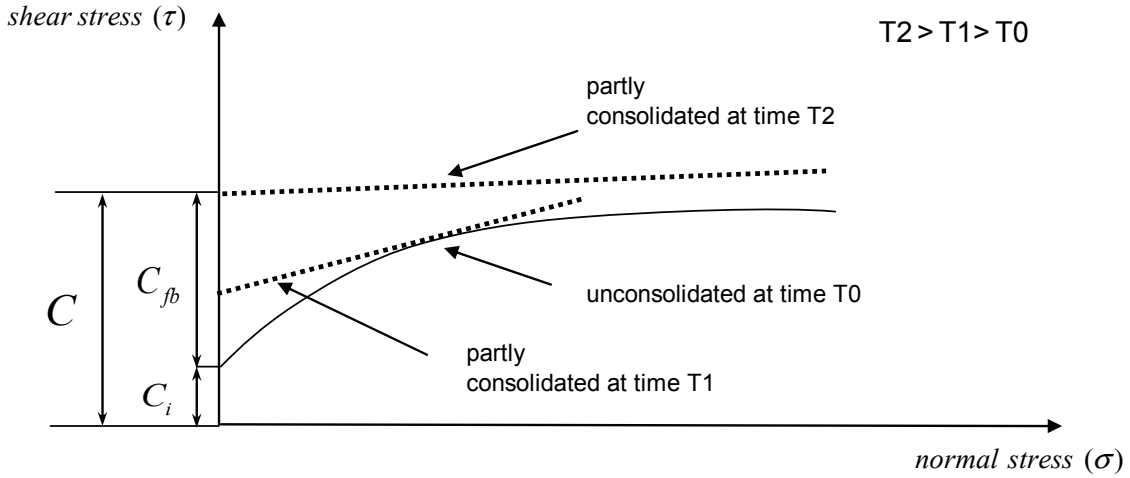

Figure 1.6 - Qualitative forms of the Mohr-Coulomb diagram for a partly consolidated and unconsolidated media (Vershinin, et al., 2005)

According to Vershinin, et al. (2005), the cohesion of a partly consolidated ridge (C) can be calculated as the sum of the cohesion due to interlocking forces (C_i), which is considered as the cohesion of the unconsolidated ridge, and the cohesion due to freeze-bond forces (C_{fb}). Ridge interlocking forces are dependent on the ice-rubble thickness and could be defined almost precisely by direct measurements (Punch-test on unconsolidated ridges and Shear-box test in the laboratory). The value of interlocking is a few times lower than the value of cohesion during consolidation process and, as it can be presumed, it doesn't rise above 3-5kPa (experiments in the Baltic Sea with poorly consolidated ridges).

1.2.2 FB creation, FB importance

Information in this section is based on Chapter 3 in Vershinin, et al. (2005). Unfortunately, from the source it was not always clear whether the presented data are based on theory or on the experiments.

When an ice-ridge is formed, especially at low air temperature, ice freezes over the surface of the broken ice pieces due to *internal cold energy*. So, ice blocks freeze together at their contacts, creating FBs. Figure 1.7 shows schematically of the freezing process over the an ice block of radius *(R)*. For simplicity, it is supposed that the ice block has a spherical shape.

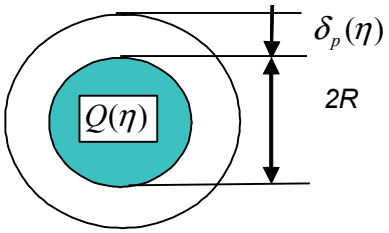

Figure 1.7 - Scheme of freezing over an ice block (Vershinin, et al., 2005)

The amount of *cold energy* in the ice block ($Q(\eta)$) at the moment of the ice-ridge creation can be written as:

$$Q(\eta) = \int_0^{T_{av}} (\theta - \tau_i) \cdot c_p(\upsilon, \tau_i) \frac{4}{3} \rho_i \cdot \pi R^3 \cdot d\tau_i \tag{1.2}$$

where $\eta = T_{av} - \theta$; c_p is heat capacity of ice as a function of salinity (υ) and temperature (τ_i); θ is the melting temperature of ice; T_{av} is the average ice temperature; ρ_i is the sea ice density. The thickness of the additional ice layer ($\delta_p = \delta_p(\eta)$) can be found from:

$$Q(\eta) = L\rho_i \frac{4\pi(R + \delta_p)^3 - 4\pi R^3}{3} \approx 4\pi\rho_i \cdot LR^2\delta_p \tag{1.3}$$

where L is the specific latent heat of sea ice.

Note: Oceanic flux is assumed to be zero in this model.

An ice block submerged in water undergoes three stages of thermal changes. First the temperature changes as ice piece is colder than the surrounding water, and the initial condition at the ice boundary become important. Later the steady-state stage advances, which ends with the stage of equilibrium temperature between the ice block and surrounding water.

The heat flow through the area *(Ω)* over the time (Δt) can be calculated by Equation 1.4 if the following assumptions can be made:

(1) The temperature gradient along the ice block thickness is given in Figure 1.8

(2) The initial stage of temperature change proceeds locally and fast without significant changes of the total amount of cold in the ice block.

(3) The effect of frozen-over ice on the temperature variation is negligible.

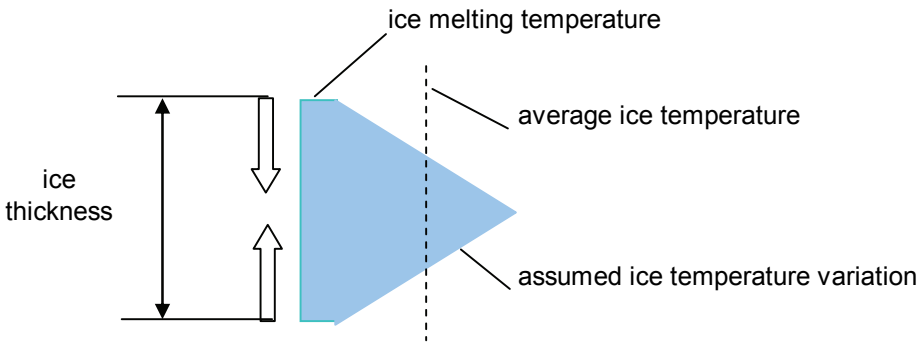

Figure 1.8 - Scheme for estimating ice block temperature variation with time (Vershinin, et al., 2005)

$$\frac{Q(t)-Q(t+\Delta t)}{\Delta t \cdot \Omega} = \lambda \frac{\eta(t)+\eta(t+\Delta t)}{h/2}$$
$$Q(t) = c_p \cdot h/2 \cdot \Omega \cdot \eta(t) \cdot \rho_i \qquad (1.4)$$

Where c_p, λ are the heat capacity and the thermal conductivity of the ice block respectively, averaged through the ice thickness (h);

Then, averaged variation of the ice temperature as a function of time is shown in Figure 1.9.

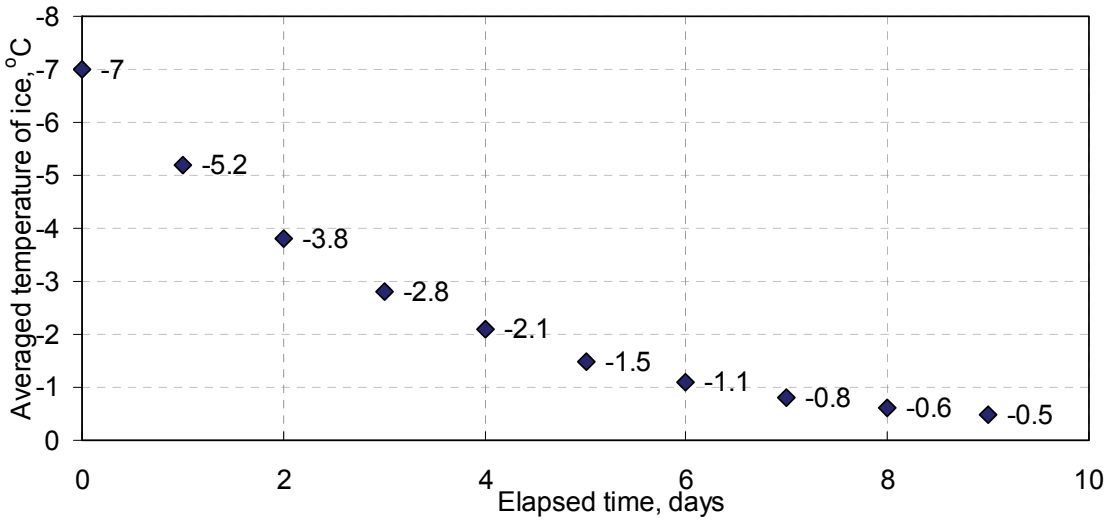

Figure 1.9 - Temperature of ice as a function of time (Vershinin, et al., 2005).

Freezing process over the ice block varies with time. From calculations it can be seen that such a process for the ice block, with thickness less then one meter, doesn't significantly progress in time if this process lasts more then ten days. Hence for ice-

ridges older then one month it can be assumed that $\delta(t) \approx \delta_p$. Volume of newly created ice by the freezing-over process is shown in Figure 1.10 as a percentage of the volume of the ice block.

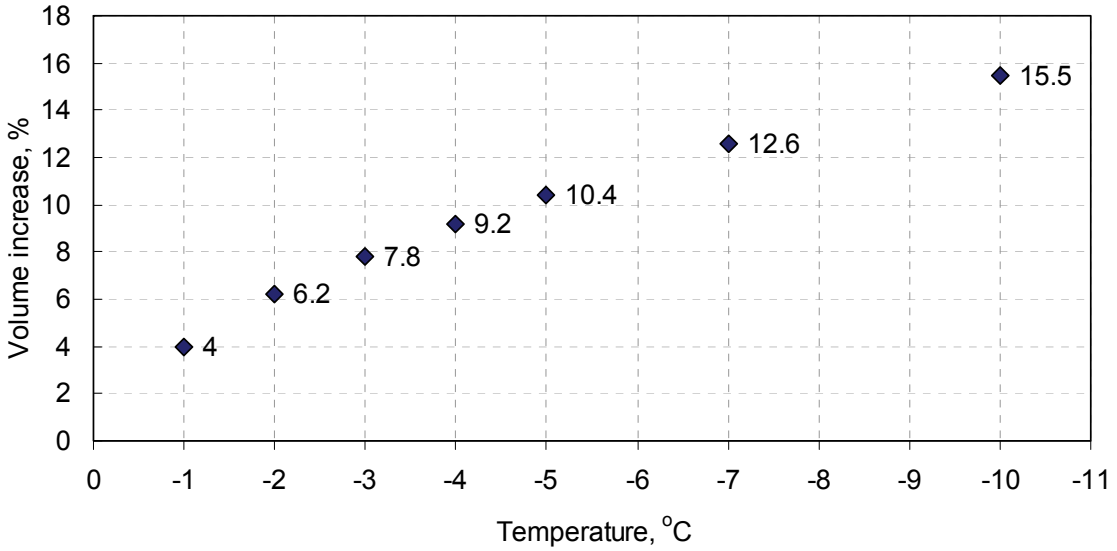

Figure 1.10 - Increase of volume as a function of temperature; (Ice salinity 3.5% and θ=-1.5°C) (Vershinin, et al., 2005).

A model of a ridge consolidation can be represented as a cell structure consisting of frozen together spheres. The physical parameters of the ice at the contacts are defined by properties of the FB as a function of salinity and temperature. The properties of horizontally oriented FBs differ from those of vertically oriented ones. The ice-ridge re-compaction process, which takes place after the ice-ridge has been created, results in an increase of horizontally oriented FBs, especially at the upper part of the ridge. Vertically oriented FBs are less affected by the re-compaction process. Horizontally and vertically oriented FBs are illustrated in Figure 1.11a and Figure 1.11b respectively.

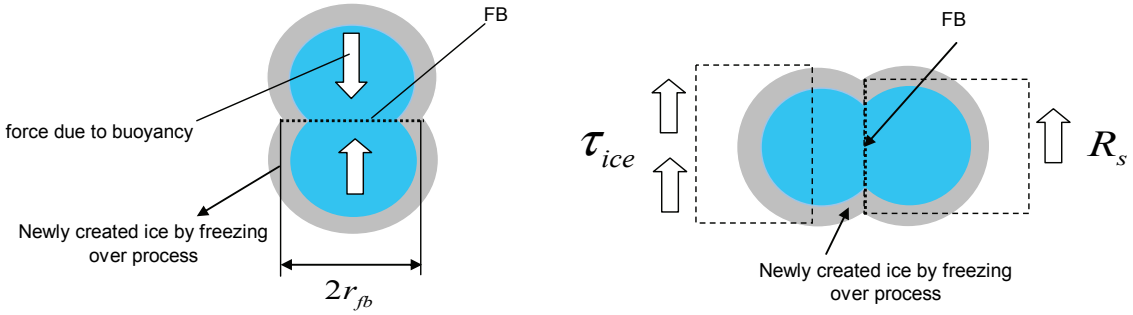

(a) FB confinement

(b) FB – ice strength relation scheme

Figure 1.11 - Scheme of the frozen together spheres, (a)-horizontally oriented, (b)-vertically oriented FB (Vershinin, et al., 2005).

FB strength corresponds to the strength of sea ice with high brine content.

For the vertically oriented FBs Vershinin, et al. (2005) give following strength parameters:

(1) Compression strength of FB is R_c=*0.4-0.6MPa;*

(2) Tension strength of FB is R_t= *0.2-0.3MPa;*

The strengths ratio is $\frac{R_c}{R_t} = \frac{tan(45 + \phi/2)}{tan(45 - \phi/2)}$, ϕ_i=20° - angle of internal friction of ice;

(3) In according with Coulomb's theory the shear strength of FB is $R_s = 1/2(R_c R_t)^{1/2}$ =*0.14-0.21MPa.*

Strength parameters for horizontally oriented FBs are higher than for vertically oriented ones due to the increase of freezing surface with re-compaction process of the ridge.

The keel of an ice-ridge can be considered as a continuum cohesive medium. Cohesion of such medium (C) can be estimated as:

$$C = F_{fb} / 4R^2 + C_i, \tag{1.5}$$

where F_{fb} is the FB force along the surface of radius (r_{fb}), see Figure 1.11a; C_i is the specific cohesion due to interlocking, defined from experiments; R is the radius of the sphere, see Figure 1.7. F_{fb} is found from the relationship: $F_{fb} = R_s \pi \cdot r_{fb}^2$.

1.2.3 Uncertainty summary

From what was presented in Sections 1.2.1 and 1.2.2, it can be seen that the existence of FBs might significantly affect the ice-ridge failure process and therefore the load exerted onto a structure by an ice-ridge. Unfortunately almost no analytical, numerical or empirical models exist which directly take into account the phenomenon of freeze-bonding. In most of the state-of-the-art models, describing ice-ridge structure interaction, influence of the FB are implicitly incorporated with other assumptions, for example, together with the assumption of failure plane. During the phase of model validation, the influence of FB on the final result is often ignored. Thus, a deeper study of the physical processes governing the behavior of both model ice-ridges and ice-ridges in nature may bring additional knowledge which will allow: (i) improvement of existed models of ice-ridges, (ii) improvement of correlation between model and full-scale experiments; (iii) improvement of numerical models.

1.3 Finite Element Method in Ice-ridges Structure Interaction (Theory)

Though several numerical models have been built to simulate loads exerted on a structure from ice-ridges, this work concentrates on the algorithm proposed by Konuk, et al. (2009a) as it looks promising for simulations of ice fracture processes. The approach is relatively new and therefore has many uncertainties, offering plenty of opportunities for investigation.

According to Konuk, et al. (2009a), for the scenario of an ice-ridge interaction with a structure the frozen rubble in the keel or sail can be modeled by utilizing the cohesive element method and the frozen consolidated layer of ice-ridges can be treated as the level ice. The authors propose the following discretization algorithm to model ice-ridges:

1. The consolidated layer is discretized by inserting cohesive elements between the internal element boundaries in horizontal and vertical planes. Properties of the cohesive elements (CEs) inserted in the horizontal planes differ from those inserted in vertical planes. The bulk ice is discretized using a structured or unstructured finite element mesh.

2. The rubble in the keel and sail are descretized using an unstructured element mesh consisting of three-dimensional continuum elements. A set $A^{(ce)}$ of CEs are introduced along some selective element boundaries. This cohesive element set is a simulation of the freeze-bonds between the ice blocks. Later some of the groups (or single) of CEs trapped between the cohesive surfaces are deleted. Created in this way voids represent porosity of the ice rubble.

3. The surface area between the keel (sail) and the consolidated layer is populated with a set $B^{(ce)}$ of CEs.

4. A set $C^{(ce)}$ of CEs is inserted in the remaining element boundaries. It represents Cohesive Zone Model[1] properties of the ice blocks.

Author of this study believes that the approach proposed by Konuk, et al. (2009a) will be used in near future for simulations of ice-ridge structure interactions. A study has been done in order to get an idea of the properties of cohesive elements from the '$A^{(ce)}$' set and therefore to contribute to the future development of the method.

[1]Cohesive Zone Model is a model developed to account for the nonlinear stress field around the crack tip and to model the softening behavior during propagation of the crack (Konuk, et al., 2009a)

1.3.1 General

The numerical model described in next subsections is based on the basic principles presented in this part of thesis. Information given in Subsections 1.3.1 and 1.3.2 is based on works by Belov (2004), Zienkiewicz, et al. (2005) and Belytschko, et al. (2006). A reader familiar with the basic principles of elasticity theory, finite element method and cohesive zone model (or cohesive crack model), may skip Subsections 1.3.1 and 1.3.2.

1.3.1.1 Foundations of the elasticity theory

Let V denote a volume occupied by a part of body, and S the surface, bounding this volume. The quasistatic problem of elasticity formulated in terms of displacements for a heterogeneous anisotropic medium includes the solution of three differential equations of equilibrium (Equation 1.6) with respect to components of the displacement vector.

$$\nabla \cdot \left({}^4\boldsymbol{C}(\boldsymbol{r}) : \nabla \boldsymbol{u} \right) + \boldsymbol{f}_V = 0 \tag{1.6}$$

In Equation 1.6 the symbol ':' denotes a contraction of a pair of repeated indices; '$\cdot$' denotes a contraction of inner indices as in Belytschko, et al. (2006);

$\boldsymbol{r} = x_k \boldsymbol{e}_k = x_1 \boldsymbol{e}_1 + x_2 \boldsymbol{e}_2 + x_3 \boldsymbol{e}_3$ is the radius-vector of considered point;

${}^4\boldsymbol{C}(\boldsymbol{r}) = C_{ijkl} \boldsymbol{e}_i \boldsymbol{e}_j \boldsymbol{e}_k \boldsymbol{e}_l$ is the fourth-rank tensor of material stiffness;

$\nabla = \boldsymbol{e}_k \dfrac{\partial}{\partial x_k}$ is Hamilton's nabla operator;

$\boldsymbol{u} = u_k \boldsymbol{e}_k$ is the displacement vector;

$\boldsymbol{f}_V = f_{Vk} \boldsymbol{e}_k$ is the vector of body forces;

Three types of boundary conditions are commonly encountered in the solution of differential equations (Equation 1.6).

1. *Kinematic boundary conditions* describe the behavior of a body at points laid within its volume (Equation 1.7).

$$\boldsymbol{u}\big|_S = \boldsymbol{u}_S(\boldsymbol{r}) \tag{1.7}$$

In Equation 1.7 S is the body surface; $\boldsymbol{u}_S = u_{Sk} \boldsymbol{e}_k$ is the displacement vector prescribed on S.

2. *Static boundary conditions* are described by Equation 1.8.

$$\boldsymbol{n}\cdot\left({}^{4}\boldsymbol{C}(\boldsymbol{r}) : \nabla\boldsymbol{u}\right)\Big|_{S} = \boldsymbol{f}_{S} \tag{1.8}$$

In Equation 1.8 $\boldsymbol{f}_S = f_{Sk}\boldsymbol{e}_k$ is the vector of surface forces (prescribed on S); $\boldsymbol{n} = n_k\boldsymbol{e}_k$ is the unit vector of outward pointing normal to the body surface.

3. *Mixed boundary conditions* are described by Equation 1.9.

$$\boldsymbol{u}\big|_{S_1} = \boldsymbol{u}_S(\boldsymbol{r})\,; \quad \boldsymbol{n}\cdot\left({}^{4}\boldsymbol{C}(\boldsymbol{r}) : \nabla\boldsymbol{u}\right)\Big|_{S_2} = \boldsymbol{f}_S\,; \quad S = S_1 \cup S_2 \tag{1.9}$$

In Equation 1.9 S_1 and S_2 are parts of the surface S. It is also possible to define combined boundary conditions, when from a total three equations one (two) equations are formulated in terms of displacements and two (one) - in terms of forces.

If the dynamic problem of elasticity is considered, then a contribution of inertia forces is considered separately (Equation 1.10).

$$\nabla\cdot\left({}^{4}\boldsymbol{C}(\boldsymbol{r}) : \nabla\boldsymbol{u}\right) + \boldsymbol{f}_V = \rho\ddot{\boldsymbol{u}} \tag{1.10}$$

In Equation 1.10 ρ is the body density and the superposed dots denote the time derivative $\partial^2 / \partial t^2$. In Equation 1.10 the term with $\ddot{\boldsymbol{u}}$ can be considered as a body force which acts in the direction opposite to the acceleration (d'Alembert force). Since the governing differential equation for the dynamic problem is second order in time, two sets of initial conditions are needed. These conditions are specified at the initial time $t = t_0$ from which the given set of equations evolves.

1.3.1.2 Basis equations

For small strains $\left(|\nabla\boldsymbol{u}|\right) << 1$ the strain tensor ($\boldsymbol{\varepsilon}$) can be approximated by Cauchy's relationships:

$$\boldsymbol{\varepsilon} = \varepsilon_{ij}\boldsymbol{e}_i\boldsymbol{e}_j \approx \frac{1}{2}\left(\frac{\partial u_i}{\partial x_j} + \frac{\partial u_j}{\partial x_i}\right)\boldsymbol{e}_i\boldsymbol{e}_j\,, \tag{1.11}$$

$\varepsilon_{11} = \dfrac{\partial u_1}{\partial x_1}, \quad \varepsilon_{22} = \dfrac{\partial u_2}{\partial x_2}, \quad \varepsilon_{33} = \dfrac{\partial u_3}{\partial x_3}$ are the normal strains;

$\varepsilon_{ij} = \dfrac{1}{2}\gamma_{ij}, \quad \gamma_{ij} = \dfrac{\partial u_i}{\partial x_j} + \dfrac{\partial u_j}{\partial x_i}$ are shear strains.

The first invariant of the strain tensor is a volumetric strain written as:

$$I_1(\boldsymbol{\varepsilon}) = trace(\boldsymbol{\varepsilon}) = \varepsilon_{11} + \varepsilon_{22} + \varepsilon_{33}, \tag{1.12}$$

Constitutive equations for a linear-elastic heterogeneous anisotropic medium can be written as following:

$$\boldsymbol{\sigma} = \sigma_{ij}\boldsymbol{e}_i\boldsymbol{e}_j = {}^4\boldsymbol{C}(\boldsymbol{r}) : \boldsymbol{\varepsilon} = C_{ijkl}\varepsilon_{kl}\boldsymbol{e}_i\boldsymbol{e}_j \tag{1.13}$$

$$\boldsymbol{\varepsilon} = \varepsilon_{ij}\boldsymbol{e}_i\boldsymbol{e}_j = {}^4\boldsymbol{S}(\boldsymbol{r}) : \boldsymbol{\sigma} = S_{ijkl}\sigma_{kl}\boldsymbol{e}_i\boldsymbol{e}_j \tag{1.14}$$

where $\boldsymbol{\sigma}$ is the stress tensor; $\sigma_{11},\sigma_{22},\sigma_{33}$ are the normal stresses, $\sigma_{12},\sigma_{23},\sigma_{31}$ are the shear stresses ${}^4\boldsymbol{S}(\boldsymbol{r})$ is the fourth-rank tensor of elastic complaisance. In Equations 1.13 and 1.14 ${}^4\boldsymbol{C}(\boldsymbol{r}) : {}^4\boldsymbol{S}(\boldsymbol{r}) = {}^4\boldsymbol{I}$ ($\boldsymbol{I}$ is the unit tensor). Equations 1.13 and 1.14 are reciprocal formulations of Hooke's law.

If displacements are large (e.g. undeformed and deformed configurations of the body the nonlinear or second-order terms of the finite strain tensor have to be considered. The strain tensor can be written as:

$$\boldsymbol{\varepsilon} = \varepsilon_{ij}\boldsymbol{e}_i\boldsymbol{e}_j + \eta_{ij}\boldsymbol{e}_i\boldsymbol{e}_j, \tag{1.15}$$

Second term in Equation 1.15 represents nonlinear part of the tensor.

1.3.1.3 Principle of virtual displacements

Consider a body V, which is at the equilibrium state under an action of body forces ($\boldsymbol{f}_V$), surface forces ($\boldsymbol{f}_S$), and displacements ($\boldsymbol{u}_S$). Under such conditions displacements fields ($\boldsymbol{u}(\boldsymbol{r})$), deformations and stress fields ($\boldsymbol{\varepsilon}(\boldsymbol{r})$) and ($\boldsymbol{\sigma}(\boldsymbol{r})$), respectively, appear inside the body. If the displacements of the body ($\boldsymbol{u}$) at its equilibrium state show the infinitesimal increments ($\delta\boldsymbol{u}$) (Equation 1.16), which are compatible with both geometrical and kinematic constrains (superimposed on the body), then such additional displacements are called virtual displacements (Harris, 1959).

$$\left(\boldsymbol{u}\big|_{S_1} = \boldsymbol{u}_S \quad \Rightarrow \quad \delta\boldsymbol{u}\big|_{S_1} = 0\right) \tag{1.16}$$

When a body is in the equilibrium state subjected to virtual displacements, the work done by external forces is equal to the change in potential energy (δU) due to virtual displacements (Equation 1.17).

$$\int_V \boldsymbol{f}_V \cdot \delta\boldsymbol{u} dV + \int_{S_2} \boldsymbol{f}_S \cdot \delta\boldsymbol{u} dS = \delta U \tag{1.17}$$

δU can be considered as the internal virtual work done by the stresses (Equation 1.18):

$$\delta U = \int_V \boldsymbol{\sigma} : \delta \boldsymbol{\varepsilon} \, dV \tag{1.18}$$

For dynamic problems the first term in Equation 1.17 can be rewritten as:

$$\int_V \boldsymbol{f}_V \cdot \delta \boldsymbol{u} dV = \int_V \boldsymbol{F} \cdot \delta \boldsymbol{u} dV - \int_V \rho \ddot{\boldsymbol{u}} \cdot \delta \boldsymbol{u} dV \tag{1.19}$$

where $\boldsymbol{F}$ is the prescribed body force.

The principle of virtual displacements is also valid for large deformations. In this case Equation 1.17 should be written using more complex measures of stresses and strains.

1.3.1.4 Cohesive Zone Model (CZM)

Fracture mechanics can be performed on a variety of length scales ranging from a global (macroscopic) scale to a micro- (atomic) scale. The transition of stresses and displacements from a macro- to micro-scale is performed by use of local approaches. A general concept of the local approach is that the global failure of material is initiated by the local behavior in the area where stresses concentrations exist (i.e. crack tip). One of the local approaches is the *cohesive zone modeling*, which has been successfully employed to simulate fracture in ice by Wang, et al. (2006), Paavilainen, et al. (2009), Gürtner (2009b) and Konuk, et al. (2009a,b). Cohesive zone model (CZM) is a relatively new phenomelogical model, used mainly for the numerical simulations of crack propagation and it is based on previous works by Dugdale (1960), Barrenblatt (1962), Needleman (1987) and Tvergards (1990a, 1990b). Hillerborg, et al. (1976) applied the cohesive model to brittle fracture using the finite element method. Needleman (1987) was probably the first, who used the CZM for the crack propagation analysis of ductile materials. In recent years, many scientists use CZMs in many numerical investigations (e.g. a crack growth in ductile and brittle materials, interface debonding, analysis of a sandwiched structures), where the cohesive element technique is incorporated within the classical finite element frameworks. It should be noted that convergence proofs for the cohesive element technique are still in a development stage (Konuk, et al., 2009a).

The idea of CZM is based on the consideration that stresses at the crack tip are finite. The crack tip is divided into two zones (Figure 1.12): a "*Traction free surface*" and "*Traction on surfaces*". The traction free surface corresponds to the physical length of crack, which is a stress free; and the traction on surfaces is the fracture process zone (FZP), where the yielding and degradation of material occur. It is loaded by a finite stress called traction stress or cohesive stress (T).

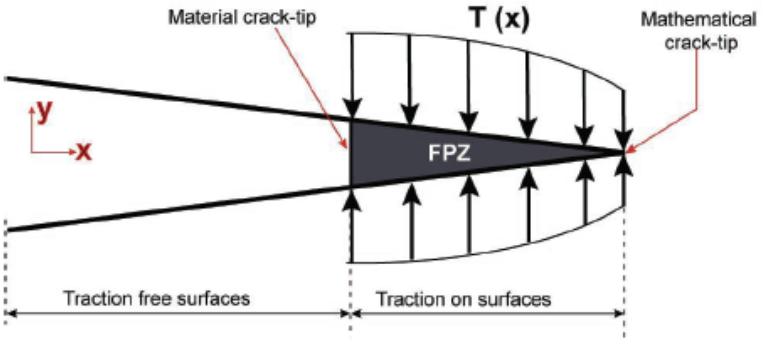

Figure 1.12 - A crack model, where FZP is a fracture process zone and traction ($T(x)$) is a function of distance from the crack tip (Gürtner, 2009b).

Most of recently developed CZMs are based on a mathematical framework of the conventional finite element method. In the cohesive model implemented into ABAQUS 6.8 finite element code, the cohesive stress is considered as a function of material separation and not of the distance from the crack tip. In the finite element representation of the CZMs, cohesive elements are inserted as an interface between continuum elements, and the damage, occurring in the element interfaces, follows a constitutive equation named cohesive law (Scheider and Brocks, 2003a), see Figure 1.13. If assume that each of these cohesive elements contains sufficient information about the crack growth in Mode I in the material, the cohesion-decohesion behavior for the Mode I can be obtained by applying a tensile load on a single element. The area under the cohesion-decohesion curve can be considered as the energy of separation and the cohesion-decohesion curve can be considered as the traction-separation law (TSL) for cohesive elements. In this model the crack can propagate only along element boundaries. Separation (δ) in these cohesive elements is calculated from the difference in displacements of continuum elements adjacent to them. A cohesive element fails when the maximum opening (δ_0) named critical separation is reached. The maximum traction (T_0) of cohesive strength is defined as a stress at the surface of continuum element. T_0 and δ_0 are used as fracture parameters of the material.

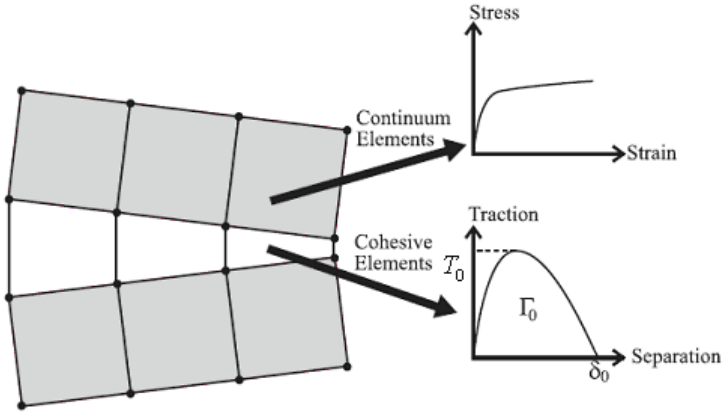

Figure 1.13 - A cohesive zone obeying a traction-separation law and the surrounding undamaged material (Anvari, 2008).

The post-failure behavior of a cohesive element is defined either by the specified shape of TSL and by the value of critical separation or by the TSL shape and by the value of cohesive energy (Γ_0). Γ_0 is the energy absorbed by the cohesive element, calculated as:

$$\Gamma_0 = \int_0^{\delta_0} T(\delta) d\delta \tag{1.20}$$

It should be noted that the δ can occur in normal or tangential directions. The value of Γ_0 can be obtained experimentally as it coincides with the J - integral at the crack initiation.

Cohesive laws

According to Anvari (2008), most of scientists, working with the CZM, can be split in two main groups based on their beliefs: *Group 1*, which claims that the shape of TSL does not have or has very little influence on the behavior of crack growth (Lin, et al., 1998; Needleman, 1990; Siegmund and Needleman, 1997; Tvergaard and Hutchinson, 1992) and *Group 2*, which has belief in the effect of TSL shape (Falk, et al., 2001; Scheider and Brocks, 2003b; Zhang, et al., 2003). For example, Scheider and Brocks (2003b) write that the influence of TSL on the result of calculations is strong, and the values of the cohesive parameters depend on the choice of that function and that the transferability of parameters from one TSL to another is not satisfied. Uncertainties regarding a physical meaning of TSL for cohesive elements are discussed in Anvari (2008).

Only few studies, where the cohesive model was employed to simulate ice fracture processes, were done. Figure 1.14 illustrates different cohesive laws adopted for ice by Paavilainen, et al. (2009), Gürtner, et al. (2008) and Wang, et al. (2006).

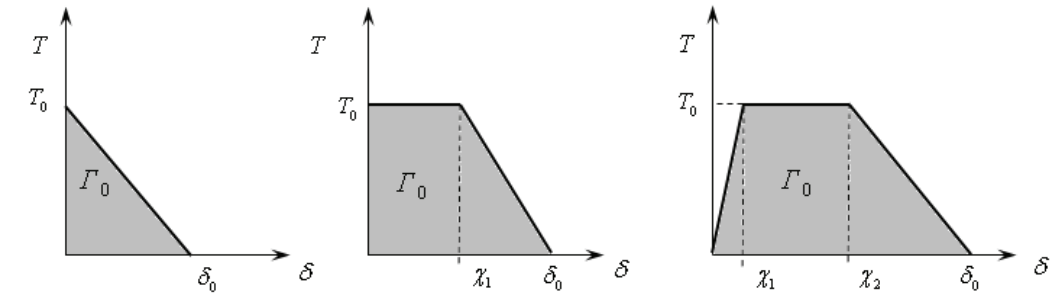

(a) linear (b) bilinear (c) trilinear

Figure 1.14 - Cohesive laws adopted for the modeling of ice failure by Paavilainen, et al. (2009) (a); for the modeling of sea ice breakup in McMurdo Sound by Wang, et al. (2006) (b) and for the modeling of in-plane fracture of model ice by Gürtner, et al. (2008) (c); (T_0 - maximum traction; Γ_0 - cohesive energy; δ_0 - critical separation; χ_1 and χ_2 - separation measures).

In Paavilainen, et al. (2009) the linear softening behavior (Figure 1.14a) is considered as a material property. In Gürtner, et al. (2008) the utilized cohesive law (Figure 1.14c) is regarded as a phenomenological characterization of FPZ and the maximum traction is related to the tensile capacity of ice, while Wang, et al. (2006) mentioned that the particular shape of traction-separation curve (Figure 1.14b), describing cohesive law, is regarded as a material property.

1.3.2 Background and basic equations of finite element method

1.3.2.1 Concept of FEM

The general idea of FEM is that any continuous variables (e.g. temperature, displacement, pressure) can be approximated by a discrete model, which is built-up on the set of piecewise-continuous functions. These functions are defined on a finite number of subdomains via values of a continuous quantity at a finite number of points in the considered region.

At present, FEM has become a numerical technique for finding approximate solutions of partial differential equations (PDE) and integral equations. Today, the FEM as well as many other state-of-the-art numerical methods are used mainly to gain insights into key variables and their causes and effects or to construct reasonable arguments as to why events can or cannot occur based on the numerical model, or to make qualitative or quantitative predictions about the future.

According to Eckard (2009), the finite-element analysis serves the opportunity to speed-up the design process. One of the advantages of using FEM is that any type of domain and boundary conditions can be handled including multi-material domains.

The vector $\boldsymbol{u}(\boldsymbol{r})$ is defined within a domain (V) limited by a surface (S). The main conception of FEM is a building of discrete-element model of the domain and a continuous function (a trial function). In order to do this the domain V has to be approximated by a finite number of subdomains called finite elements (FE). This process is referred to as discretization. The vector-function $\boldsymbol{u}(\boldsymbol{r})$ is interpolated at every FE by a polynomial function which is defined by nodal values of $\boldsymbol{u}(\boldsymbol{r})$.

1.3.2.2 Discretization of a domain (FE model)

A region V subdivided into a finite elements can be written as $V^{(e)}, e = \overline{1, n_e}$, where n_e is the total number of FEs. Every FE shares its nodes with other FEs and the nodes are numbered as $J, J = \overline{1, n_p}, n_p$ is the total number of nodes. The FE model is characterized by the global coordinate vector ($\boldsymbol{X}$) (Equation 1.21).

$$\boldsymbol{X}^T = \left\{\ldots, X_j{}^T, \ldots\right\}_{J=\overline{1,n_p}} \tag{1.21}$$

A coordinate vector of FE nodes $\boldsymbol{x}^{(e)}$ is formed from $\boldsymbol{X}$ (Equation1.22).

$$\boldsymbol{x}^{(e)} = \left\{\ldots, x_i^{(e)T}, \ldots\right\}_{i=\overline{1,m_g}} = \boldsymbol{a}_g^{(e)}\boldsymbol{X} \tag{1.22}$$

where $\boldsymbol{a}_g^{(e)}$ is the incidence matrix.

The choice of element type and its configuration as well as the number of nodes depends on the considered problem and required accuracy.

1.3.2.3 Construction of a FE trial function

Nodal values of an unknown function and, if necessary, values of its derivatives are considered as basic variables (i.e. degrees of freedom or DOFs). Let's introduce the $\boldsymbol{U}$, as a global vector of nodal unknowns for the whole body and the $\boldsymbol{u}^{(e)}$ as a local vector of the nodal unknowns of an element (Equation 1.23).

$$\boldsymbol{U}^T = \left\{\ldots, U_J^T, \ldots\right\}_{J=\overline{1,n_p}};\ \boldsymbol{u}^{(e)} = \boldsymbol{a}_f^{(e)}\boldsymbol{U} \tag{1.23}$$

where $\boldsymbol{a}_f^{(e)}$ is the incidence matrix (often called the connectivity matrix).

If the nodal values of an interpolation function are taken as the DOFs of a FE, then such element is called Lagrange element; if the values of derivatives are used then the FE is called Hermite element.

After the choice of nodal unknowns, a polynomial interpolation is constructed. The polynomial is based on the law of change of the unknown function within the domain of FE and it is expressed through values of unknown function at nodes.

The displacement vector $\boldsymbol{u}^T = (u_1, u_2, u_3)$ in an arbitrary point of FE (e) and its position vector $\boldsymbol{x}^T = (x_1, x_2, x_3)$ can be written as following:

$$\boldsymbol{u} = \boldsymbol{N}^{f^{(e)}}\boldsymbol{u}^{(e)} = \boldsymbol{N}^{f^{(e)}}\boldsymbol{a}_f^{(e)}\boldsymbol{U} \tag{1.24a}$$

$$\boldsymbol{x} = \boldsymbol{N}^{g^{(e)}}\boldsymbol{x}^{(e)} = \boldsymbol{N}^{g^{(e)}}\boldsymbol{a}_g^{(e)}\boldsymbol{X} \tag{1.24b}$$

where $\boldsymbol{N}^{f^{(e)}}$ is the matrix of polynomial interpolants (shape functions); $\boldsymbol{N}^{g^{(e)}}$ is the matrix of approximate functions.

1.3.2.4 Stiffness matrix and load vector of an element

Based on the strain tensor for small deformations $\boldsymbol{\varepsilon} = (\nabla \boldsymbol{u})^S$ a strain vector can be written as:

$$\boldsymbol{\varepsilon} = \boldsymbol{B}^{(e)} \boldsymbol{u}^{(e)} = \boldsymbol{B}^{(e)} \boldsymbol{a}_f^{(e)} \boldsymbol{U} \tag{1.25}$$

where $\boldsymbol{B}^{(e)}$ is the matrix which defines strains from nodal variables.

The relation between stresses and strains is linear (Equation 1.26).

$$\boldsymbol{\sigma} = \boldsymbol{D}^{(e)} \left(\boldsymbol{\varepsilon} - \boldsymbol{\varepsilon}_0 \right) + \boldsymbol{\sigma}_0 = \boldsymbol{D}^{(e)} \left(\boldsymbol{B}^{(e)} \boldsymbol{a}_f^{(e)} \boldsymbol{U} - \boldsymbol{\varepsilon}_0 \right) + \boldsymbol{\sigma}_0 \tag{1.26}$$

In Equation 1.26 $\boldsymbol{D}^{(e)}$ is the elasticity matrix, containing material properties; $\boldsymbol{\varepsilon}_0$ is the vector of initial strains (temperature strains) and $\boldsymbol{\sigma}_0$ is the initial stress vector.

Substituting Equations 1.25, 1.26 and 1.24a into Equation 1.27, which is the principle of virtual displacements written in the matrix form for a static problem, we get Equation 1.28.

$$\int_V \delta \boldsymbol{\varepsilon}^T : \boldsymbol{\sigma} \, dV = \int_V \delta \boldsymbol{u}^T \cdot \boldsymbol{f}_V \, dV + \int_{S_2} \delta \boldsymbol{u}^T \cdot \boldsymbol{f}_S \, dS \tag{1.27}$$

$$\boldsymbol{K}\boldsymbol{U} = \boldsymbol{F} \tag{1.28}$$

In Equation 1.28 following symbols are used:

$\boldsymbol{K} = \sum_{e=1}^{n_e} \boldsymbol{a}_f^{(e)^T} \boldsymbol{k}^{(e)} \boldsymbol{a}_f^{(e)}$ is the global stiffness matrix;

$\boldsymbol{k}^{(e)} = \int_{V^{(e)}} \boldsymbol{B}^{(e)^T} \boldsymbol{D}^{(e)} \boldsymbol{B}^{(e)} dV$ is the element stiffness matrix;

$\boldsymbol{F} = \sum_{e=1}^{n_e} \boldsymbol{a}_f^{(e)^T} \boldsymbol{f}^{(e)} = \sum_e \boldsymbol{a}_f^{(e)^T} \left(\boldsymbol{f}_V^{(e)} + \boldsymbol{f}_S^{(e)} + \boldsymbol{f}_{\varepsilon_0}^{(e)} + \boldsymbol{f}_{\sigma_0}^{(e)} \right)$ is the global vector of nodal forces, where the nodal forces are given by Equation 1.29.

$$\begin{aligned} \boldsymbol{f}_V^{(e)} &= \int_{V^{(e)}} \boldsymbol{N}^{f^{(e)^T}} \boldsymbol{f}_V dV \; ; \; \boldsymbol{f}_S^{(e)} = \int_{S_2^{(e)}} \boldsymbol{N}^{f^{(e)^T}} \boldsymbol{f}_S dS \\ \boldsymbol{f}_{\varepsilon_0}^{(e)} &= \int_{V^{(e)}} \boldsymbol{B}^{(e)^T} \boldsymbol{D}^{(e)} \boldsymbol{\varepsilon}_0 dV \; ; \; \boldsymbol{f}_{\sigma_0}^{(e)} = -\int_{V^{(e)}} \boldsymbol{B}^{(e)^T} \boldsymbol{\sigma}_0 dV \end{aligned} \tag{1.29}$$

In Equation 1.29 $\boldsymbol{f}_V^{(e)}, \boldsymbol{f}_S^{(e)}, \boldsymbol{f}_{\varepsilon_0}^{(e)}, \boldsymbol{f}_{\sigma_0}^{(e)}$ are FE vectors of nodal forces, which are equivalent to the acting body forces ($\boldsymbol{f}_V$), surface forces ($\boldsymbol{f}_S$), initial strains fields ($\boldsymbol{\varepsilon}_0$) and initial stresses fields ($\boldsymbol{\sigma}_0$) respectively. In a case of linear behavior, $\boldsymbol{K}$ is a linear factor of $\boldsymbol{U}$. It is independent of the stresses status and constant. For a case of nonlinear behavior the $\boldsymbol{K}$ is expressed as a function of the displacements. In order to form the matrix $\boldsymbol{K}$ and the right-hand-side of Equation 1.28 the FE type, number of DOFs, element connectivity, node data and material data have to be known.

To get the values of $\boldsymbol{U}$ matrix Equation 1.28 has to be solved. To solve a nonlinear problem, the vector $\boldsymbol{F}$ has to be divided into stages called increments. After the solution is found, displacements, stresses and strains at any point of the body can be calculated utilizing interpolation principles.

1.3.3 Formulation of cohesive model in ABAQUS

This subsection is based on ABAQUS 6.8 Documentation. It describes the cohesive model which was used in numerical experiments of this study. The presented information helps us understand commands used in the input files (Appendix D2) for the numerical simulations described in Section 1.5.

The cohesive zone is discretized with a single layer of cohesive elements (CEs) with a thickness close to zero. The constitutive equation of cohesive elements is established in terms of relative displacements (separations) and tractions across the interface. The vector Δ, defining separations of CE in terms of nodal displacements in global coordinates, is calculated from the displacements of adjacent continuum elements as the difference between displacements of top and bottom nodes (Equation 1.30a). In local coordinates separations ($\boldsymbol{\delta}$) can be obtained by Equation 1.30b.

$$\Delta = \boldsymbol{u}^{+} - \boldsymbol{u}^{-} = \boldsymbol{N}^{f(ce)}\boldsymbol{u}^{(ce)} \tag{1.30a}$$

$$\boldsymbol{\delta} = \boldsymbol{a}_f^{(ce)}\boldsymbol{N}^{f(ce)}\boldsymbol{u}^{(ce)} = \boldsymbol{B}^{(ce)}\boldsymbol{u}^{(ce)} \tag{1.30b}$$

In Equation 1.30a and 1.30b $\boldsymbol{u}^{+}$ and $\boldsymbol{u}^{-}$ are the displacements vectors of the top and bottom nodes of the element, respectively; $\boldsymbol{N}^{f(ce)}$ is the matrix of the CE shape functions; $\boldsymbol{u}^{(ce)}$ is the vector of CE nodal displacements in global coordinates;. $\boldsymbol{a}_f^{(ce)}$ is the transformation tensor; $\boldsymbol{B}^{(ce)}$ is the matrix connecting the $\boldsymbol{\delta}$ and $\boldsymbol{u}^{(ce)}$. For a three-dimensional problem the cohesive model assumes three components of separations (a normal separation (δ_N) and two tangential separations (δ_T and δ_S) and corresponding to them three traction components T_N, T_T, T_S.

Each of the traction stresses is a nonlinear function of separations and obeys bilinear law described farther in the text. The CE stiffness matrix (Equation 1.30c) is derived from the principle of virtual displacements.

$$\boldsymbol{k}^{(ce)} = \int_{\Omega^{(ce)}} \boldsymbol{B}^{(ce)^T} \boldsymbol{D}^{(ce)} \boldsymbol{B}^{(ce)} d\Omega \tag{1.30c}$$

where $\boldsymbol{D}^{(ce)}$ is the constitutive matrix of the CE which relates element tractions to element separations and the superscript *(ce)* defines parameters related to CEs.

1.3.3.1 Cohesive law

For a single variable response the constitutive equation for mixed-mode loading conditions is defined by a *penalty stiffness* (*K**) (Camanho and Davila, 2002), a damage evolution function (*d),* mixed-mode effective displacements (δ_m^d), corresponding to the damage , and effective displacements (δ_{0m}), corresponding to the complete failure of CE (i.e. total decohesion) as:

$$T = D^{(ce)} \delta \tag{1.31}$$

where $D^{(ce)}$ is the constitutive operator of CE, which depends on the state of cohesive element defined by a relation between δ_{0m}, δ_m^d and a maximum mixed-mode separation (δ_m^{max}) as described below. The mixed-mode softening law is illustrated in Figure 1.15.

Figure 1.15 shows the traction on the vertical axis (*Z*) and the magnitudes of the normal (representing) and the shear separations (shear Modes II and III) along the two horizontal axes (*Y,X*). The unshaded triangles in the two vertical coordinate planes represent a bi-linear response under a pure normal deformation (Mode I) on the *Y-Z* plane and a pure shear deformation (Mode II, Mode III) in the *X-Z* plane. All intermediate vertical planes (that contain the vertical axis) represent the damage response under mixed-mode conditions with different mode mixes and, therefore, any point on the *0-X-Y* plane represents mixed-mode separations. The dependence of damage-evolution data on the mode mix was defined analytically based on an energy definition.

Functions $T(\delta)$ under pure Mode I loading conditions and under pure Mode II or Mode III loading conditions are illustrated in Figure 1.16a and Figure 1.16b, respectively, which corresponds to a brittle material (Konuk, et al., 2009b).

A nonlinear relation between the traction and separation was considered. The model initially assumes linear-elastic behavior prior to damage. Same penalty stiffness in Modes I, II and III were assumed in order to reduce the number of unknown parameters in the model and, therefore, tractions before softening onset are:

$$T_i = K * \delta_i, \quad i = N, S, T \tag{1.32}$$

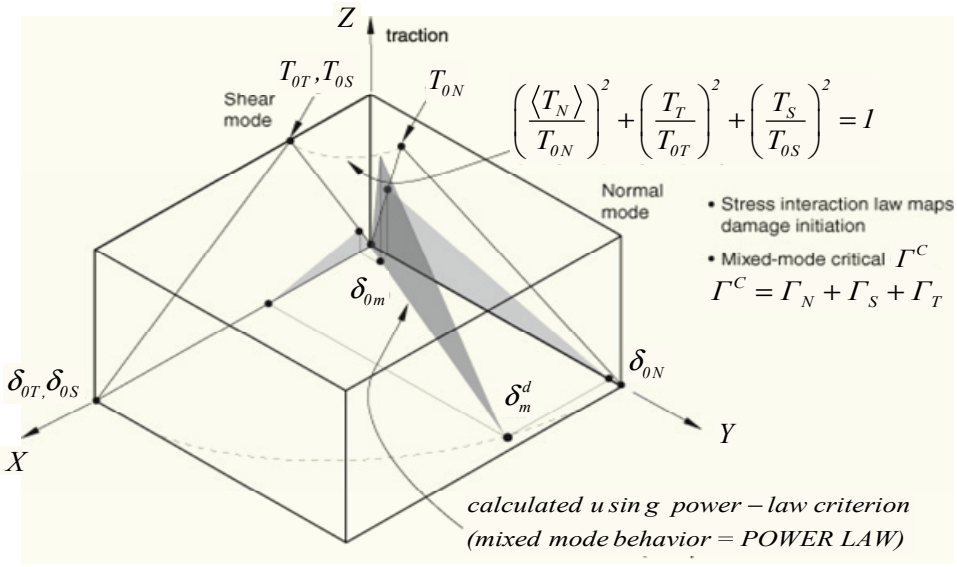

Figure 1.15 - A mixed-mode softening law (ABAQUS 6.8).

In Equation 1.32, T_i is the traction stresses in the direction i; δ are separations of CE; the symbol N denotes a normal direction and symbols S and T denote tangential directions.

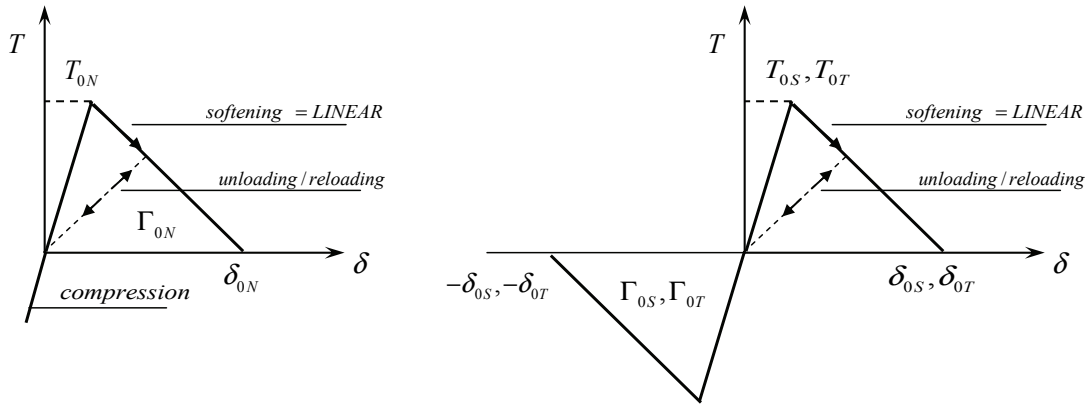

(a) Mode I (b) Mode II or Mode III

Figure 1.16 - A traction-separation law used to define the behavior of cohesive elements in pure normal (a) and two tangential (b) directions.

Under mixed-mode loading damage is assumed to be initiated when a quadratic interaction criterion involving the ratios of traction stresses reaches the value of one (Equation 1.33).

$$\left(\frac{\langle T_N \rangle}{T_{0N}}\right)^2 + \left(\frac{T_T}{T_{0T}}\right)^2 + \left(\frac{T_S}{T_{0S}}\right)^2 = 1 \tag{1.33}$$

where the Macauley bracket $\langle\ \rangle$ specifies that

$$\left(\frac{T_T}{T_{0T}}\right)^2 + \left(\frac{T_S}{T_{0S}}\right)^2 = 1$$

under compressive loading $(\delta_N \le 0)$. The cohesive layer does not undergo any damage under the pure compression. The aforementioned criterion was successfully used for the modeling of the delamination processes of composite materials (Camanho and Davila, 2002). The damage evolution (Equation 1.38) is defined based on the energy that is dissipated as a result of a damage process (cohesive or fracture energy). In order to account for the dependence of fracture toughness on the mixed-mode loading it was assumed that that failure under mixed-mode conditions is governed by a law written as:

$$\frac{\Gamma_N}{\Gamma_{0N}} + \frac{\Gamma_T}{\Gamma_{0T}} + \frac{\Gamma_S}{\Gamma_{0S}} = 1 \tag{1.34}$$

where Γ_N, Γ_T, and Γ_S refer to the work done by the traction and its conjugate relative displacement in the normal, the first, and the second shear directions, respectively; Γ_{0N}, Γ_{0T}, and Γ_{0S} refer to the specified critical fracture energies required to cause failure in the normal, the first, and the second shear directions, respectively.

Stress components of the traction-separation model are affected by damage (d) according to Equations 1.35 - 1.37.

$$\text{if } \bar{T}_N \ge 0 \text{ then } T_N = (1-d)\bar{T}_N \text{, otherwise no damage } (d=0) \tag{1.35}$$

$$T_S = (1-d)\bar{T}_S \tag{1.36}$$

$$T_T = (1-d)\bar{T}_T \tag{1.37}$$

where $\bar{T}_N$, $\bar{T}_S$ and $\bar{T}_T$ are stress components predicted by the elastic traction-separation behavior for the current strains without damage.

$$d = \frac{\delta_{0m}(\delta_m^{max} - \delta_m^d)}{\delta_m^{max}(\delta_{0m} - \delta_m^d)},\ d \in [0,1] \tag{1.38}$$

In Equation 1.38 $\delta_{0m} = 2\Gamma^C / T_{0eff}$, T_{0eff} is the effective traction at damage initiation; δ_m^{max} is the maximum value of the effective displacements ($\delta_m = \sqrt{\langle\delta_N\rangle^2 + \delta_S{}^2 + \delta_T^2}$) attained during the loading history; with assumed mode-mix, fracture energy $\Gamma^C = \Gamma_N + \Gamma_S + \Gamma_T$ when the condition (Equation 1.34) is satisfied.

The basic approach of described cohesive model is similar to the CZM in Gürtner (2009b), however, many details are different (e.g. function $T(\delta)$ under the pure normal and shear loading; formulations of the constitutive behavior under mixed-mode conditions, dependences of penalty stiffness on the direction, etc.).

1.3.3.3 Unloading of the cohesive elements

If due to a change of deformation direction the stress state removes from the limiting traction-separation curve the material elastic stiffness is reduced by damage as shown in Figure 1.16. The separation vanishes when the traction decreases to zero. Reloading subsequent to unloading also occurs along the same linear path until the softening envelope is reached.

1.3.4 ABAQUS solution to finite element equations

Only relevant methods, taken from the ABAQUS 6.8 Documentation, are given in this subsection.

ABAQUS version 6.8 solves a system of finite element equations implicitly, satisfying the differential equations at each time increment after the solution at previous increment is found (ABAQUS/Standard) or explicitly, marching a solution forward through time in small time increments without solving a coupled system of equations at each increment (ABAQUS/Explicit). Implicit methods implemented in ABAQUS can handle static, quasi-static, dynamic large deformation problems, involving nonlinearities. According to King (2009), implicit methods even with the fast sparse solvers and advanced algorithms struggle to solve sophisticated contact problems. Explicit methods can handle dynamic problems involving the most complex contact conditions.

1.3.4.1 Linear solution methods

Matrices assembled by a finite element procedure are generally very sparse. The ratio between nonzero elements and the total number of elements in the global matrix varies usually between 0.1 and 0.2 (Belov, 2004). Equation solvers that can deal with sparse matrices for the finite element analysis can be classified into two categories, the direct and the iterative solvers.

Direct multifrontal method (Gauss Elimination)

Consider a set of algebraic equations (Equation 1.28), where the $\boldsymbol{K}$ is the square coefficient matrix (stiffness matrix), $\boldsymbol{U}$ is the vector of unknown parameters (nodal unknowns), $\boldsymbol{F}$ is the vector of known values (specified forces).

ABAQUS uses a multifrontal method to solve Equation 1.28. The solution procedure consists of (i) a triangular decomposition of $\boldsymbol{K}$ by utilizing Gauss elimination principle and (ii) a backward substitution technique to compute unknown DOFs. The process of

Gauss elimination reduces the matrix $\boldsymbol{K}$ to the upper triangular matrix by the operations performed in the coefficient array.

A general idea of the multifrontal method is simultaneous assembly of equations and eliminating unknowns. The multifrontal solution method (Duff and Reid, 1973; Kwon, et al., 2003) is an extension of the frontal solution scheme (Irons, 1970; Fialko, 2003; Belov, 2004) and it is able to deal with multiple frontal matrices[1], which results in a significant reduction of total operation counts.

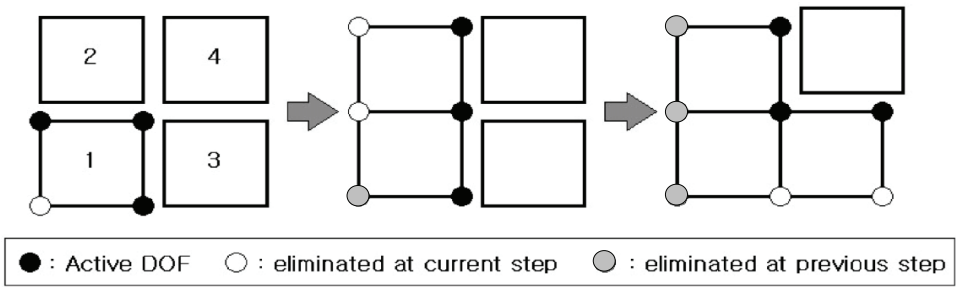

Figure 1.17- The procedure of the frontal solution algorithm (Kwon, et al., 2003).

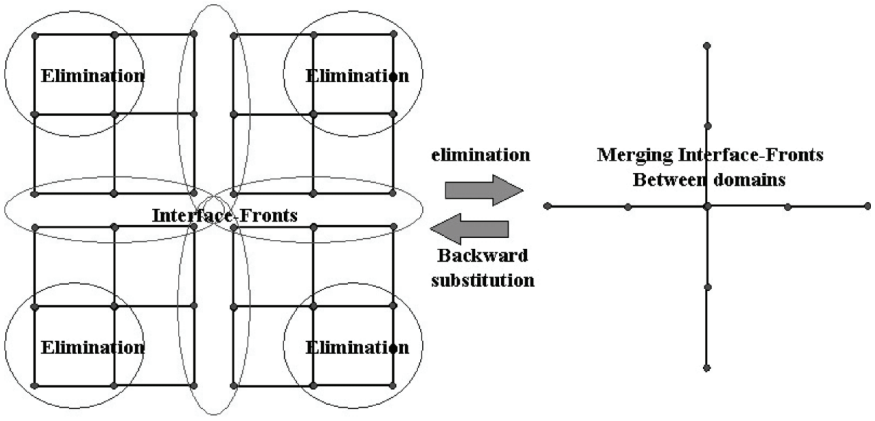

Figure 1.18 - The procedure of the multifrontal solution algorithm with four independent wave fronts being employed (Kwon, et al., 2003).

In contrast to the frontal method (Figure 1.17), where only those equations that are actually required for the elimination of specific unknowns are assembled, several independent fronts (Figure 1.18) (frontal matrices) are employed in the multi-frontal method. Later these fronts are merged completely.

Multifrontal solution method is now considered as one of the most efficient direct solvers for general sparse systems of linear equations from standpoint of computation, memory requirements, and parallel speedup (Kim, et al., 2005). This method requires precise node numeration.

[1]In frontal solution scheme as soon as the coefficients of an equation are assembled from the contributions of all relevant elements to a dense matrix called 'frontal matrix', the corresponding variables are eliminated.

Iterative method

Iterative methods based on a successive approximation of the solution in the following form:

$$\boldsymbol{U}_{n+1} = \boldsymbol{G}\boldsymbol{U}_n + \boldsymbol{r}_n \tag{1.39}$$

where $\boldsymbol{G}$ is the transition matrix; $\boldsymbol{r}_n$ is a vector.

For linear systems ABAQUS utilizes the domain decomposition method based on Finite Element Tearing and Interconnecting (FETI) algorithm, which solves a boundary value problem by splitting it into smaller problems on subdomains and iterating to coordinate the solution between adjacent subdomains. General principle of FETI method is that the FEM is silted into non-overlapping sets of elements called subdomains. The stiffness matrix for each subdomain is factored independently with a direct solver described above and immediately saved in memory. Then, a system of Lagrange multipliers is formed and solved with preconditioned conjugate gradient (PCG) iteration algorithm. An approximate solution is recovered from subdomain solutions and Lagrange multipliers.

1.3.4.2 Nonlinear solution methods

Nonlinearities arises from large-displacement effects (large strains, rotations, etc.), material nonlinearity (plasticity, creep, etc.) and boundary nonlinearities (contact, friction). Nodal displacements in this case are considered functions of time. To solve a nonlinear system of equations ABAQUS uses several methods in which the solution is obtained as a series of increments. Among them are Newton's method, BFGS (Broyden, Fletcher, Goldfarb, Shanno) method and direct cyclic algorithm (modified Newton's method in conjunction with a Fourier representation of the solution and the residual vector). In this study Newton's method was used to solve nonlinear system of FE equations.

Newton's method

In Newton's method the solution to a nonlinear system of algebraic equations (Equation 1.40), which arises from the finite element discretization of a system of nonlinear partial differential equations, is procured by iteratively solving a sequence of linear systems of obtained via Taylor series expiation of the left-hand-side of Equation 1.40 in the vicinity of an assumed solution.

$$\boldsymbol{K}(\boldsymbol{U})\boldsymbol{U} - \boldsymbol{F} = 0 \tag{1.40}$$

Newton's iteration scheme can be written as:

$$\boldsymbol{U}_{n+1} = \boldsymbol{U}_n - \boldsymbol{J}^{-1}(\boldsymbol{U}_n)\boldsymbol{rs}(\boldsymbol{U}_n) \tag{1.41}$$

where $\boldsymbol{U}_n$, $\boldsymbol{U}_{n+1}$ are two consequent approximations of the solution;

$\boldsymbol{rs}(\boldsymbol{U}_n) = \boldsymbol{K}(\boldsymbol{U}_n)\boldsymbol{U}_n - \boldsymbol{F}$ is the residual vector;

$\boldsymbol{J}(\boldsymbol{U}_n) = \dfrac{\partial \boldsymbol{rs}(\boldsymbol{U}_n)}{\partial \boldsymbol{U}_n}$ is the tangent stiffness matrix (Jacobi matrix);

The termination of the iteration procedure is determined by convergence criteria, ensuring that the residual is very small and the difference between successive solutions is less than a specified tolerance (ξ), see Equation 1.42.

$$\left\| \boldsymbol{U}_{n+1} - \boldsymbol{U}_n \right\| \le \xi \tag{1.42}$$

Nonlinear dynamics

A finite element approximation of equilibrium equations, formulated for dynamic problems, can be written as:

$$\boldsymbol{M}\ddot{\boldsymbol{U}} + \boldsymbol{K}\boldsymbol{U} = \boldsymbol{F} \tag{1.43}$$

where $\boldsymbol{M}$ is the "consistent" mass matrix, obtained by consistent use of the interpolation. If the first-order elements (provided with linear interpolation) are used, then $\boldsymbol{M}$ is the diagonal lumped mass matrix, obtained by adding the each row of the consistent matrix onto the diagonal. The methods, available in ABAQUS for the analysis of dynamic linear and nonlinear problems, use explicit or implicit integration operators. ABAQUS/Standard uses implicit the Hilber-Hughes-Taylor operator, introduced by Hilber, et al. (1978) for integration of Equation 1.43. The integration operator matrix must be inverted and a set of nonlinear equilibrium equations must be solved at each time increment. ABAQUS/Explicit uses the central-difference operator and diagonal element mass matrixes.

The Hilber, Hughes and Taylor operator

The operator solves the following modified equilibrium equations:

$$\boldsymbol{M}\ddot{\boldsymbol{U}}_{t+\Delta t} + (1+\alpha)(\boldsymbol{K}\boldsymbol{U}_{t+\Delta t} - \boldsymbol{F}_{t+\Delta t}) - \alpha(\boldsymbol{K}\boldsymbol{U}_t - \boldsymbol{F}_t) + \boldsymbol{L}_{t+\Delta t} = 0 \tag{1.44}$$

where the subscript t refers to time and Δt refers to the time step; α is the parameter, which controls the amount of numerical damping; $\boldsymbol{L}$ is the sum of all Lagrange multiplier forces. The operator definition is completed by Newmark's equations in a standard form:

$$\boldsymbol{U}_{t+\Delta t} = \boldsymbol{U}_t + \Delta t \dot{\boldsymbol{U}}_t + \left(\frac{1}{2} - \beta\right)\Delta t^2 \ddot{\boldsymbol{U}}_t + \beta \Delta t^2 \ddot{\boldsymbol{U}}_{t+\Delta t} \tag{1.45}$$

$$\dot{\boldsymbol{U}}_{t+\Delta t} = \dot{\boldsymbol{U}}_t + (1-\gamma)\Delta t \ddot{\boldsymbol{U}}_t + \gamma \Delta t \ddot{\boldsymbol{U}}_{t+\Delta t} \tag{1.46}$$

where β and γ are parameters of the operator. Equations 1.44, 1.45 and 1.46 are solved iteratively, for each time step, for each displacement DOF of the structural system.

The central-difference operator

The equilibrium Equation 1.43 is explicitly integrated using following rule:

$$\boldsymbol{U}^{i+1/2} = \dot{\boldsymbol{U}}^{i-1/2} + \frac{\Delta t^{i+1} + \Delta t^{i}}{2} \ddot{\boldsymbol{U}}^{i} \tag{1.47}$$

$$\boldsymbol{U}^{i+1} = \dot{\boldsymbol{U}}^{i} + \Delta t^{i+1} \dot{\boldsymbol{U}}^{i+1/2} \tag{1.48}$$

In Equation 1.47 and 1.48 the superscript *i* refers to the increment number *i-1/2* and *i+1/2* refer to the mid-increment values.

1.4 Analysis of Freeze-Bond Shear Strength Experiments

In this section a summary of the experiments used to study the freeze-bond behavior under shear conditions is given. The first part of the section describes the experimental setup and the second part presents ice characteristics used in the freeze-bond experiments. Information presented in the second part is based on data obtained via personal communication with A. Repetto-Llamazares.

1.4.1 Experiment description

Model experiments were performed in the Hamburg Ship Model Basin (HSVA) in order to study freeze-bond shear strength. A detailed description of the experimental procedure can be found in Repetto-Llamazares, et al. (2009b). Only a brief summary is given here. Two ice blocks (HSVA model ice) with dimensions 0.14 x 0.14 x 0.03m were brought together in contact and submersed below water level allowing FB to form (Figure 1.19). After a specific time adfrozen ice blocks were taken out of the water and tested for direct shear at constant velocity of 0.7mm/s. A total of 58 experiments were performed. Eight of these were taken from rafted layers of ice found in model ridges, described in Repetto-Llamazares, et al. (2009a). The main parameters varying during the experiments were: (i) confining pressure during the test and freezing; (ii) ice temperature prior submersing; (iii) submersion time (Table 1.1).

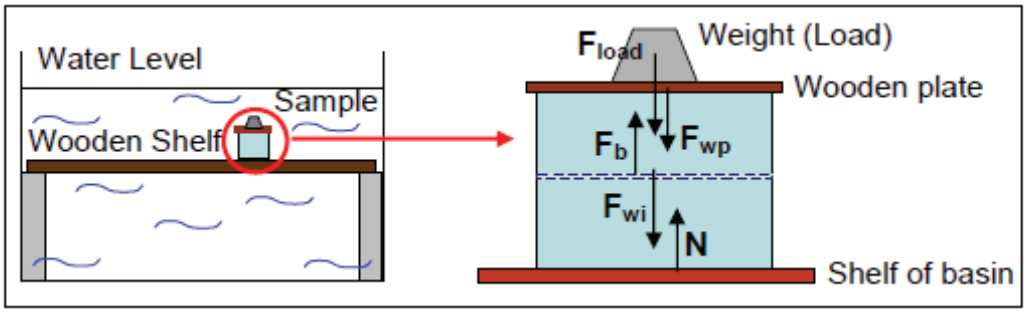

Figure 1.19- Scheme of how the ice blocks were loaded during submersion and the forces involved. (F_{load} - force exerted by the weight on top of the ice, F_{wp} - weigh of the wooden plate, F_b - buoyancy force, F_{wi} - total weight of ice, N-reaction force) (Repetto-Llamazares, et al., 2009b).

Table 1.1 - Parameters used in each experiment: initial temperature of the ice (τ_i), normal stress applied while making the freeze-bond and while testing them (σ) and time of submersion of the samples (Δt) (Repetto-Llamazares, et al., 2009b).

Test#	τ_i (C°)	σ (Pa)	Δt (hr)
10110	-7.5	125 637 1205 2040	20
10120	-14	125 637 1205 2040	20
10130	-1.2	147 295 637 2040	20
10210	-7.5	637	1 4.5 10
10220	-12	637	1 4.5 10
10410 Ridge 3000	-1.3	185 365 305 1380	20
10510 Ridge 4000	-1.7	205 205 245 187	9

1.4.2 Ice characteristics

Thin sections of some ice samples (HSVA ice) were examined in the polarized light. In this study it was assumed that the ice used during tests had a similar microstructure. A vertical thin section of ice found in the consolidated layer of a model ridge is illustrated in Figure 1.20a. The consolidated layer consists of two pieces of frozen-together rafted ice with the thickness approximately 30-35 mm. To increase brittleness of the ice and reduce its density air bubbles (diameter $200\,\mu m$ to $500\,\mu m$) were incorporated into the model ice (Figure 1.20b) (Evers and Jochmann, 1993). From Figure 1.20 it can bee seen that the internal structure of ice is not completely homogeneous. Granular ice is embedded into the columnar structure (Figure 1.20a).

Presence of a freeze-bond disturbs uniform distribution of air bubbles along the ice thickness (Figure 1.20b). Within the freeze-bond area crystals differ from the rest of the ice and no air is trapped into the crystal structure. Besides, there are voids of different size, shape and spacing between them.

1.5 Finite Element Modeling of the Freeze-bond Shear Strength Experiments

From a series of experiments described in Section 1.4 one ice sample was chosen for the numerical simulation. The sample showed brittle fracture and freeze-bond shear capacity of 205N for initial ice temperature of -14°C and a submersion time of 20hours.

1.5.1 Initial data

A rational model describing the geometry of tested ice sample and the testing device, which is able to take into account static and inertial properties of the whole experimental procedure, is shown in Appendix A.

Geometrical characteristics of the model are given in Figure 1.21. An approximate value of freeze-bond thickness obtained from the thin section in Figure 1.20b is equal to 5-6mm. It should be noted that the 'true' (exact) value of FB thickness for a given ice sample might not be 5mm as the thin section analyses were done only for few rafted ice samples found in model ice-ridge and not for the considered ice sample.

Properties of material (HSVA ice) are given in Table 1.2.

Table 1.2 - Properties of HSVA ice

Properties	Values
density	850kg/m^3
elastic modulus	50MPa-350MPa, (Evers Jochmann, 1993)
Poison's ratio	0.3
flexural strength	20-160kPa, (Evers Jochmann, 1993)
unconfined compressive strength (vertical)	140-230kPa, (Evers Jochmann, 1993)
unconfined compressive strength (horizontal)	115-155kPa, (Evers Jochmann, 1993)

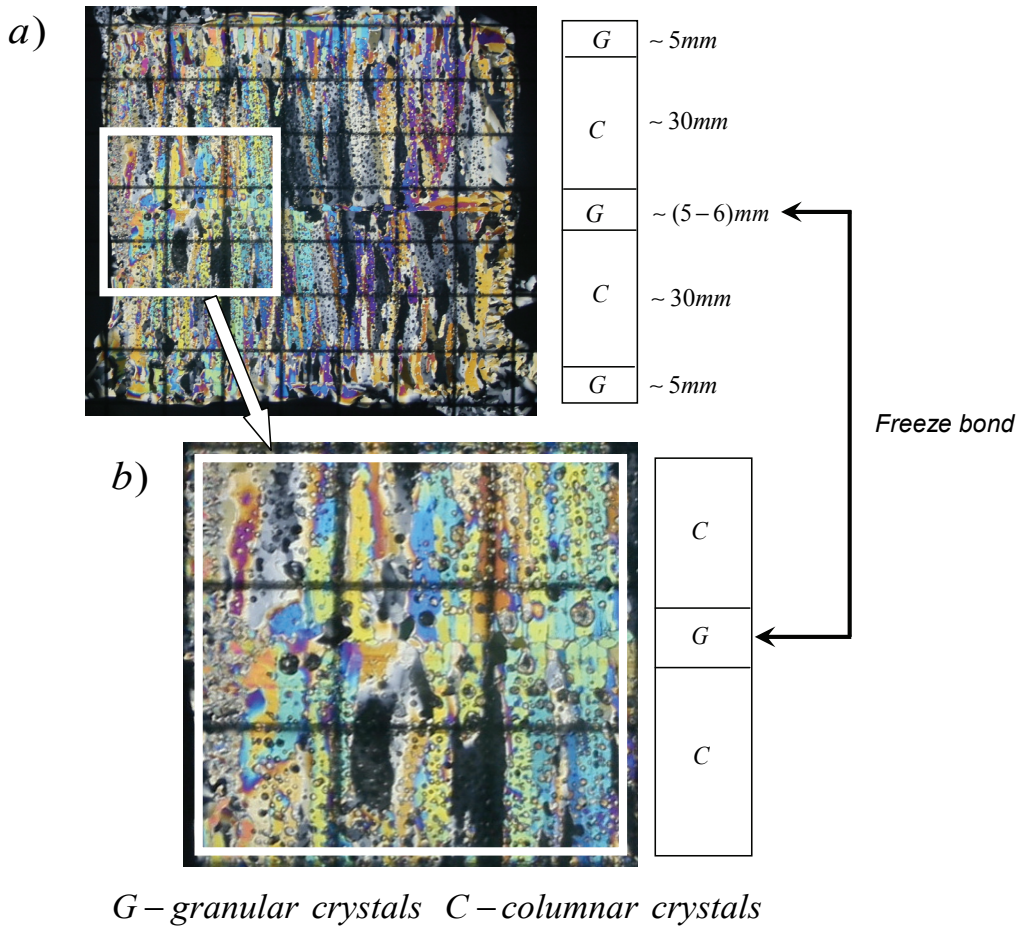

Figure 1.20 - Vertical thin section of a consolidated layer, layers of columnar and granular crystals): (a) - Complete view of the ice sample; (b) - Magnified part of the freeze-bond area.

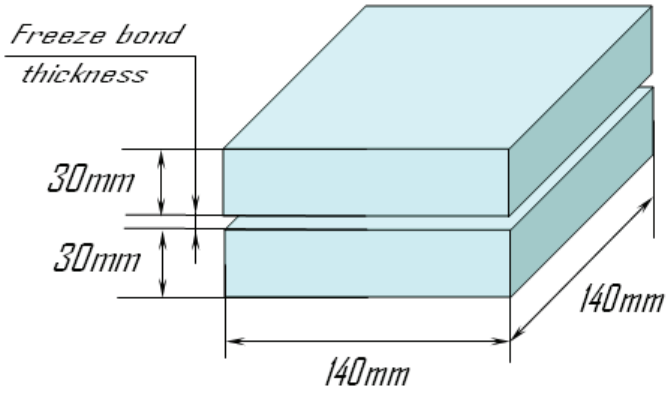

Figure 1.21 - Geometry of the tested ice sample.

1.5.2 Finite element model

The three-dimensional (Figure 1.22a) and two-dimensional models (Figure 1.22b) considered in this study consisted of solid (volumetric) parts and a cohesive layer inserted between them. Solid parts represent the ice blocks and the cohesive layer is attributed to the freeze-bond between them.

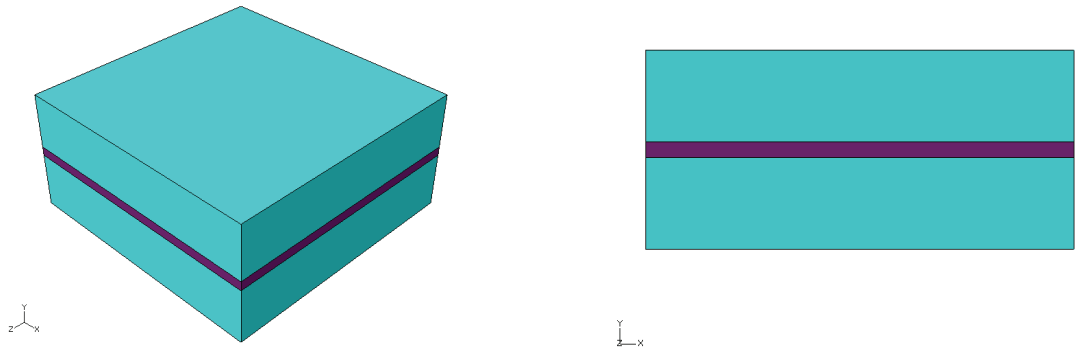

(a) (b)

Figure 1.22 - Model of tested ice sample with solid parts and a cohesive layer. The three-dimensional (a) and the two-dimensional (b) model.

1.5.2.1 Material parameters and assumptions

For the present set of experiments both the cohesive law (TSL) and the constitutive behavior of model ice were not known. Moreover, ice failure processes in the presence of freeze-bond were poorly investigated. Hence, several assumptions regarding the constitutive behavior of the model ice and the behavior of freeze-bond were made:

1. Shafrova (2007) showed that the freeze-bond strength is lower than the ice strength. In the model it was assumed that during shear tests ice fails along the freeze-bond and a plastic state in ice itself is not reached. Elastic properties of ice used in the simulations are given in Table 1.3. The values in Table 1.3 were based on the values in Table 1.2.

Table 1.3- Elastic material properties

Properties	Labels	Values
Elastic Modulus	E	200 MPa
Poisson's ratio	ν	0.3
Density	ρ	810 kg/m^3

2. The freeze-bond failure is assumed to be brittle and triangular cohesive law (Figure 1.16), as it well represents brittle behavior, was assumed for the freeze-bond area. Cohesive law parameters were retrieved by trial and error to match FE solution with experimental results. Density of the freeze-bond was assumed to be equal to the density of tested ice (810kg/m^3).

In reality, as the freeze-bond fails, a frictional sliding of the surfaces should be taken into account. According to Scheider (2001), determination of friction coefficient of fracture surfaces is a difficult task. From the experiments (Section 1.4) it was found that after the short distance of sliding the ice-ice friction changes significantly, and the sliding mechanism was not clear. Due to high uncertainty regarding frictional behavior of ice, the sliding was not implemented in the numerical model described in this section.

Extraction of CE parameters

Procedure of extraction of CE parameters (K^*, T_0 and Γ_0) followed the algorithm as it is described below.

1. The values of normal and tangential CE stiffness (K^*_N , K^*_T, K^*_S) were chosen such that the experimental loading slope was equal to the slope obtained through the numerical solution (Figure 1.23). For simplicity it was assumed that $K^*_N = K^*_T = K^*_S$.

2. The value of maximum traction (T_0) in normal and tangential directions was chosen such that the maximum force in experiments was equal to the maximum force in numerical calculations (Figure 1.24). It was assumed that the values of maximum normal and tangential tractions are the same $T_{0N} = T_{0T} = T_{0S}$.

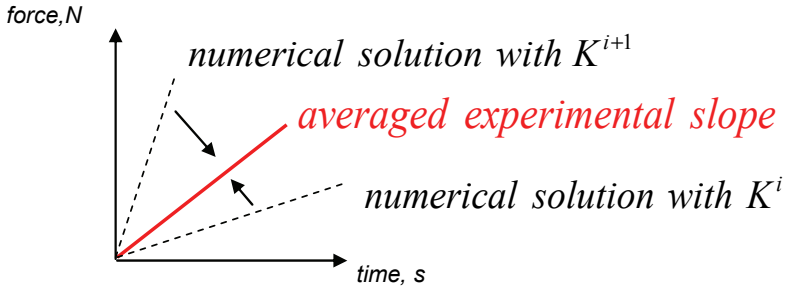

Figure 1.23 - Tuning procedure of CE stiffness (K^*); the subscript i denotes trial number.

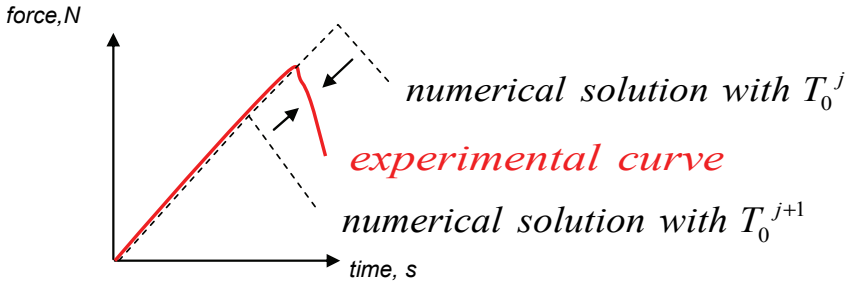

Figure 1.24 - Tuning procedure of CE maximum traction, T_0; the subscript j denotes trial number.

3. The value of cohesive fracture energy Γ_0 in normal and tangential directions was chosen such that the post-failure behavior obtained via numerical calculations was relatively close to the post-failure behavior in the experiments (Figure 1.25). It was assumed that the values of normal and tangential cohesive fracture energies are the same $\Gamma_{0N} = \Gamma_{0T} = \Gamma_{0S}$. Since the smaller the angle between the loading slope and post-failure slope the more the iterations needed to reach the convergence of solution, the value of cohesive fracture energy was limited by the convergence requirements.

The commercial finite element code ABAQUS 6.8 was used to make a 2D plane stress, plane strain and 3D model of the shear setup. As a computational model can not be fully verified, guaranteeing 100% error-free implementation (Macal, 2005), simple case was tested in ABAQUS 6.8 in order to increase the degree of statistical certainty of the finite element code (see Appendix D).

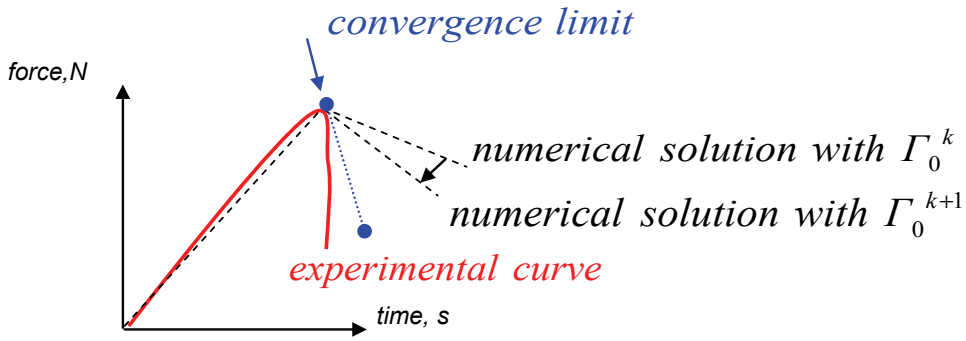

Figure 1.25 - Tuning procedure of cohesive fracture energy (Γ_0); the subscript k denotes a trial number.

1.5.2.2 Model discretization

Two families of finite elements were used in the simulations (Table 1.4).

Table 1.4 - Finite elements used in numerical simulations

Model	Solid elements	Cohesive elements
Two-dimensional formulation	CPE4; SPS4	COH2D4
Three-dimensional formulation	C3D8	COH3D8

Characteristics of used elements are given below.

Cohesive elements

COH2D4 is a 4-node two-dimensional cohesive element with two degrees of freedom in each node. It can be used to model the behavior of adhesive joint interfaces in composites, etc., where the integrity and strength of interfaces may be of interest. The geometry of the element is shown in Figure 1.25.

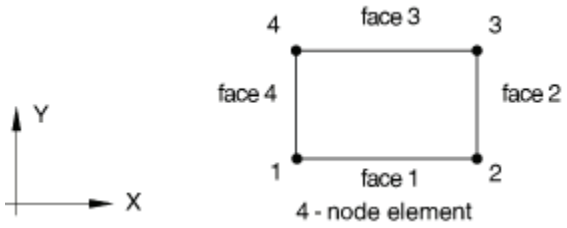

Figure 1.26 - Geometry of the element COH2D4 (ABAQUS 6.8).

COH3D8 is an isoparametric 8-node three-dimensional cohesive element with three degrees of freedom at each node and it can be used in the same way as COH2D4. The geometry of the element is shown in Figure 1.27.

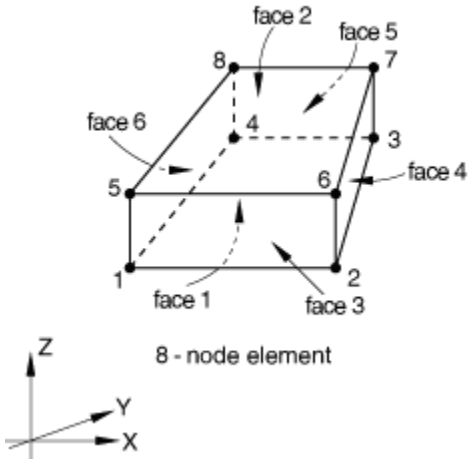

Figure 1.27 - Geometry of the element COH3D8 and C3D8 (ABAQUS 6.8).

Solid elements

CPE4 is an isoparametric 4-node bilinear plane strain quadrilateral element with two degrees of freedom in each node. It assumes that the out-of-plane strain $\varepsilon_{ZZ} = 0$. The element can be used to model thick structures. The geometry of the element is shown in Figure 1.28.

CPS4 is an isoparametric 4-node bilinear plane stress quadrilateral with two degrees of freedom in each node. It assumes that the out-of-plane stress $\sigma_{ZZ} = 0$ and it is suitable for modeling thin structures. The geometry of the element is shown in Figure 1.28.

C3D8 is a 8-node linear brick having three degrees of freedom at each node. The elements can be used for linear analysis and nonlinear analyses involving contact, plasticity, and large deformations. The geometry of the element is shown in Figure 1.27.

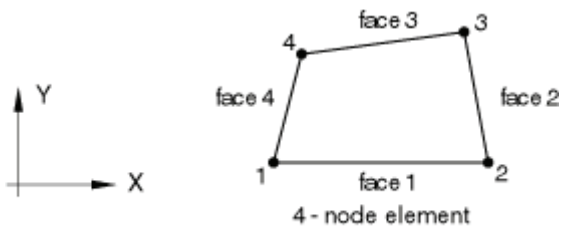

Figure 1.28 - Geometry of the elements CPE4 and CPS4 (ABAQUS 6.8).

Three-dimensional and two-dimensional finite element modes used in the simulations are shown in Figure 1.29 and Figure 1.30 respectively. Models consist of three elements - two solid elements and one cohesive element between them.

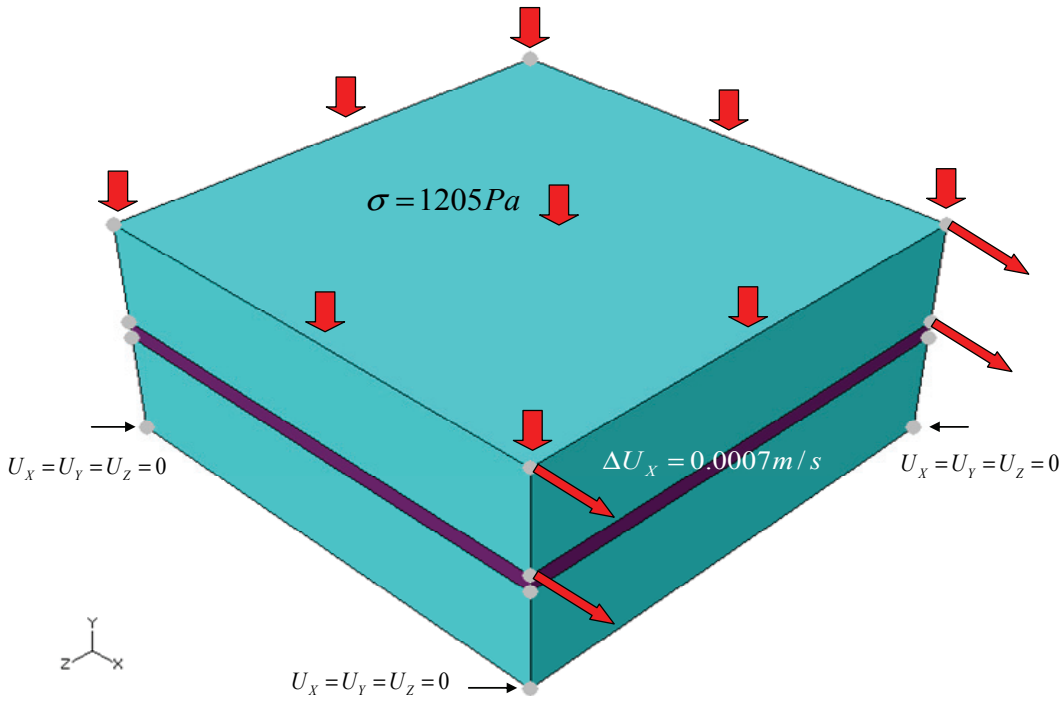

Figure 1.29 - Three-dimensional finite element model used to simulate shear test.

Ice was assumed to behave as an isotropic homogeneous elastic medium with constitutive equations given by Equation 1.13, where elasticity tensor ${}^4\boldsymbol{C}$ is written as:

$$ {}^4\boldsymbol{C} = C_{ijkl}\boldsymbol{e}_i\boldsymbol{e}_j\boldsymbol{e}_k\boldsymbol{e}_l = \frac{E}{1+\nu}\left[\frac{\nu}{1-2\nu}\delta_{ij}\delta_{kl} + \frac{1}{2}\left(\delta_{ik}\delta_{jl} + \delta_{il}\delta_{jk}\right)\right]\boldsymbol{e}_i\boldsymbol{e}_j\boldsymbol{e}_k\boldsymbol{e}_l \qquad (1.49) $$

where $\delta_{ij}, \delta_{kl}, \delta_{ik}, \delta_{jl}, \delta_{il}, \delta_{jk}$ is Kronnecker deltas. The expression (1.49) was obtained by rewriting equation for the elasticity tensor ("Linear elasticity", Wikipedia, 2009) in terms of E and ν.

A quasistatic problem of elasticity formulated in terms of displacement is given by Equation 1.6. A system of finite element equations for the static analysis due to presence of cohesive elements (nonlinear constitutive behavior, $\boldsymbol{D}^{(ce)}$ is a function of nodal displacements) and due to geometrical nonlinearities (Equation 1.15) is given by Equation 1.40. Large displacement theory was used (nlgeom=YES).

The behavior of the freeze-bond part was specified in terms of triangular traction-separation law (see Subsection 1.3.3).

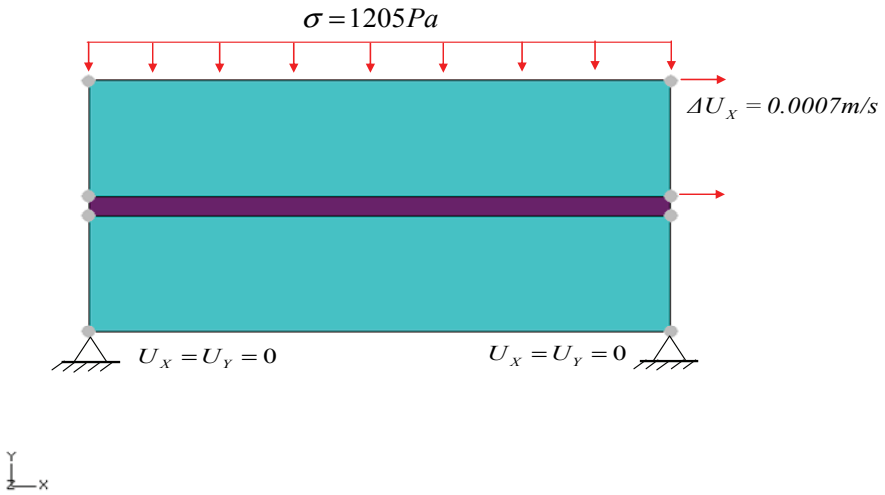

Figure 1.30 - Two-dimensional finite element model used to simulate shear test.

1.5.2.3 Boundary conditions

Boundary conditions for the model were specified as following:

→ The displacements of the bottom face of the lower ice piece were set to zero in all directions.

→ The displacements of the top face of the of the upper ice piece were allowed only in the directions of applied loads.

1.5.2.4 Loads

Loads were applied in several steps:

Within the Step 1 vertical pressure of 1205Pa (as during the experiment) was applied to the top face of the upper ice piece (Figure 1.29 and Figure 1.30).

Within the Step 2 gradually rising horizontal displacements were applied as it shown in Figure 1.29 and Figure 1.30 to simulate a constant sliding speed of 0.0007m/s.

The nonlinear system of equations (Equation 1.40) was solved with Newton implicit method (Subsection 1.3.4.2) in ABAQUS/Standard, where linear systems of equations were solved with the direct multifrontal method (Subsection 1.3.4.1).

RESULTS 2

Information presented in this chapter brings additional knowledge which can allow: (i) improvement of existed models of ice-ridges, (ii) improvement of correlation between model and full-scale experiments; (iii) improvement of numerical models of ice-ridges. Section 2.1 presents results of the interpretation of freeze-bond shear strength experiments. Section 2.2 presents results of the numerical simulations of freeze-bond shear tests.

2.1 Analysis of Freeze-bond Shear Strength Experiments

2.1.1 Freeze-bond shear strength

Repetto-Llamazares, et al. (2009b) did a preliminary analysis of the experiments and focused mainly on FB shear strength as a function of confining pressure and submersion time. The shear strength of an ice sample (R_s) was calculated as maximum force divided by contact area. A statistical distribution of FB shear strength in the experiments of Repetto-Llamazares, et al. (2009b) is shown in Figure 2.1.

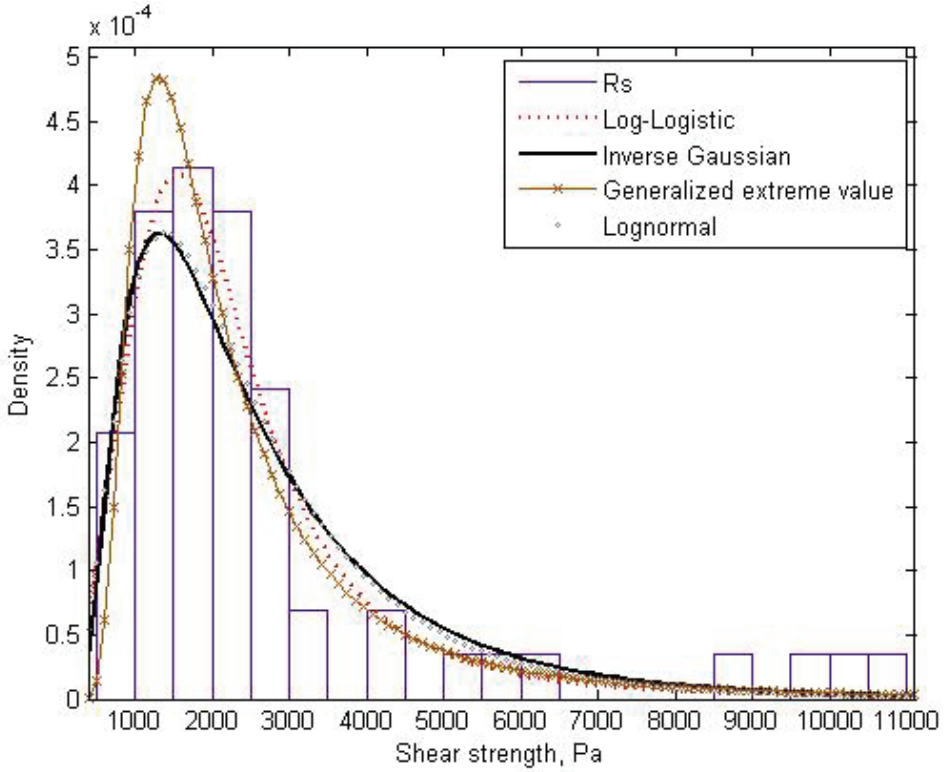

Figure 2.1 - Freeze-bond shear strength distribution.

Several distribution types were fitted to the data as illustrated in Figure 2.1. Fitting was done in MATLAB with *dfittool*, Freedman - Diaconis Rule was used to set bin widths and locations, (see MATLAB help for more details). Parameters of fitted distributions are given in Table 2.1.

Table 2.1 - Distribution parameters.

Distribution type	Mean	Variance
Log-Logistic	2446	$4.6 \cdot 10^6$
Inverse Gaussian	2670	$3.7 \cdot 10^6$
Generalized extreme value	2739	$2.6 \cdot 10^7$
Lognormal	2585	$3.4 \cdot 10^6$

As it can be seen from Figure 2.1, the R_s values were significantly scattered, it could be due to experimental uncertainties described in Repetto-Llamazares, et al. (2009b) and also due to a fact that FB shear strength is a function of time, temperature, confining pressure used to form FBs, etc. The Log-Logistic distribution seems to be the best fit to most of the experimental data.

In order to help in the interpretation of obtained trends in Repetto-Llamazares, et al. (2009b) and to gain knowledge on the ice failure process from the 58 conducted measurements several additional parameters were estimated (see Appendix B) and analyzed.

2.2.2 Failure type

2.2.2.1 Ductile or brittle

It is well known that ice exhibits either ductile or brittle behavior, depending upon the conditions under which it is loaded. In ductile fracture (ductile behavior), the crack grows slowly and is accompanied by a large amount of plastic deformation. The crack will not grow unless an increased stress is applied. On the other hand, in dealing with brittle fracture, cracks spread very rapidly with little or no plastic deformation. The cracks that propagate in a brittle behavior will continue to grow once they are initiated. It is commonly known in ice science that two behaviors can be distinguished by comparing their stress-strain curves. The ice response for ductile and brittle materials is exhibited by both qualitative and quantitative differences in their respective stress-strain curves. This gives rise to the question of which criteria may be used to distinguish between brittle and ductile fracture of ice.

A tendency of ice samples to fail either in brittle or ductile manner has been observed by Repetto-Llamazares, et al. (2009b). In this study ductile and brittle samples were separated from one another based on following criteria:

(i) Visual observations of post-peak behavior of loading history within period $t_f - 0.3s \le t_f \le t_f + 0.3s$, where t_f is the failure moment, corresponding to the peak force, see Figure 2.2;

(ii) A critical value (S_{cr}) of unloading slope (S_u). The values of S_u were calculated as $S_u=\left(\frac{dF}{dt}\right)_{t>t_f}$ (Table 2.2);

(iii) A critical value (S_{cr}') of loading slope (S_l'). The values of S_l' were calculated as $S_l'=\left(\frac{dF}{dt}\right)_{t_{sf}\le t\le t_f}$, where t_{sf} is the start time of the failure process (Figure 2.2), see Appendix B.

It is worth noting that:

→ The force measured after time t_f was always less than $F(t_f)$. Mathematically it can be written as $F(t>t_f) < F(t_f)$;

→ For most of the cases maximum registered force or peak force (F_p) corresponded to the $F(t_f)$ and therefore, it was further considered that $F_p \approx F(t_f)$;

→ No negative registers of F existed within the time span $[t_{sf}, t_f]$ or for $t_{sf} \le t \le t_f$ $F(t) \ge 0$;

→ Estimations, made by visual observations, were highly dependent on the software used for visualization, scale used in the plots and the eye of the observer.

It can be shown that the observer's skill in interpreting a model and obtaining the necessary results is an important factor.

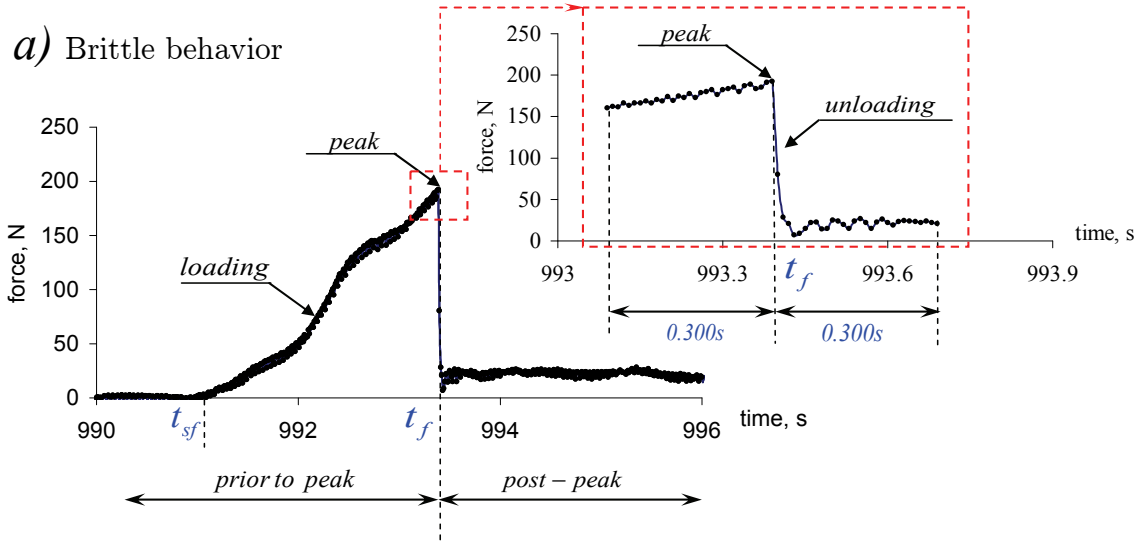

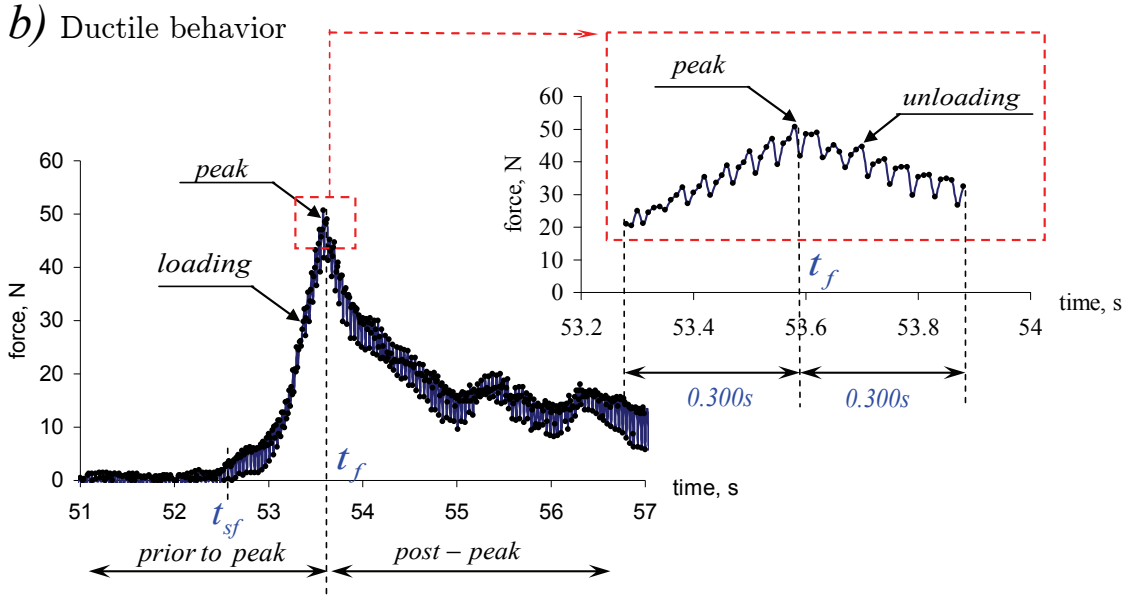

Figure 2.2 - Representative plot of curves obtained when testing freeze-bonds in direct shear device; (a) - Brittle behavior, sample 23_7_3; (b) - Ductile behavior, sample 13_7_1 (t_f - the time corresponding to the failure; t_{sf} - start time of the failure process).

Criterion (ii)

At first, brittle samples were selected from the total set of experiments based on the criterion (i), then for the selected brittle samples values of $S_u = \left(\frac{dF}{dt}\right)_{t>t_f}$ were calculated (Table 2.2a). In Table 2.2a the values of S_u for some ductile samples are also shown. This was done to give the reader an idea of representative values. As it could be seen from Table 2.2a the calculated slope value for FB_R4_3 is too low and can be compared with the slope for ductile samples. This raises questions regarding the validity of using only visual observation for a brittle/ductile judgment.

Samples with $S_u < S_{cr}$ were considered to be ductile. Assuming that $S_{cr} = 400N/s$, it was possible to find a new set of brittle samples (Table 2.2b). New set consisted of 14 samples in total, 13 samples were associated to higher forces. All 14 samples had post-peak behavior of loading history as it shown in Figure 2.2a.

In Figure 2.3 the effect of normal pressure (confining pressure σ) on the FB shear strength for ductile samples, defined by criterion (ii) is shown. Samples found in the model ridges were not considered. Each point in Figure 2.3 to Figure 2.6 was calculated as an average of the n measurements available. The shear strength increased as normal pressure increased. For the low ice temperature a linear dependency could be assumed between σ and R_s.

Table 2.2 - Unloading slope data, S_u is the unloading slope: (a) – criterion (i); (b) - criterion (ii)

Brittle fracture		Ductile fracture	
file	**S_u**	**file**	**S_u**
13_7_4	-3031	13_7_1	-187
23_7_3	-4632	10h_13_2	-62
23_7_jump	-2816	**average**	-125
7_4_2_jump	-1578	**std**	88
13_17_1	-3072		
23_17_1	-5082		
23_17_2	-2146		
1_3000gr1	-686		
1_4kg_3	-2136		
1_buoy_1	-1176		
1_buoy_2	-501		
7_10_1	-416		
7_10_3	-864		
1h_12_1	-1968		
FB_R4_3	-96		
average	-2013		
std	1502		

(a) - Data summary, criterion (i)

Brittle fracture	
file	**S_u**
13_7_4	-3031
23_7_3	-4632
23_7_jump	-2816
7_4_2_jump	-1578
13_17_1	-3072
23_17_1	-5082
23_17_2	-2146
1_3000gr1	-686
1_4kg_3	-2136
1_buoy_1	-1176
1_buoy_2	-501
7_10_1	-416
7_10_3	-864
1h_12_1	-1968
average	-2150
std	1459

(b) - Improved data set for brittle fracture, criterion (ii)

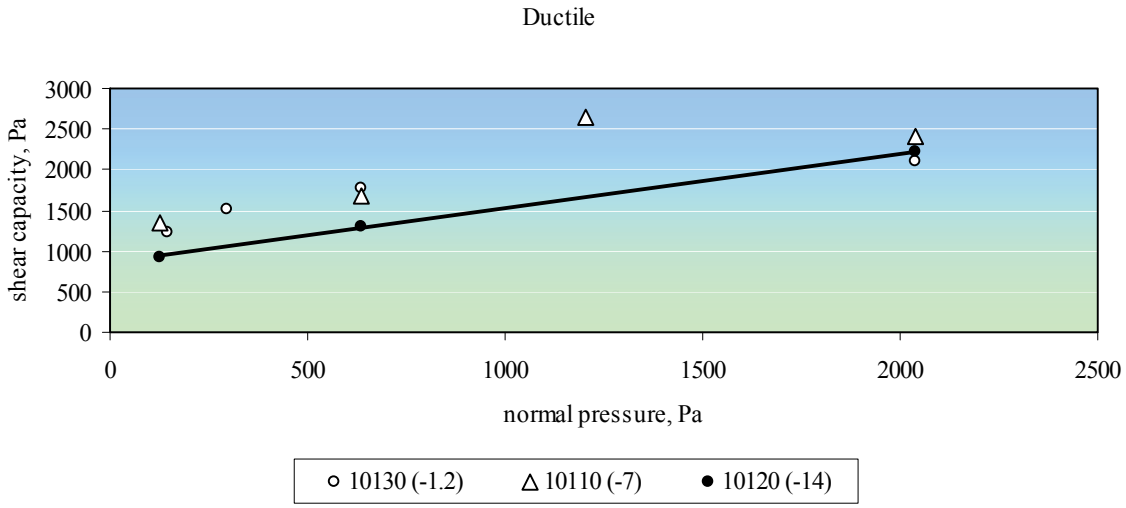

Figure 2.3 - Shear strength of freeze-bonds as a function of normal pressure (ductile samples, criteria (i) and (ii)).

The temperature dependency was complex as is more clearly shown in Figure 2.4. Initial temperature of ice samples (T_i) used in the 10110 and 10210 tests was about -7.5 °C; in 10120 T_i = -14.0 °C; in 10130 T_i = -1.2 °C; in 10220 T_i = -12.0 °C; in 10410 T_i = -1.3 °C; and in 10510 T_i = -1.7 °C (Table 1.1).

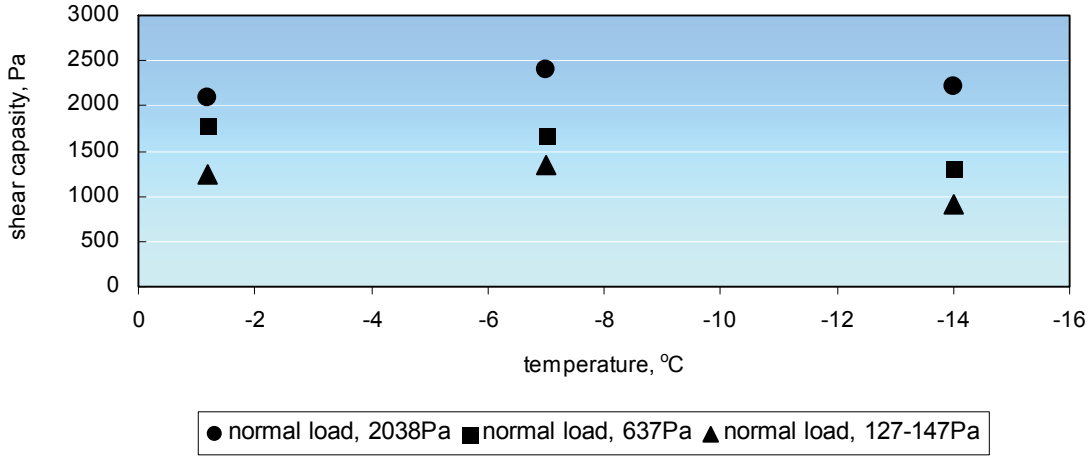

Figure 2.4 - Temperature dependence of averaged shear capacity at different normal pressures (ductile samples, criteria (i) and (ii)).

If the temperature was lower than -7°C, then shear capacity increased with rise in temperature (except for the normal pressure of 637Pa) but it decreased at temperature higher than -7°C.

The submersion time dependency is shown in Figure 2.5 for ductile fracture. There was a decreasing tendency of the freeze-bond strength versus increasing submersion time. Temperature dependency was complex and will be discussed later.

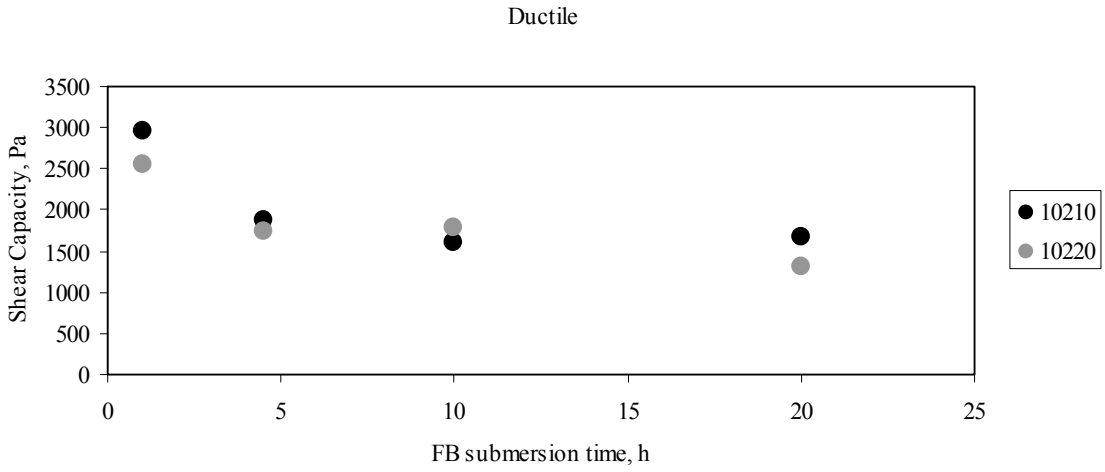

Figure 2.5 - Averaged shear capacity as a function of the submersion time. Ductile samples, criteria (i) and (ii).

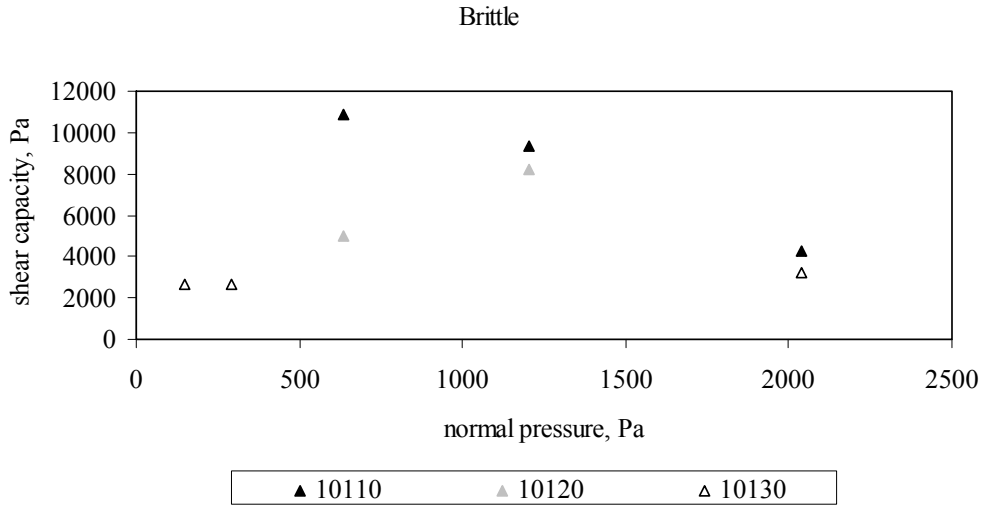

Figure 2.6 - Averaged shear capacity for brittle fractures (criteria (i) and (ii)) as a function of normal pressure.

Criterion (iii)

Averaged (approximated) loading slope (S_l') was calculated as:

$$S_l' = \frac{F(t_f) - F(t_{sf})}{(t_f - t_{sf})}, [N/s] \tag{2.1}$$

where t_f is the failure time; t_{sf} is the start time of the failure process; F is the force registered during experiments.

Approximated loading slope varied in each sample. Distribution of S_l' is shown in Figure 2.7.

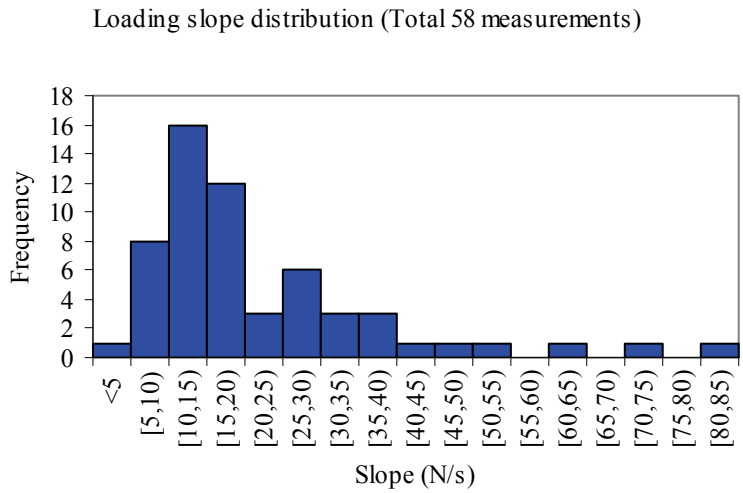

Figure 2.7 - Distribution of approximated loading slope.

Two characteristic peaks can be seen from the distribution. The first peak corresponds to the loading slopes ranged between 10-15N/s and the second peak corresponds to the slopes ranged between 25-30N/s.

In order to distinguish between brittle and ductile samples, a critical loading slope was introduced (S_{cr}'). Samples with $S_l' < S_{cr}'$ were assumed to be ductile. A value of $S_{cr}' = 39$N/s was chosen on the basis that the most of the brittle samples obtained by use of the criteria (i) and (ii) had the S_l' values higher than 39N/s. Seven brittle samples were found from all measurements. Five out of seven samples were brittle by visual observation (criterion (i)). A summary for ductile samples (loading slope is less than 39N/s) is shown in Figure 2.8. Each point in Figure 2.8 was calculated as an average of the n measurements available. Samples found in the model ridges were not considered here.

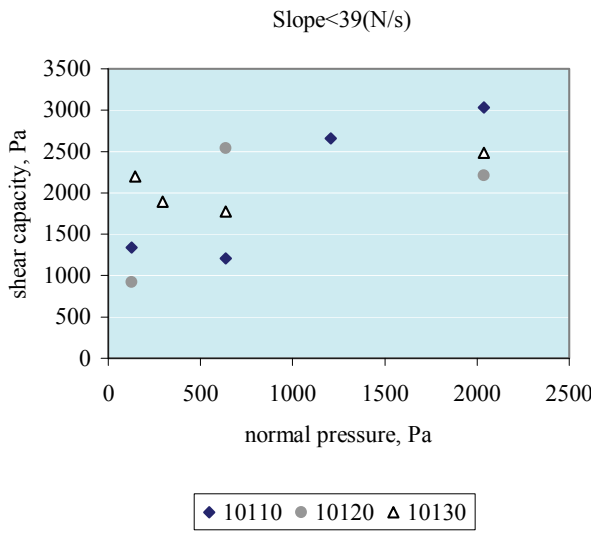

(a)- Shear capacity for ductile fractures (criterion (iii)) as function of the normal pressure.

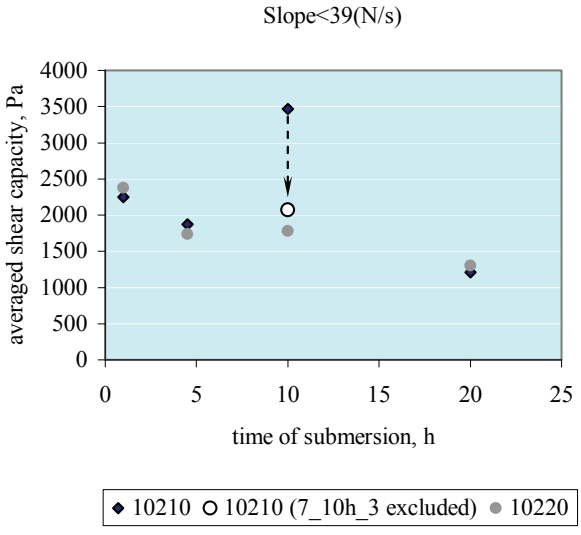

(b)- Shear capacity for ductile fractures (criterion (iii)) as function of the submersion time.

Figure 2.8 - Summary of the obtained results for the ductile samples with loading slope less then 39N/m.

Similar trends as in Figure 2.3 and Figure 2.5 can be seen in Figure 2.8. However using the loading slope (criterion (iii)) as the criteria to separate brittle from ductile samples is probably not the best approach. The dependencies shown in Figure 2.8a are more complex than given in Figure 2.3, which is probably an artifact introduced by excluding samples with loading slope >39N/s.

The tilted and re-tested samples mentioned in Repetto-Llamazares, et al. (2009b) could significant affect the results as shown in Figure 2.8b. Assume the following: in the test 10210 all measurements were valid, contact surfaces were parallel to each other during the test and no tilting was reported. Let's exclude brittle samples from

analysis based on the averaged loading slope value (e.g. criterion (iii)), saying that all samples with slope >39N/s could be considered as brittle ones. Calculated shear capacity of the freeze-bonds as a function of the submersion time is shown in Figure 2.8b (black rhombuses).

Now assume that during the tests 10210 with submersion time of ten hours one measurement was not valid due to tilting of the sample during experiment. Removing one measurement from the analysis we obtained a new point (Figure 2.8b, white circle). Thus the lack of both statistical data and the presence of tilted and retested samples might lead to misinterpretation of the temperature dependencies as well as general trends. Most probably the general trends reported in Repetto-Llamazares, et al. (2009b) were found correctly.

2.2.2.2 Summary

The percentage of brittle and ductile samples obtained by using of different criteria is given in Table 2.3.

Table 2.3 - Change in the percentage of brittle and ductile samples

Criterion	Brittle, %	Ductile, %
(i)	26	74
(ii)	24	76
(iii)	12	88

Further in this study only the value of post-failure slope and visual observation of the post-failure behavior (criterion (ii) + criterion (i)) will be used to differentiate between ductile and brittle samples.

2.2.3 F(t) behavior (as visual observation)

As the force was measured as a function of time t, all results could be grouped based on following types of $F(t)$ behavior: smooth or 'line' and saw-toothed behavior ('saw (1)', 'saw (2)', 'saw (3)' and 'mix'). Examples for the 'saw (1)', 'saw (2)', 'saw (3)', 'line' and 'mix' type of failure are given below (Figure 2.9). Measured force plotted versus time within time space of $t_f - 0.3s \le t_f \le t_f + 0.3s$ is shown in Figure 2.9.

Different types of saw-toothed failure behavior leads to the different failure loads $F(t_f)$ as it can be seen from Figure 2.10 but no particular load levels could be associated with the 'saw (1)', 'saw (2)', 'saw (3)', 'line' and 'mix' types of failure. In Figure 2.10 measured force plotted versus time within time space of $t_f - 0.3s \le t_f \le t_f + 0.3s$.

The values of the FB shear capacity did not seem to be correlated with the curve types in Figure 2.9.

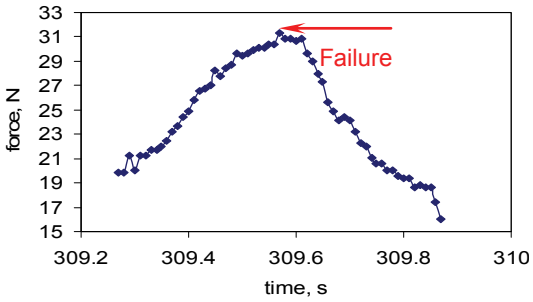

'line' (file 7_10h_2)

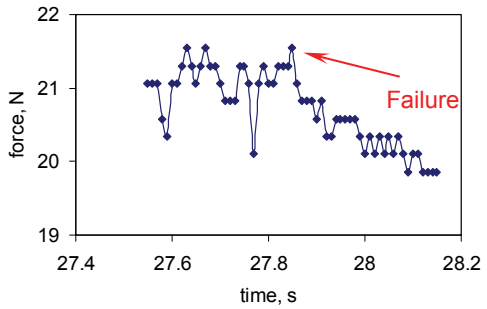

'mix' (file FB_R4_1)

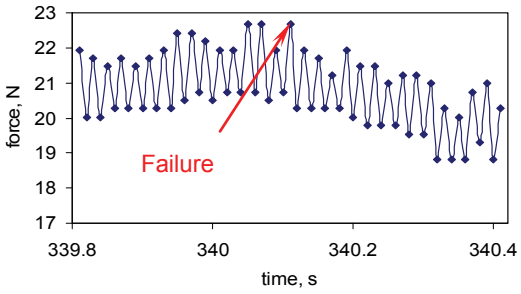

'saw (1)' (file FB_R3_4)

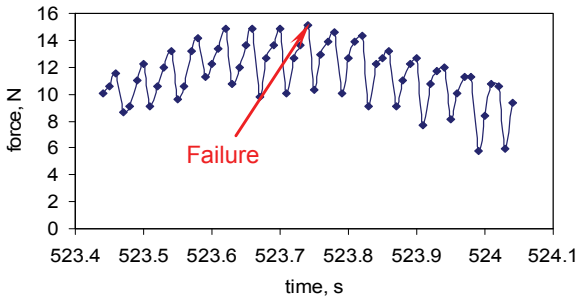

'saw (3)' (file Buoy_4)

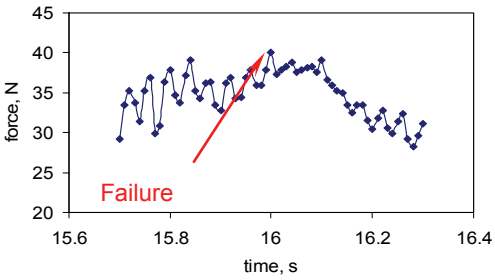

'saw(2)' (file Buoy_1)

Figure 2.9 - Typical types of *F(t)* behavior (from all results).

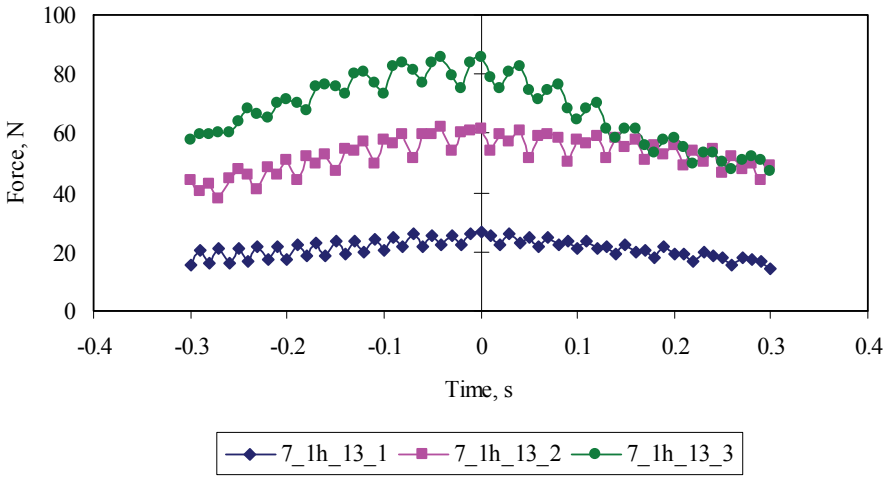

Figure 2.10 - Measured force versus time $t(t_f \pm 0.3s)$: the lower curve corresponds to the 'saw (1)' type, both middle and upper curves are 'saw (3)' type.

Measured response types in the figures above include: (i) signal noise; (ii) material response; (iii) response of measuring device. Types of curves in Figure 2.9 were probably related to the ice structure but it is hard to tell how they were related.

2.2.4 Post-peak force

Post-peak force *F1* was estimated as:

$$\begin{aligned} &F1=F(t_f+1.0s) \text{ for ductile fracture, [N]} \\ &F1=F(t_f+delta+1.0s) \text{ for brittle fracture, [N]} \end{aligned} \tag{2.2}$$

where *delta* (in seconds) is the time needed for the load to drop down. It was introduced to exclude very steep slopes from the future *F(t)* plots. And it could be shown that $F(t_f + 1) \approx F(t_f + delta + 1)$.

The curves *F(t)* (after the failure had occurred) were smoothed by the moving average of every four points in *Excel* (Appendix C). Figure 2.11 illustrates representative curves for the samples series 10140 in order to give the reader an idea regarding post-failure behavior. In the figures in Appendix C the brittle samples can be recognized from ductile samples based on the post-failure behavior. Post-failure behavior of brittle samples started with a lower force value and then slowly rose with time.

From the measurements of force versus time it could be seen that the post-failure behavior was a saw-toothed, with different saw-tooth amplitude, and measured force *F1* converged to the 8N-30N value. For samples from the ice-ridge (Test 10410 and Test 10510) the force after failure converged to value in range 13N-23N which was slightly lower than series 10100 and 10200, which could be explained by lower value of normal pressure, used during series 10410 and 10510. Figure 2.12 summarizes the results of series 10100 and 10200. Each point was calculated as an average of the *n* available measurements without distinguishing between brittle and ductile samples.

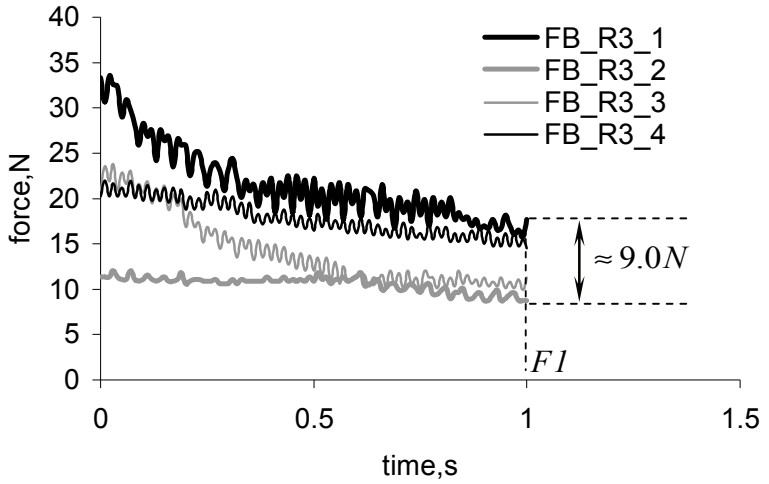

Figure 2.11 - Post-failure behavior of ice samples from series 10140 (Samples taken from the rafted layers of ice found in the model ridges).

Figure 2.12b shows a decreasing tendency of *F1* when the submersion time increases up to 10hours. *F1* increased with increasing of normal load.

From Figure 2.11 it can be seen that *F1* convergences to approximately the same value. This value depended on the normal pressure, the initial ice temperature and the submersion time (Figure 2.12). For the tests with the same confining pressure, submersion time and initial ice temperature *F1* did not vary much even if the samples showed brittle or ductile behavior.

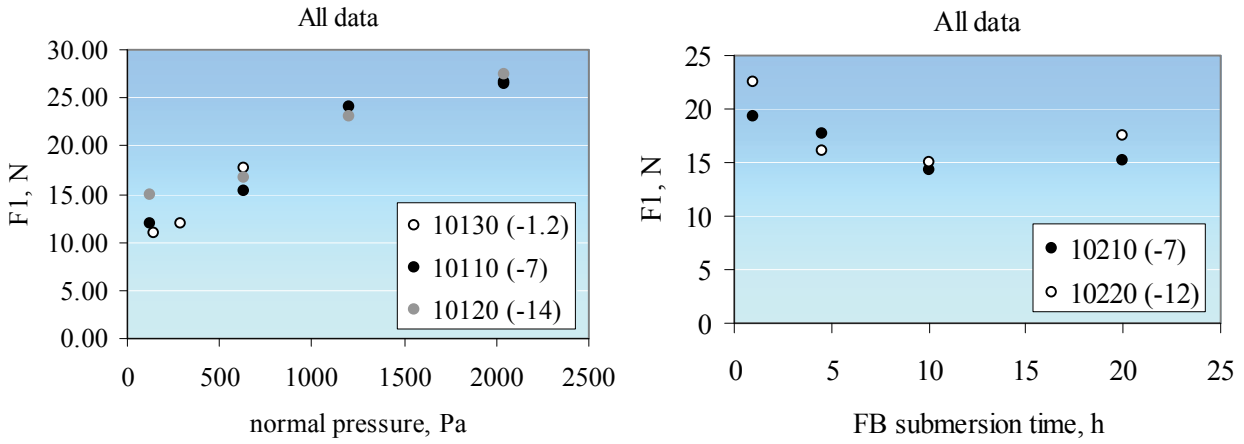

(a) (b)

Figure 2.12 - A summary of the obtained results of series 10100 and 10200: (a) - A force *F1* versus normal pressure; (b) - A force *F1* as a function of the submersion time.

It was assumed that *F1* is correlated to the frictional force (F_f) during the sliding of the de-bonded ice samples. If F_f is the frictional force and F_n is the normal force, then by definition the friction coefficient is:

$$\mu = \frac{F_f}{F_n} \tag{2.3}$$

In this study it was not possible to say either if the tested samples were tilted or if the samples started sliding relative to each other at the time when *F(t)=F1*. Hence, only a similitude (an approximation) of friction coefficient (μ^*) could be obtained by selecting the value of force *F1* and dividing it by the normal force applied on the ice sliding interface.

Figure 2.13a gives the ice-ice friction coefficient similitude plotted against temperature in a range -1.2°C to -14°C at different normal pressures for ductile samples (submersion time of 20hours).

There was almost no temperature dependence of friction coefficient similitude at normal pressures of 637Pa and 2038Pa. At temperatures lower than -7°C, μ^* slightly decreased with rising temperature form -7 °C to -1.2 °C at normal pressure of 632Pa.

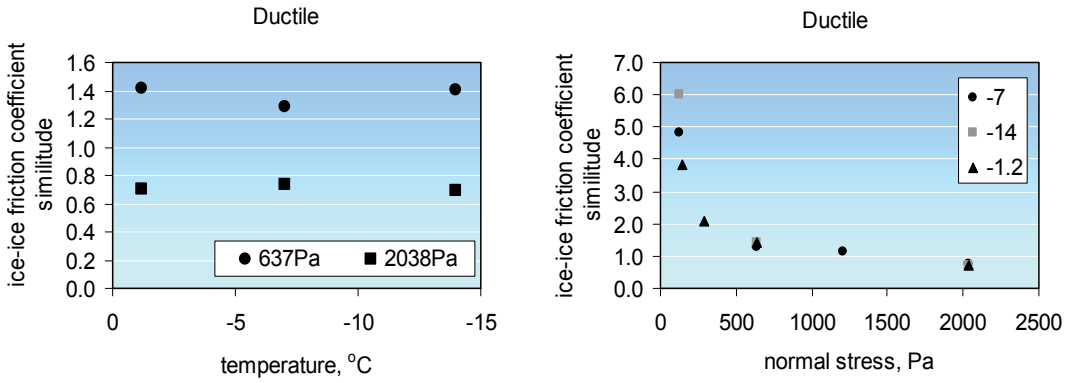

(a) (b)

Figure 2.13 - (a) - Temperature dependence of ice-ice friction coefficient similitude at different normal pressure (ductile samples, submersion time is 20hours, sliding velocity is 0.0007m/s.); (b) - Normal pressure dependence of ice-ice friction coefficient similitude at different temperatures(ductile samples, submersion time is 20hours sliding velocity is 0.0007m/s).

Normal stress dependence of μ^* at temperatures -14, -7 and -1.2 °C is shown in Figure 2.13b. μ^* decreased when normal stress increased.

The values of ice-ice friction coefficient similitude (μ^*) slightly higher than one (Figure 2.13) can be explained with the following example:

Example 1

Figure 2.14 shows development of μ^* in time, starting just after the failure.

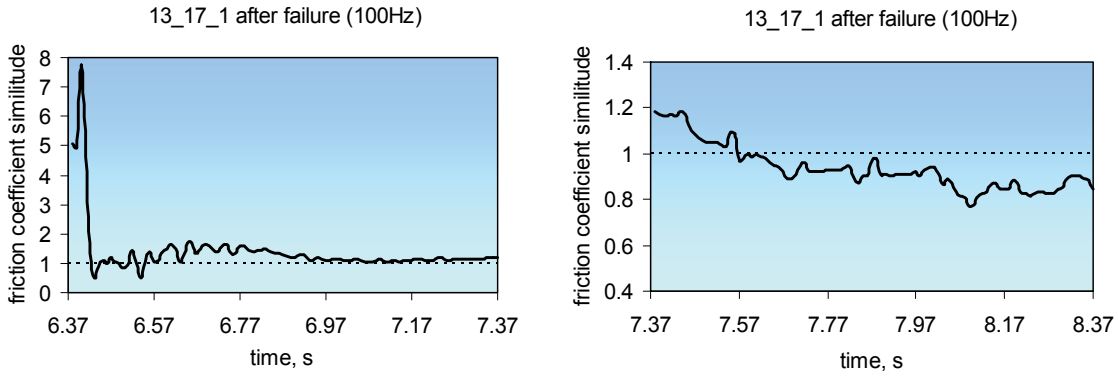

Figure 2.14 - Ice-ice friction coefficient similitude as a function of time (sample 13_17_1).

To calculate μ^* evolution in time measured force was divided (point by point) by the applied normal force value. Figure 2.14 (left) shows μ^* evolution within the first

second after the failure, while in Figure 2.14 (right), the evolution of μ^* within the next second is illustrated.

Figure 2.14 shows that at the end of first second the μ^* value was above one, which implies that the force required to slide an ice block along the surface of another ice block was greater than the normal force of the surface on the ice sample. Within the next second μ^* reached a value which was lower than one.

Extremely high values of μ^* in Figure 2.13b can be explained with the following example:

Example 2

The assumption of $F1 = F_f$ in Equation 2.3 was wrong and $F1 \neq F_f$. From Figure 2.12a it can be seen that for the considered sliding system (ice-ice) the frictional force $F1$ is related (not proportional) to the normal load (P) as:

$$F1 = \mu_0^* F_n + z, \tag{2.4}$$

where μ_0^* and z are the constants, which can be treated as a coefficient of Coulomb friction and cohesion, respectively.

Such behavior was probably a combination of following phenomena:

→ Not only friction mechanisms were involved. At the end of one second since the load peak was reached freeze-bond has softened but it was still in the plastic state.
→ Model ice was different from the real ice;
→ The roughness of contacting ice surfaces was significant immediately after the failure and changed as ice slides;
→ A transition between static and kinetic friction;
→ An effect of the ice sintering due to low sliding velocity.

In reality, due to sliding of ice samples relative to each other, the contact area will decrease with time. Such effect wasn't taken into account due to mainly two reasons: the exact position of ice blocks relative to each other was unknown during experiments and sliding velocity was low. Figure 2.15 shows an example at -14 °C temperature. Analogous to the study in Maeno, et al. (2003), from the definition of the friction coefficient (Equation 2.3), and dividing the expression above (Equation 2.4) by the F_n we got:

$$\mu^* = \mu_0^* + \frac{z}{F_n} \tag{2.5}$$

According to this relation (Equation 2.5) the friction coefficient similitude approaches μ_0^* at larger normal stress and increases rapidly with decreasing normal stress at smaller normal stress. This was in good observations of μ^* in Figure 2.13b.

For high normal stresses the value of $\mu^* = 0.7$ was found.

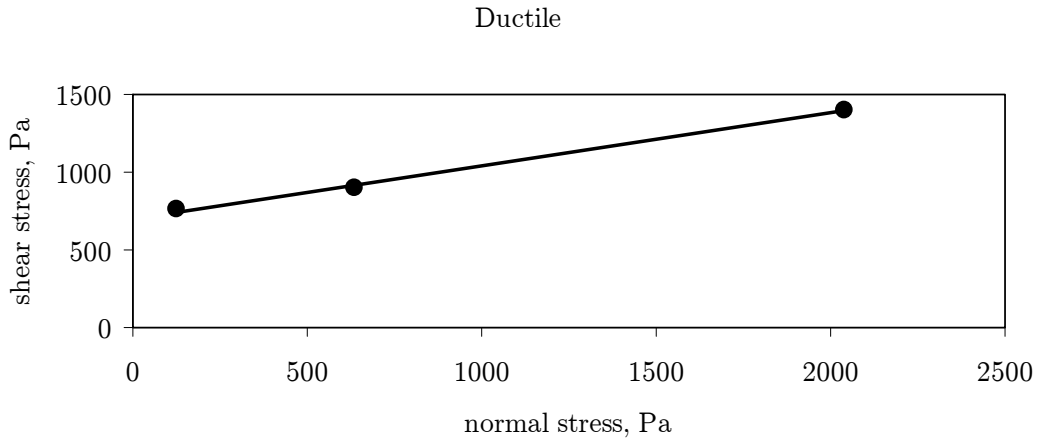

Figure 2.15 - Linear relation between the post-peak shear stress and the normal stress at -14°C temperature.

By linear fitting of the data points as shown in Figure 2.15, the Coulomb friction coefficient and cohesion were estimated at each temperature (Figure 2.16a and Figure 2.16b respectively). The shear stress in Figure 2.15 was obtained by dividing *F1* by the surface area of the ice blocks.

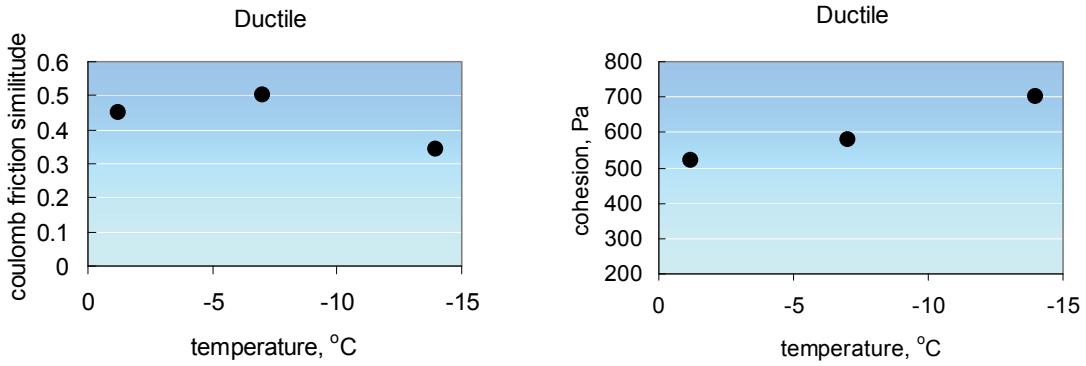

(a) (b)

Figure 2.16 - Estimated Coulomb friction coefficient plotted against temperature (a), cohesion plotted against temperature (b).

The adhesion (cohesion in Figure 2.6b divided by the Coulomb friction coefficient in Figure 2.6a) ranged from 1.2 to 2.1kPa, which are one to two orders of magnitude

smaller than the flexural strength of model ice (Table 1.2) and one to two order of magnitude higher than adhesion reported in Maeno, et al. (2003).

The relation between normal pressure (σ) and freeze-bond shear capacity (R_s) at temperatures of -14°C, -7 °C and -1.2 °C showed that it can be reasonably expressed by a linear function.

$$R_s = a\sigma + b, \tag{2.5a}$$

where a and b are constants. As it can be seen that the empirical relation is similar to the so-called Mohr-Coulomb failure criterion, a can be regarded as the internal friction coefficient and b as the cohesion strength.

By linear fitting of data points in *Excel*, internal friction coefficient a=0.67 was estimated at temperature -14°C (Figure 2.3). After the first second since failure occurred, the normal stress dependence of frictional stress at -14°C could be expressed by a linear relation (Figure 2.15). By linear fitting of data points internal friction coefficient was found as a=0.34.

Figure 2.17 shows estimated values of internal friction coefficient (a) and cohesion (b), obtained by linear fitting of data points, as a function of temperature (white squares represents values corresponding to the peak force (ductile failure), black circles show values corresponding to *F1* force (ductile failure)).

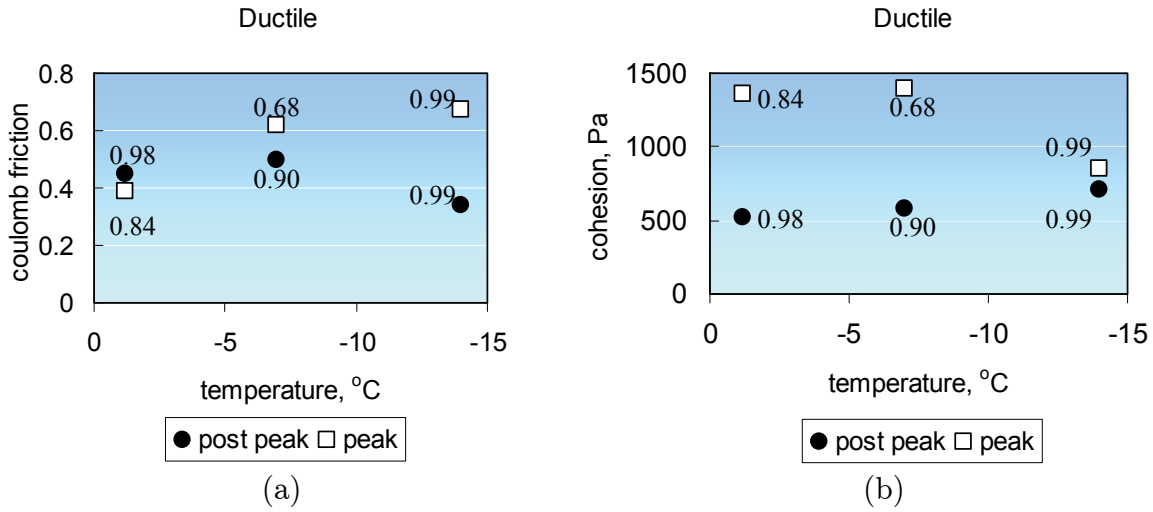

Figure 2.17 - Internal friction coefficient (a) and cohesion (b) as a function of temperature for ductile ice behavior

In Figure 2.17 correlation coefficient squared (r^2) was calculated as:

$$r^2 = \left[\frac{n\sum(\sigma R_S) - \sum\sigma \sum R_S}{\sqrt{\left[n\sum\left(\sigma^2\right) - (\sum\sigma)^2\right]\left[n\sum\left(R_S{}^2\right) - (\sum R_S)^2\right]}} \right]^2 \qquad (2.5b)$$

where n is the number of data points used for the linear fitting. r^2 is a measure of the reliability of the linear relationship between normal (σ) and shear stress (R_S) values. Predictions of coulomb friction based on the linear relationship $R_S = a\sigma + b$ are less reliable if the value of r^2 far away from one.

Let us redraw Figures 2.17a and 2.17b by combining the coulomb friction data and the cohesion data and plotting them on axes of shear stress and normal stress using Equation 2.5a. Obtained in such a way plots better illustrates behavior of both cold ice (Figure 2.18a) and warm ice (Figure 2.18b). In Figure 2.18 the dashed line (called *peak*) denotes shear behavior of FB at the time t_f and the solid line (called *post-peak*) denotes shear behavior of FB at $t_f + 1.0$s.

As it can be seen from Figure 2.17a, as temperature decreases the difference between internal friction coefficients at failure and at one second after the failure increases. An opposite trend was found for the cohesion (Figure 2.17b). The value of internal friction at failure was higher than after the failure for low temperatures. The cohesion strength at failure was always higher than the cohesion after the failure for the considered temperatures.

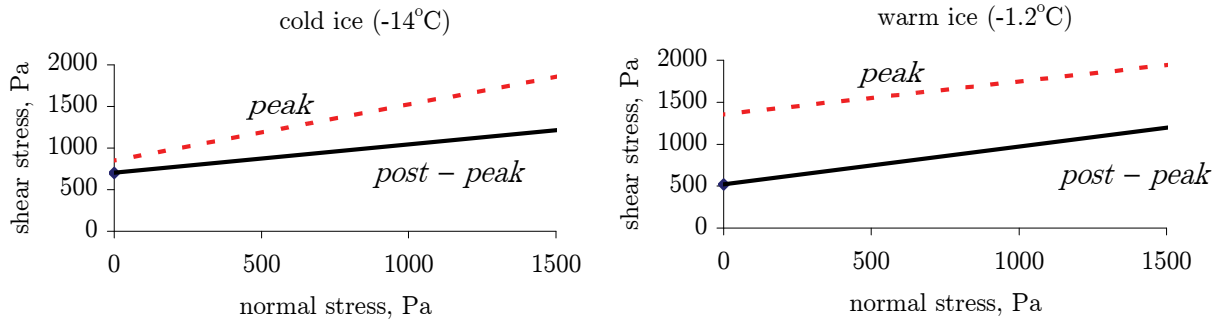

(a) (b)

Figure 2.18 - Shear stress versus normal pressure: (a) - cold ice with the initial temperature of -14°C and (b) - warm ice with the initial temperature of -1.2°C.

Figure 2.18 shows that resistance to sliding of FB depends on: (i) pressure acting normal to the surface of sliding, (ii) initial temperature of ice used to establish FB and (iii) on time. The closer FB to its melting point (soft FB) the higher is its non-frictional resistance (corresponding to the peak force). From Figure 2.18 can be seen that the angle of internal friction, corresponding to the post-peak force, is less sensitive to the change of ice temperature than those corresponding to the peak force. Therefore, though physical mechanisms governing FB behavior at failure and after it

are connected implicitly, FB behavior prior to and after its failure should be considered separately.

2.2.5 Fracture energy

The macroscopic potential energy of the system, consisting of the internal stored elastic energy and the external potential energy of the applied loads, varies with the size of the crack (Yue, 2009). Therefore the fracture process is associated with the consumption of energy. The energy relation can be expressed by:

$$U = U_0 - U_a - U_\gamma \tag{2.6}$$

where U is the total potential energy of the system; U_0 is the elastic energy of the uncracked plate; U_a is the decrease in the elastic energy caused by introducing the crack in the plate and U_γ is the increase in the elastic-surface energy caused by the formation of the crack surfaces.

The FB experiments were conducted at constant velocity (v) of 0.7mm/s. The displacement measuring device was placed in the piston of the pulling system. The area under the loading curve can be calculated as:

$$A = \int_{t_{sf}}^{t_f} F(t)dt \text{ , [N·s]} \tag{2.7}$$

where t_{sf} is the start time of the deformation process; t_f is the failure time.

U or total work done by the pulling system for the unidirectional movement can be written as:

$$U = \int_{x_{sf}}^{x_f} F(x)dx \text{ , [J]} \tag{2.8}$$

where x is the direction of movement, x_{sf} is the position of the piston at time t_{sf} and x_f is the position of the piston at time t_f.

If $v = \frac{dx}{dt}$ is constant, then $dx = v \cdot dt$ and U can be written as:

$$U = v\int_{t_{sf}}^{t_f} F(t)dt = v \cdot A \text{ , [J]} \tag{2.9a}$$

Therefore the area (A) under the loading curve $F(t)$ estimated as shown in Equation 2.9a is related to the total input energy to the system (U) by a proportionality constant given by v.

Lets denote A_{fb} the FB contact area, h_{fb} the FB thickness; γ_{fb} the FB shear strain (the relative in-plane displacement (u) of two parallel layers in a FB (the top and the

bottom of FB) divided by their separation distance (h_{fb})) and τ_{fb} the FB shear stress. Assuming $F(t) = \tau_{fb}(t)A_{fb}$ and $u = \gamma_{fb}h_{fb}$, Equation 2.9a can be rewritten as:

$$\begin{aligned} U &= v\int_{t_{sf}}^{t_f} F(t)dt = \int_{t_{sf}}^{t_f} F(t)\cdot v dt = \int_0^{u(\,failure\,)} F(u)du = \\ &= \int_0^{\gamma_{fb}(\,failure\,)} \tau_{fb}(\gamma_{fb})\cdot A_{fb}\cdot h_{fb}d\gamma_{fb} = A_{fb}h_{fb}\int_0^{\gamma_{fb}(\,failure\,)} \tau_{fb}(\gamma_{fb})d\gamma_{fb} = \\ &= V\int_0^{\gamma_{fb}(\,failure\,)} \tau_{fb}(\gamma_{fb})d\gamma_{fb} \end{aligned} \qquad (2.9b)$$

where V is the FB volume. It was also assumed that the displacements of the pulling piston (total displacements) equal to the displacements of FB. FB shear stress is a unique function of FB shear strain, $\tau_{fb}(\gamma_{fb}\ failure) = R_s$.

Figure 2.19a shows the evolution in time of the total energy of the system before failure of the FB in brittle sample 13_17_1. Total energy of the system at time $(t=\zeta)$ was calculated as:

$$U(\zeta) = \sum_{j=0}^{j=\zeta} Uj = \sum_{j=0}^{j=\zeta} \frac{(F(t_{j+1}) + F(t_j))}{2}\cdot(t_{j+1} - t_j)\cdot 0.0007, [J] \quad j=0,1,2,... \qquad (2.9c)$$

Figure 2.19b illustrates evolution of energy increment $\Delta U(t_i)$ in time before failure of FB in brittle sample 13_17_1. $\Delta U(t_i)$ was calculated as:

$$\Delta U(t_i) = \frac{(F(t_{i+1}) + F(t_i))}{2}\cdot(t_{i+1} - t_i)\cdot 0.0007, [J] \quad i=0,\ 1,\ 2,... \qquad (2.9d)$$

A part of U in Figure 2.19 was consumed by the pulling system, the other part of the energy was transferred to the ice sample and absorbed through the various damage mechanisms (deformation of ice, crack initiation, crack propagation, etc.).

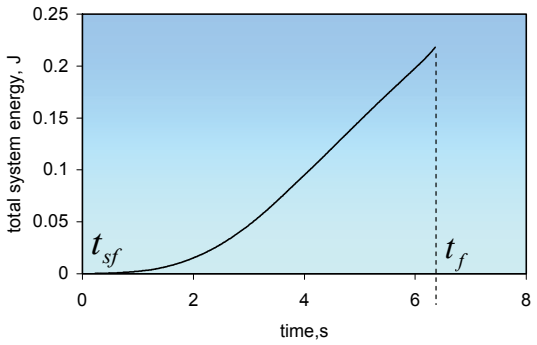

(a) - Total system energy versus time.

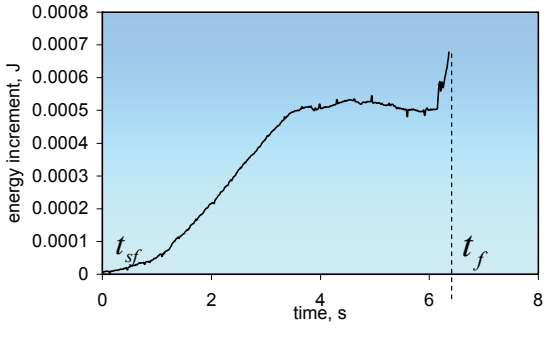

(b) - Energy increment versus time.

Figure 2.19 - Energy evolution with time for ductile sample 13_17_1.

Both elastic (continuously rising) and yielding (almost flat) regions can be seen from Figure 2.19b. Some perturbations in the energy increment can also be seen within the yielding part of the curve, which probably can be explained by processes of microcracks initiation. The flat region of the curve is followed by a sharp rising part, which might be ascribed to the formation of crack resulting in failure.

Total input of energy as a function of the normal pressure (for ductile samples) is shown in Figure 2.20a. Total input of energy as a function of submersion time is shown on in Figure 2.20b. The A value was calculated by simple trapezoidal rule in *Excel*. Each point in Figure 2.20 was calculated as an average of the n available measurements. Samples found in the model ridges were not considered here.

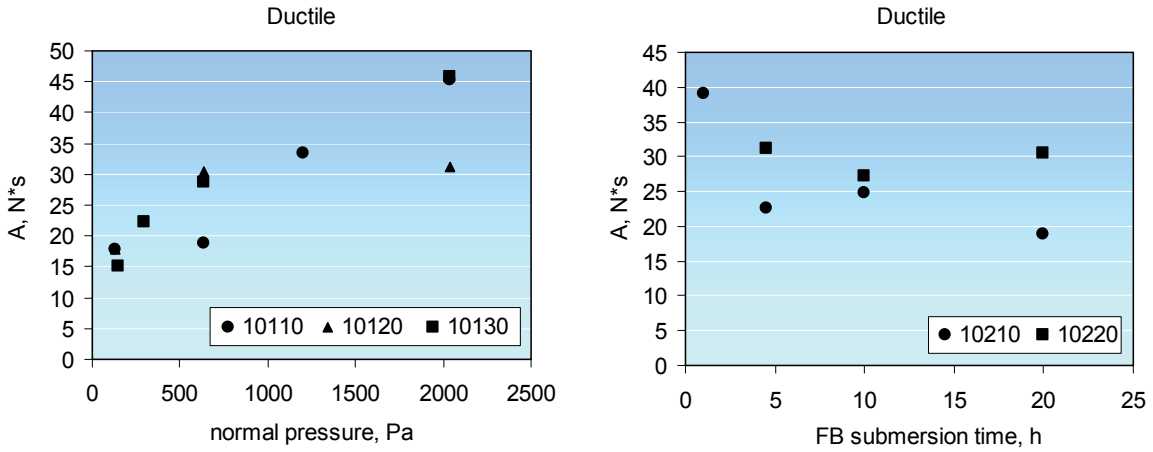

(a) (b)

Figure 2.20 - Summary obtained for the ductile samples. Area under the curve *F(t)* prior failure: (a) - Total input of energy as function of the normal pressure; (b) - Total input of energy as function of the submersion time.

The temperature effect was complex. There was an increasing tendency with increase in normal load (Figure 2.20a). Slightly decreasing tendency with increase of submersion time can be seen from Figure 2.20b.

Estimated in this way FB shear strength (R_s), post-peak frictional force (*F1*) and area under the loading curve (A) characterize the behavior of adfrozen samples of the model ice. In order to view all the possible pair-wise relationships between R_s, *F1* and A a grouped plot matrix of these parameters was created (Figure 2.21). In Figure 2.21 the histograms of considered parameters were placed along the main diagonal. It can be seen that an increase of R_s resulted in an increase of A both for brittle and ductile samples and samples found in the model ridges. Higher values of A and R_s corresponded to the brittle samples, while almost no difference was found between values of *F1* in ductile and brittle samples (see Table 2.4). Table 2.4 summaries obtained results for all 58 measurements. Average and standard deviation for A, R_s and *F1* are given for the brittle and ductile samples. Brittle samples were separated from the ductile samples based on the criteria (i) and (ii).

Table 2.4 - Estimated parameters. Area under the loading curve, ($\langle A \rangle \pm$ standard deviation), freeze-bond shear strength ($\langle R_s \rangle \pm$ standard deviation) and a force at one second after failure ($\langle F1 \rangle \pm$ standard deviation).

Ductile ice	Brittle ice
$A(duct) = 28.8 \pm 13.8 \ N \cdot s$	$A(brit) = 203.4 \pm 165.4 \ N \cdot s$
$R_s(duct) = 1861 \pm 712 Pa$	$R_s(brit) = 5548 \pm 3228 Pa$
$F1(duct) = 17.7 \pm 6.2 N$	$F1(brit) = 17.4 \pm 5.0 N$

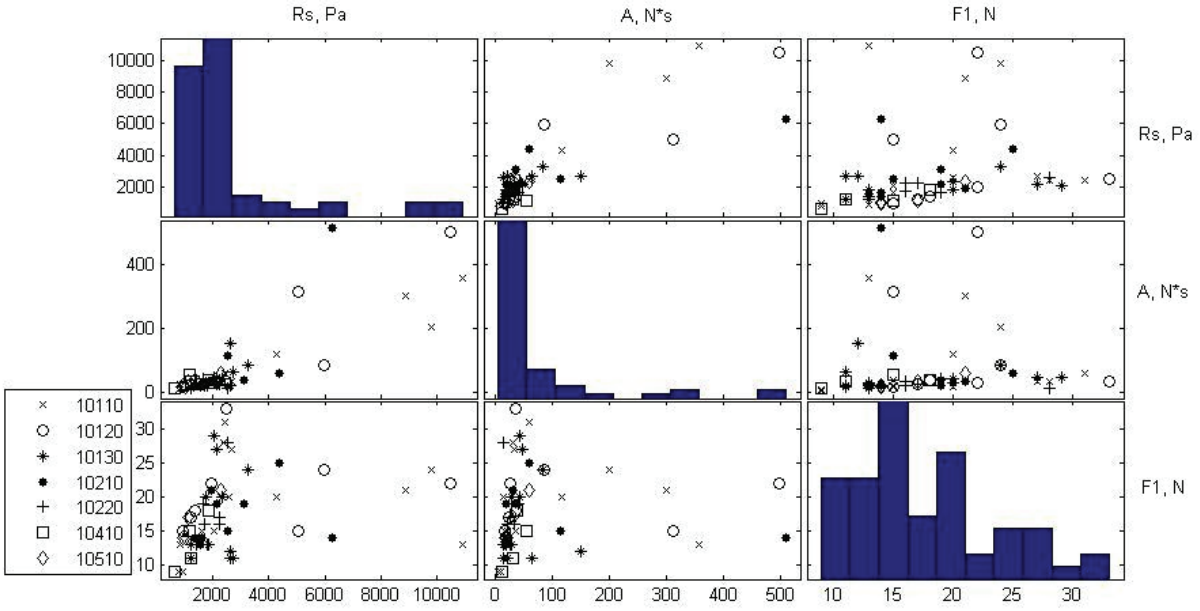

Figure 2.21 - Grouped plot matrix of FB shear strength (R_s), force at one second after failure ($F1$) and area under the loading curve (A).

Temperature dependencies were complex and will be discussed later.

As the U is a linear function of A (Equation 2.9a), there is also a relation between U and R_s (Equation 2.19b). A bivariate joint frequency distribution of U and R_s for the complete data set, consisting of 58 measurements, is presented as two-way frequency table in Figure 2.22 while a bivariate joint frequency distribution of U and R_s for ductile samples is presented in Figure 2.23. The bodies of the two-ways tables represent the joint frequencies. The differences between the values of the joint frequencies appear as the intensity of color to indicate whether the value of joint frequency is high or low (The higher the value of joint frequency the darker is the color). As it can be seen from Figure 2.22, 70% of the tested ice samples had total input of energy to the system ranged from 4 to 39mJ and shear strength ranged from 0.6 to 2.7kPa. Within the set of ductile samples (Figure 2.23) most of the samples having higher value of R_s also had higher value of U.

For series 10100 and 10200 a trend can be seen between the area (A) under the loading curve and a force ($F1$), see Figure 2.21. Figure 2.24 illustrates the relation between the A and $F1$ for the ductile samples (criteria (i) and (ii)). Each point in Figure 2.24 was calculated as an average of the n available measurements.

For both series 10100 and 10200 the area under the loading curve increased when the force $F1$ increased. For series 10100 and 10200 the correlation coefficient between the data sets (series 10100 - 23 ductile samples; series 10200 - 12 ductile samples) of A and $F1$ was equal to 0.8.

$R_s(Pa)$ →

$U(J)$ ↓

$U(J)$ \ $R_s(Pa)$	640 - 1666	1666 - 2692	2692 - 3718	3718 - 4744	4744 - 5770	5770 - 6796	6796 - 7822	7822 - 8848	8848 - 9874	9874 - 10900	10900 - 11926
0.004 - 0.039	20	21	1	0	0	0	0	0	0	0	0
0.039 - 0.074	1	2	2	1	0	1	0	0	0	0	0
0.074 - 0.109	0	2	0	1	0	0	0	0	0	0	0
0.109 - 0.144	0	0	0	0	0	0	0	0	1	0	0
0.144 - 0.179	0	0	0	0	0	0	0	0	0	0	0
0.179 - 0.214	0	0	0	0	0	0	0	0	1	0	0
0.214 - 0.249	0	0	0	0	1	0	0	0	0	0	0
0.249 - 0.284	0	0	0	0	0	0	0	0	0	0	1
0.284 - 0.319	0	0	0	0	0	0	0	0	0	0	0
0.319 - 0.354	0	0	0	0	0	0	0	0	0	1	0
0.354 - 0.389	0	0	0	0	0	1	0	0	0	0	0
										Total	58

Figure 2.22 - A bivariate joint frequency distribution of total input of energy to the system (U) and freeze-bond shear strength (R_s) for the complete data set consisting of 58 measurements.

$R_s(Pa)$ →

$U(J)$ ↓

$U(J)$ \ $R_s(Pa)$	640 - 1014	1014 - 1388	1388 - 1762	1762 - 2136	2136 - 2510	2510 - 2884	2884 - 3258	3258 - 3632	3632 - 4006	4006 - 4380
0.004 - 0.008	2	0	0	0	0	0	0	0	0	0
0.008 - 0.012	1	3	1	0	0	2	0	0	0	0
0.012 - 0.016	2	2	3	2	0	0	0	0	0	0
0.016 - 0.02	1	1	2	1	0	0	0	0	0	0
0.02 - 0.024	0	2	0	3	1	1	0	0	0	0
0.024 - 0.028	0	1	0	2	2	0	1	0	0	0
0.028 - 0.032	0	0	1	1	1	0	0	0	0	0
0.032 - 0.036	0	0	0	0	1	0	0	0	0	0
0.036 - 0.04	0	0	0	0	0	0	0	0	0	0
0.04 - 0.044	0	1	0	0	2	0	0	0	0	1
									Total	44

Figure 2.23 - A bivariate joint frequency distribution of total input of energy to the system *(U)* and freeze-bond shear strength (R_s) for the data set consisting of 44 measurements of ductile samples.

For future statistical models of experiments it might be interesting to check the assumption of normality for $F1$, A and R_s. As it can be seen from Figure 2.1 and Figure 2.21, neither the histogram of R_s nor that of A can be represented by a normal

distribution. Despite the short tail of left part of the distribution for *F1* the histogram of *F1* seems to be closer to a normal distribution. Normality test for both whole data set of *F1*, R_s and *U=0.0007A* and only for ductile samples is given in Appendix F. From the plots in this Appendix it can be seen that distributions other than the normal distribution should be used for both entire data sets of *F1*, *U* and R_s and for the same sets with only ductile samples. The non-normality of data might have come partly from the experimental setup and partly from the nature of freeze-bonds.

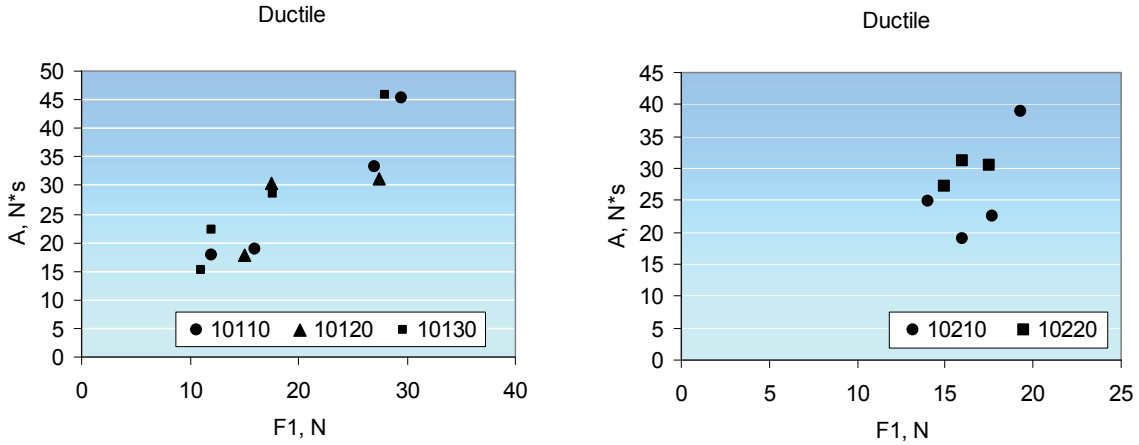

(a) (b)

Figure 2.24 - Area under the curve *F(t)* prior to failure (*A*) versus post-peak force (*F1*), (ductile samples): (a)- Test series 10100, FB submersion time of 20hours; (b) - Test series 10200. Vertical confinement is approximately 660Pa.

2.2 Numerical Results of the Freeze-bond Shear Strength Simulations

In this section numerical solutions to the problem described in Section 1.5 are presented.

3.2.1 Three-dimensional model (3 elements)

A finite element solution for the three-dimensional problem with tuned CE properties is shown in Figure 2.25 (black). The procedure of matching experimental solution with experimental results was described in Subsection 1.5.2.1 of Section 1.5.

In Figure 2.25 reaction force during simulations was calculated as the sum of reaction forces at nodes to which horizontal displacements were applied.

Tuned parameters of cohesive elements, corresponding to the evolution of force in time, (Figure 2.25) were following:

→ CE penalty stiffness $K^*_N = K^*_T = K^*_S = K^* = 2.9MPa$, which corresponds to the elastic modulus of FB $E = 1.45kPa$ for the FB thickness of 0.5mm;

→ Maximum CE traction $T_{0N} = T_{0T} = T_{0S} = T_0 = 10.5kPa$;

→ CE Fracture energy $\Gamma_{0N} = \Gamma_{0T} = \Gamma_{0S} = 22.3N/m$, which corresponds to the physically implausible values of critical separation for given TSL shape (Figure 1.15) as usually brittle materials are considered as materials with a low value of δ_0, varying in the range of a few microns.

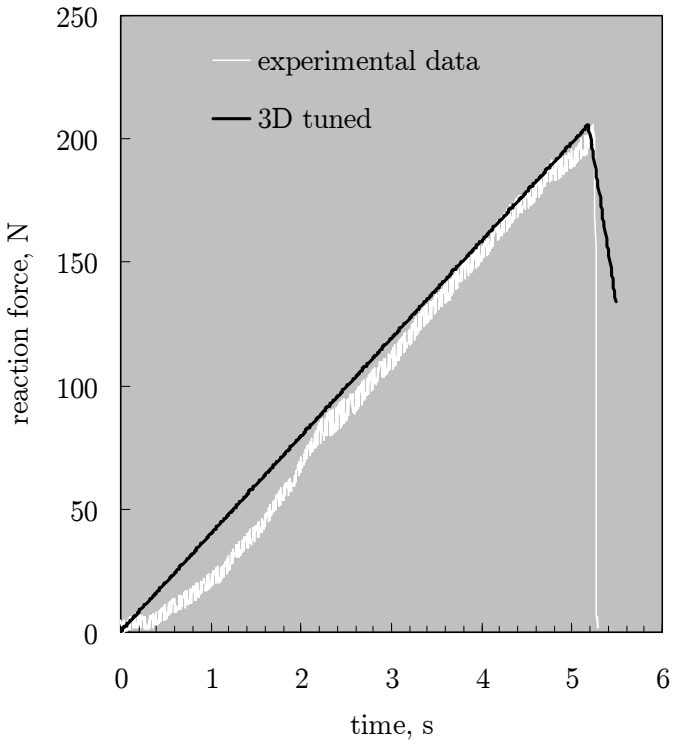

Figure 2.25 - A force history during experiment and during simulations.

The value of the peak force was governed by the value of the maximum traction and the penalty stiffness of the CE (i.e. elastic part of the TSL), while the post-peak behavior was defined by the specified value of the fracture energy.

3.2.2 Considerations on the effect of the problem formulation

The choice of the mathematical model is dependent on the skills and experience of modeler. The following subsections present results of examinations of: (i) the influence of two- and three-dimensional analyses on the value of reaction force (calculated as the sum of reaction forces at nodes to which horizontal displacements were applied); (ii) the influence of the static and dynamic analysis on the value of reaction force (calculated as the sum of reaction forces at nodes to which horizontal displacements were applied); (iii) the influence of the nonlinear geometry on the value of reaction force (calculated as the sum of reaction forces at nodes to which horizontal displacements were applied); (iv) the influence of choice of the cohesive model used for simulating de-bonding on the value of reaction force (calculated as the sum of reaction forces at nodes to which horizontal displacements were applied).

3.2.2.1 Two-dimensional versus three-dimensional model

Two-dimensional FE model was formulated using material properties, which were found by trial and error so as to match experimental results with the numerical solution for the three-dimensional problem (Figure 1.29). For the model consisting of the two plane-stress (CPS4) solids and CE (COH2D4) with out-of-plane thickness equal to 0.14 (Figure 1.30) no differences between reaction forces in two- and three-dimensional model were found. There was almost no difference in the reaction forces calculated using plane-stress or plane-strain formulation as the reaction force is mainly defined by the behavior of CE that doesn't feel the differences between plane-stress and plane-strain.

3.2.2.2 Static versus dynamic analysis

One of the reasons for choosing dynamic explicit analysis was that stresses and displacements can be greater in the dynamic model than in the static model. Besides, as was mentioned earlier, explicit methods are better at handling dynamic problems involving complex contact conditions.

In order to compare implicit static analysis with explicit dynamic in the presence of cohesive elements a simplified model of pure shear was considered (Figure 2.26).

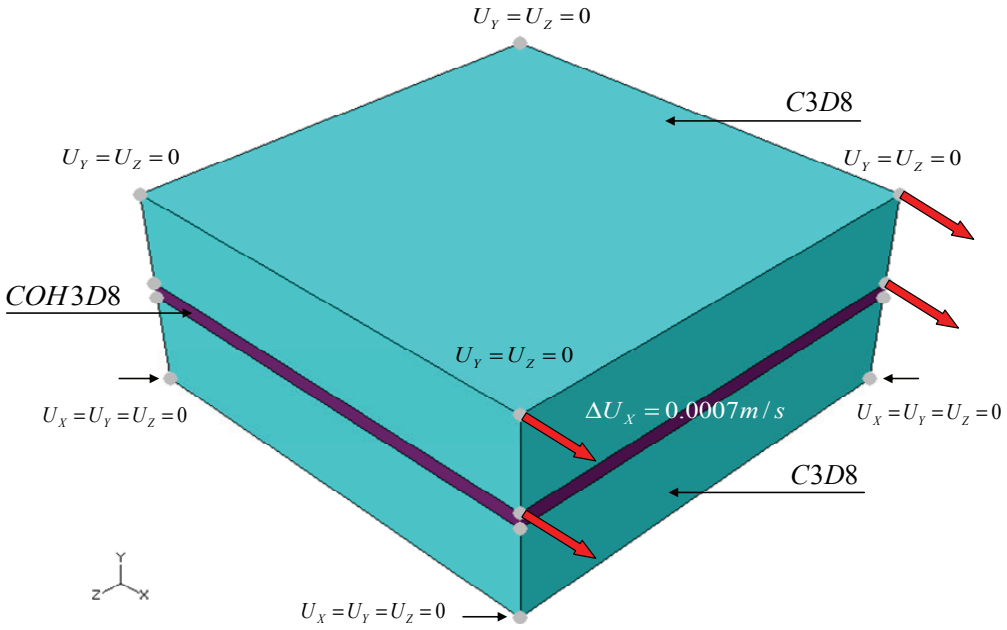

Figure 2.26 -A finite element model for the pure shear test.

Finite element formulation of the dynamic problem (Equation 1.10, Equation 1.19) leads to a system of nonlinear equations (Equation 1.43). Equation 1.43 was solved using an explicit central-difference time integration scheme (Subsection 1.3.4.2) in ABAQUS/Explicit.

Figure 2.27 shows reaction forces calculated using dynamic and static approaches. In Figure 2.27 the reaction force during simulations was calculated as the sum of reaction forces at nodes to which horizontal displacements were applied. The numerical solution in Figure 2.27 (white curve) oscillates about the static solution (black line) in a damped manner. The oscillatory behavior is not realistic. It is the numerical effect introduced by the initial load step.

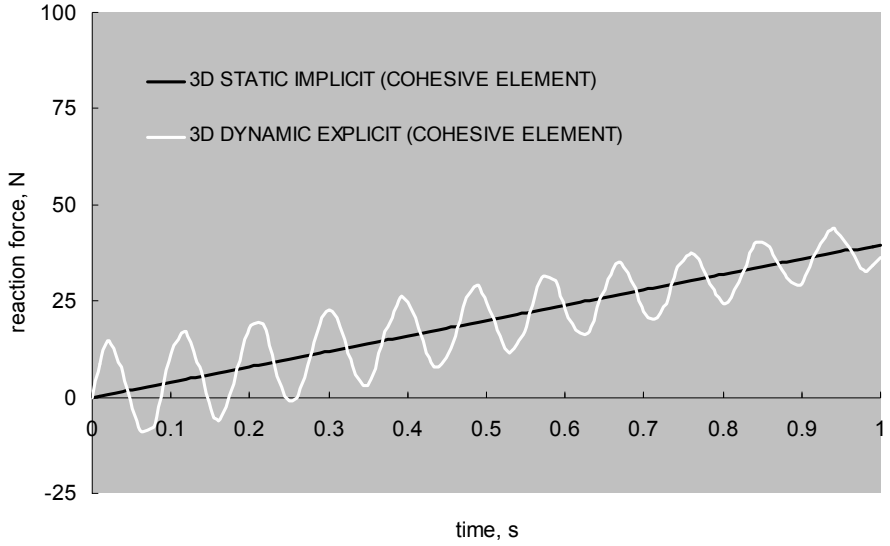

Figure 2.27 - Static versus dynamic analysis.

3.2.2.3 Effect of geometrical nonlinearities

No large deformations effects were found in neither 2D nor 3D models. Resulting reaction force calculated with account of nonlinear geometry effects (step, nlgeom=YES) was almost the same as the reaction force obtained through the geometrically linear analysis (step, nlgeom=NO).

3.2.3.4 Cohesive element versus contact surfaces

A contact interaction model (similar to the model in Figure 2.26) was used to simulate de-cohesion of initial bonded ice pieces. Instead of inserting a cohesive element between two continuum elements the interaction between two ice pieces was simulated using a *surface-based cohesive behavior*. The surface-based cohesive behavior was modeled within the general contact framework in ABAQUS/Explicit (see ABAQUS 6.8 Section "Contact formulation of general contact in ABAQUS/Explicit"). The surface-based behavior was specified in terms of traction-separation similar to the response of the cohesive elements. Input files for the surface-based cohesive model and for the model in Figure 2.26 are given in the Appendix D2. Though the same constitutive behavior in terms of tractions and separations was specified and the same cohesive properties were chosen for both surface-based and cohesive zone models, it is important to remember that the damage in surface-based cohesive behavior is an interaction property and not a material property. Definitions of strains and displacements (used for cohesive elements) here are reinterpreted as contact

separations. Contact separations are understood to mean relative displacements between the nodes on the slave surface and their corresponding projection points on the master surface along the contact normal and shear directions. For surface-based model stresses were defined in ABAQUS as the cohesive forces acting along the contact normal and shear directions divided by the current area at each contact point. Besides, thickness effects are not considered for cohesive surfaces. To exclude the thickness effect form the cohesive element formulation the constitutive element thickness in the Y direction (Figure 2.26) was set to 1.0 which implies $\varepsilon_N = \delta_N; \varepsilon_S = \delta_S; \varepsilon_T = \delta_T$ for the cohesive element. In Figure 2.28 differences among calculated values of reaction forces are shown for the surface-based model (dashed line); static cohesive zone model (black solid line) and dynamic cohesive zone model (white solid line).

Reaction force in Figure 2.28 was calculated as the sum of reaction forces at nodes to which horizontal displacements were applied. As it can be seen from Figure 2.28 the differences between the reaction forces calculated for different models are not significant.

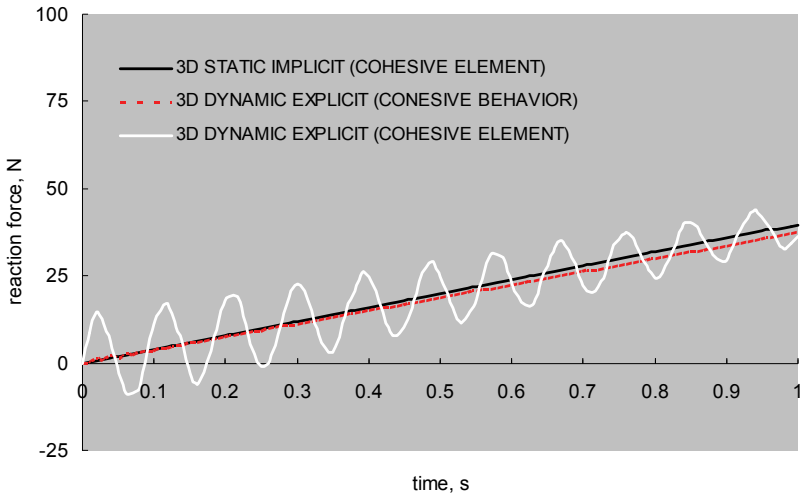

Figure 2.28 - Numerical solution for the static cohesive zone model (black); dynamic cohesive zone model (white) and surface-based cohesive model (dashed line).

3.2.3 Influence of the boundary conditions

The calculated reaction force of the model described in the Section 1.5 was unaffected by the change of the vertical pressure as a cohesive element doesn't undergo damage under compression. The change of the vertical pressure led to the change of the stress state in the continuum elements while the total reaction force (in the direction opposite to the specified displacements) remained unchanged.

Displacements applied in the direction opposite to what is given in Figure 1.29 correspond to the process of ice pushing (instead of pulling). Such change in the loading direction changed the stress state of the continuum elements but it didn't

affect the reaction force as the damage in tangential directions can occur in both ways as it shown in Figure 1.16b.

3.2.4 Influence of the finite element mesh

Two different finite element meshes (*Discretization A* and *Discretization B*) were considered (Figure 2.29). *Discretization A* of the 3D model was done by using sweep meshing technique in ABAQUS/CAE while *Disretization B* was built from the bottom-up approach using the input file. The cohesive element in case of *Discretization B* had zero geometrical thickness while CEs in *Discretization A* had a thickness of 0.5mm (ABAQUS/CAE requires an artificial thickness of the FB). To exclude the thickness effect a constitutive thickness of 1.0 was assumed for the cohesive elements. *Discretization B* in Figure 2.29 was similar to the discretization used in Gürtner (2009b).

Material parameters, boundary conditions and loads were the same as for the model described in Section 1.5. The size of the considered problem for different FE meshes is summarized in Table 2.5.

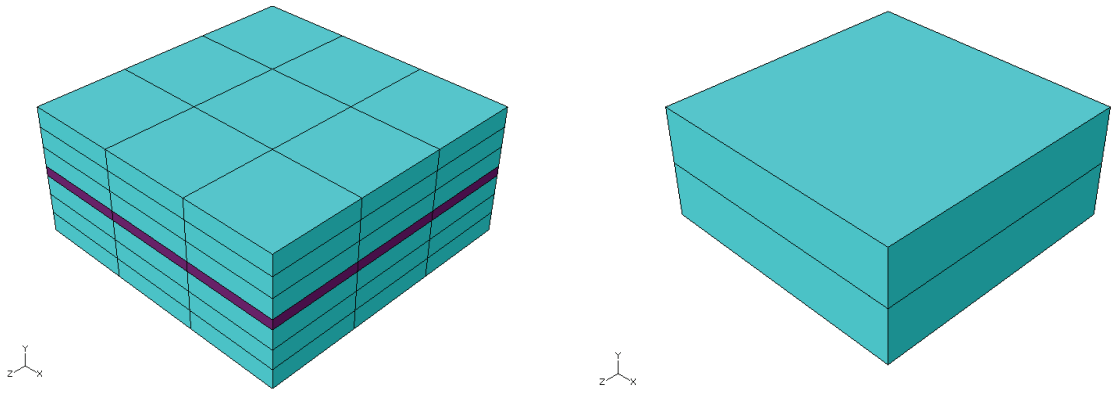

Discretization A (ABAQUS/CAE) *Discretization B* (Input file)

Figure 2.29 - Finite element discretizations.

Calculated reaction force is shown in Figure 2.30 for the *Discretization A* (solid line) and for the *Discretization B* (dashed line).

Table 2.5 - Summary of problem size

	Discretization A	Discretization B
Number of elements	63	3
Number of nodes	128	16
Total number of variables	384	48

As it can be seen from Figure 2.30 there is almost no influence of the finite element mesh on the reaction force, although there was a difference in the stress state in the whole ice sample (Figure 2.31).

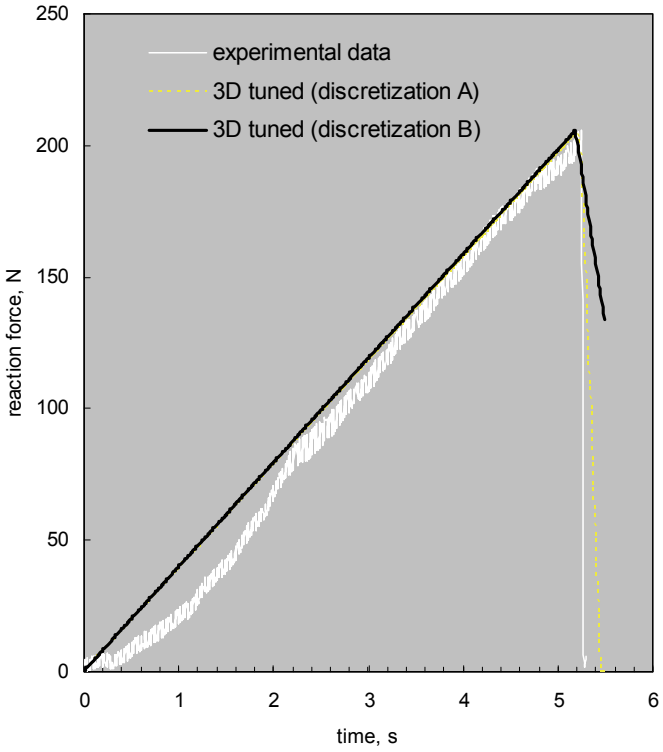

Figure 2.30 - Influence of the finite element mesh on the reaction force: the *Discretization A* (solid line), the *Dicretization B* (dashed line).

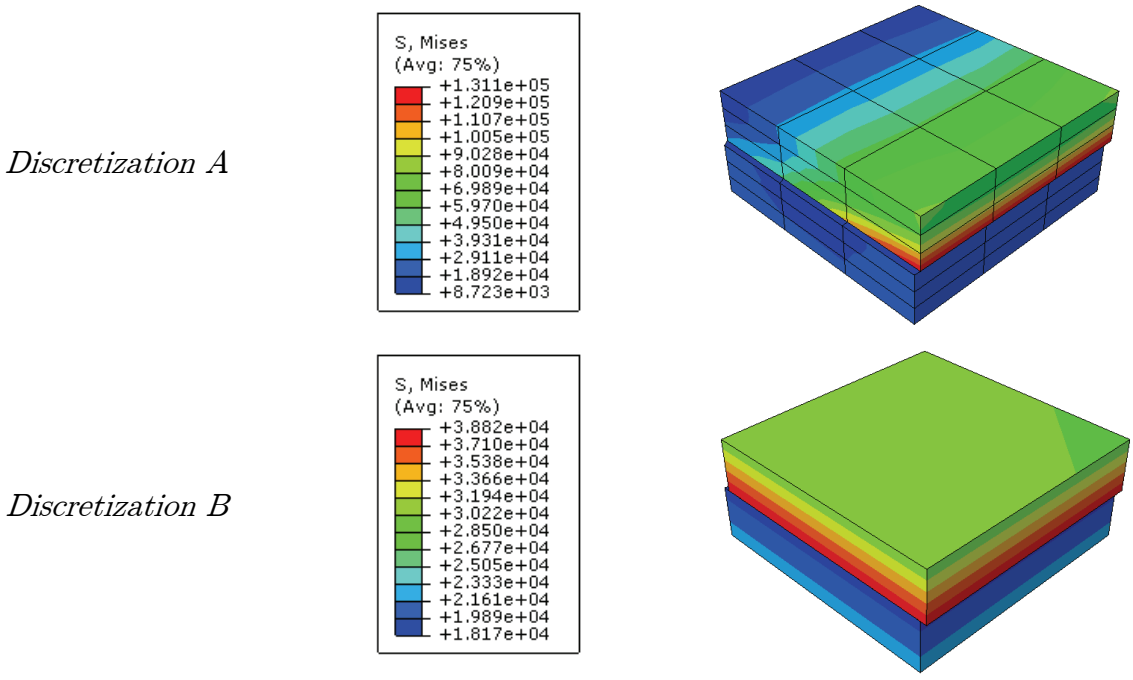

Figure 2.31 - von Mises stress created by ABAQUS/CAE at time corresponding to the peak value of reaction force.

For the *Discretization A* it was possible to decrease the value of the fracture energy ($\Gamma_{0N} = \Gamma_{0T} = \Gamma_{0S} = \Gamma_0 = 20N/m$ in order to simulate the sharper load drop measured during experiment while for the *Discretization B* the decrease of the Γ_0 lower than 22.3N/m was not possible due to limitations required for the convergence of numerical solution.

The smaller the element size the closer is the stress state to the physical reality. Probably, with decreasing the element size (element shape being the same) and by tuning the value of the fracture energy it will be possible to reach more realistic stress state and a more physically plausible value of critical separation.

3.2.5 Effect of the material parameters on the fracture behavior

To explore the effect of varying parameters of both cohesive and solid elements some numerical trials based on the three-dimensional model in Section 1.5 were done. The objective of the numerical simulations was to identify the significant parameters affecting the evolution of reaction force in time. A design and analysis of numerical experiment were done in accordance with Chapter 9 in Antony (2003) and Trumars (2009).

The responses of interest in the simulations were the maximum reaction force (F_{max}) registered during first six seconds of sliding with the speed of 0.0007m/s and time $t(F_{max})$ at which F_{max} is occurred. The reaction force itself was calculated as the sum of reaction forces at nodes to which displacements were applied.

Four main effects and three two-order and one three-order interactions were identified from the experience gained through the tuning procedure (Subsection 1.5.2.1). Under two-order interaction it is considered that the effect of one of the variables differs depending on the level of the other variable.

The value of the fracture energy affects the response of cohesive element only if its damage had occurred. Influence of the fracture energy on the behavior after damage will be considered separately. The list of main and interaction effects is shown below:

Main effects: Maximum traction (T_0); Penalty stiffness of CE (K^*); Elastic modulus of ice (E)
Interaction effects: $T_0 \times K^*$; $T_0 \times E$; $E \times K^*$ and $T_0 \times E \times K^*$

Each parameter was studied in three levels. The ranges of parameters are shown in Table 2.6.

Table 2.6 - List of factors and their ranges for the numerical experiments.

Parameters	Labels	Units	Low level	Medium level	High level
Maximum traction	T_0	kPa	5	10.5	70
Penalty CE stiffness	K^*	MPa	1.5	2.9	20
Elastic modulus of ice	E	MPa	50	200	350

The uncoded design matrix showing all the real factor settings along with their respective response values is shown in Table 2.7.

For the high values of maximum traction and low values of penalty CE stiffness the cohesive element often didn't undergo any damage within considered time frame (six seconds). In Table 2.7 such trials can be distinguished from the rest as for them the value of $t(F_{max})$ was equal to six. For the trials 12, 15 and 18 it was necessary to increase the value of fracture energy up to 23N/m in order to satisfy requirements of convergence. For rest of the samples Γ_0= 22.3N/m. Therefore statistical analysis and interpretation of the numerical results was done only for the trials with Γ_0= 22.3N/m which was treated as a full two-level factorial design with three factors.

Table 2.7 - Uncoded design matrix with response values (T_0 - maximum traction; E - elastic modulus of ice; K^* - penalty stiffness of CE; F_{max} - maximum reaction force; $t(F_{max})$ - time measured from beginning of sliding; S_l' - ratio between F_{max} and $t(F_{max})$ or loading slope).

Standard order	To, kPa	E, Mpa	K*, MPa	Fmax, [N]	t(Fmax), [s]	S_l', [N/s]
1	5	50	1.5	97.9	4.8	20
2	5	50	2.9	98	2.51	39
3	5	50	20	97.9	0.4	245
4	5	200	1.5	98	4.77	21
5	5	200	2.9	97.9	2.48	39
6	5	200	20	98	0.37	265
7	5	350	1.5	98	4.77	21
8	5	350	2.9	98	2.47	40
9	5	350	20	97.9	0.37	265
10	10.5	50	1.5	122.4	6	20
11	10.5	50	2.9	205.7	5.26	39
12	10.5	50	20	205.4	0.84	245
13	10.5	200	1.5	123.2	6	21
14	10.5	200	2.9	205.6	5.19	40
15	10.5	200	20	205.5	0.78	263
16	10.5	350	1.5	123.3	6	21
17	10.5	350	2.9	205.6	5.18	40
18	10.5	350	20	205.5	0.77	267
19	70	50	1.5	122.4	6	20
20	70	50	2.9	234.8	6	39
21	70	50	20	1479.8	6	247
22	70	200	1.5	123.2	6	21
23	70	200	2.9	237.7	6	40
24	70	200	20	1600.2	6	267
25	70	350	1.5	123.3	6	21
26	70	350	2.9	238.2	6	40
27	70	350	20	1619.5	6	270

Though the built numerical model is fully deterministic, a determination of significant main and interaction effects was done.

The results for main and interaction effects for F_{max} , $t(F_{max})$ and S_1' are illustrated in Figures 2.32 2.33 and 2.34 respectively. Effects were calculated as in the example presented by Trumars (2009). The ice friction, ice thickness and velocity in that example correspond to T_0, K^* and E, respectively, in this study. The values of $y_1 \ldots y_8$ in the example correspond to the responses of interest for trials 1, 19, 7, 25, 3, 21, 9, and 27 (Table 2.7) respectively. Effects were compared with the average (dashed line) of each response ($t(F_{max})$ and F_{max}) and S_1'. It can be seen that some effects are comparable with the average and it is reasonable to expect that these effects have a significant impact on the result.

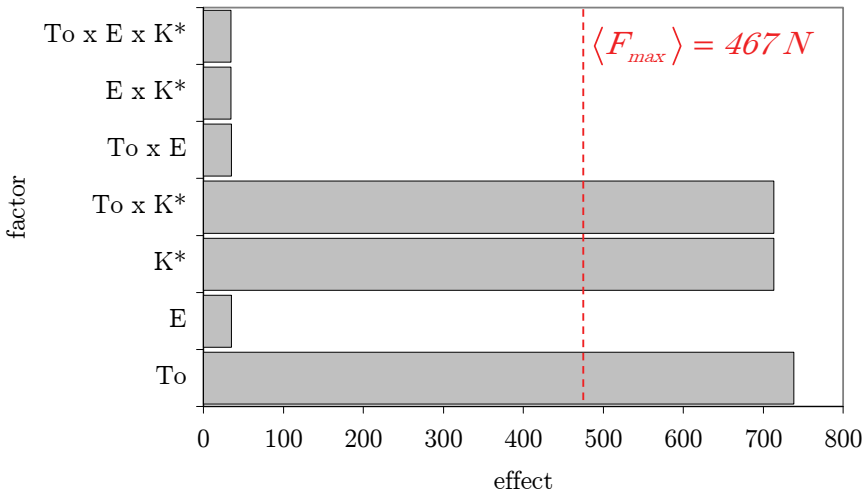

Figure 2.32 - A plot of effects for F_{max}.

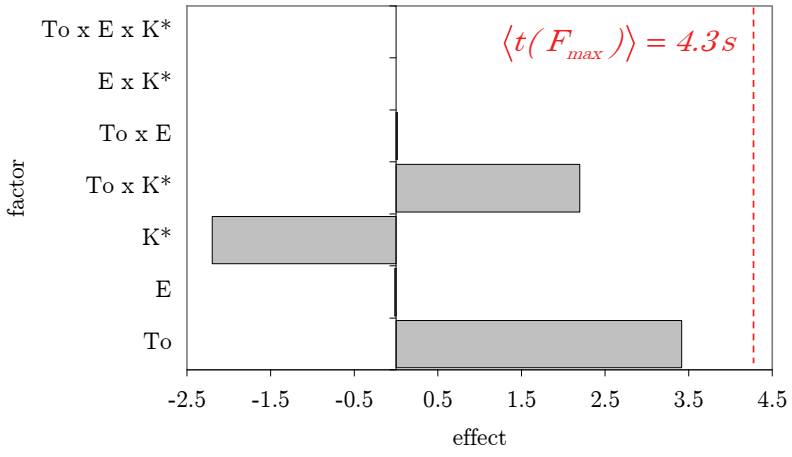

Figure 2.33 - A plot of effects for $t(F_{max})$.

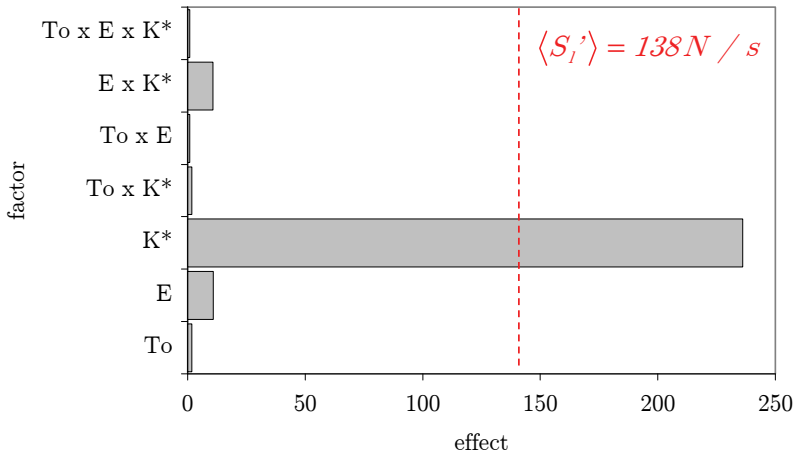

Figure 2.34 – A plot of effects for S_l'.

The plots in Figure 2.32 and Figure 2.33 indicate that factors T_0 , K^* and their interaction have a significant impact on the maximum reaction force and time at which this force is reached, while the plot in Figure 2.34 shows that factor K^* has a significant effect on the loading slope. It is should be noted that due to the fact that cohesive element hasn't been damaged during trials 19, 25, 25 and 27, the effect of K^* on F_{max} is significantly overestimated and therefore results obtained via analysis in this section should be treated with accuracy.

From Table 2.7 it can also be seen that change in T_0 affects both F_{max} and $t(F_{max})$ in the same way, so S_l' remains unaffected. From the analytical point of view it simply can be explained by that fact that in the mathematical model T_0 is parameter responsible for a damage initiation and therefore behavior prior to the damage is unaffected by this parameter.

From Figure 2.32 to 2.34 it can be seen that the effect of E on F_{max}, $t(F_{max})$ and S_l' is significantly less than the effect of K^* on those. From Table 2.7 it can be seen that for fixed T_0=10.5kPa and K^*=2.9MPa influence E on $t(F_{max})$ and S_l' is higher than on F_{max}. The interaction effect between E and K^* for T_0=10.5kPa on F_{max} is illustrated in Figure 2.35.

Figure 2.35 shows that the difference between the maximum reaction forces obtained for K^*=20MPa and K^* = 2.9MPa is greater for the trials with smaller E. There was almost no difference among maximum reaction forces obtained with high E values. For K^*=2.9MPa an increase in E resulted in a slight decrease of maximum force, while for the K^*=20MPa an increase in E had the opposite effect. These variations in behavior for different E were less important than those for K^*. Effect of K^* will be discussed later.

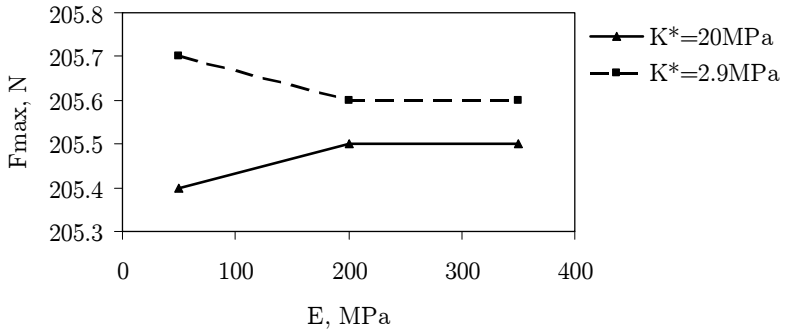

Figure 2.35 - Interaction plot of E versus K*.

From the above the following conclusions can be made:

→ Peak force F_{max} is completely determined by the maximum traction strength and the initial part of TSL. The linear behavior prior to peak load is determined by the penalty stiffness of cohesive element and only partly affected by the elastic material properties of ice.

→ Material properties of freeze-bond are more important than properties of ice for the given model as all significant effects on considered responses related to them.

The effects of cohesive element properties are discussed below.

3.2.5.1 Effect of the cohesive element stiffness

For F_{max} , $t(F_{max})$ and S_I' the cohesive element penalty stiffness K^* is one of the main effects which was considered to be significant. Figure 2.36 illustrates its effect on the S_I' value. The data for the plot in this figure were taken from Table 2.7. The effect of K* on the value of F_{max} for trials where damage of cohesive element have occurred, can be considered insignificant.

The increase in K^* resulted in increase of S_I'. Linear dependency between K^* and S_I' is explained by Equations 1.30a, 1.30b, and 1.32 in Subsection 1.3.3 and the fact that due to loading conditions horizontal displacements at nodes (Figure 1.29) were proportional to the time t.

As can be seen from Figure 2.36 the closer the stiffness of the cohesive element to the ice elastic constant E the more sensitive is the loading slope to a change in the value of E.

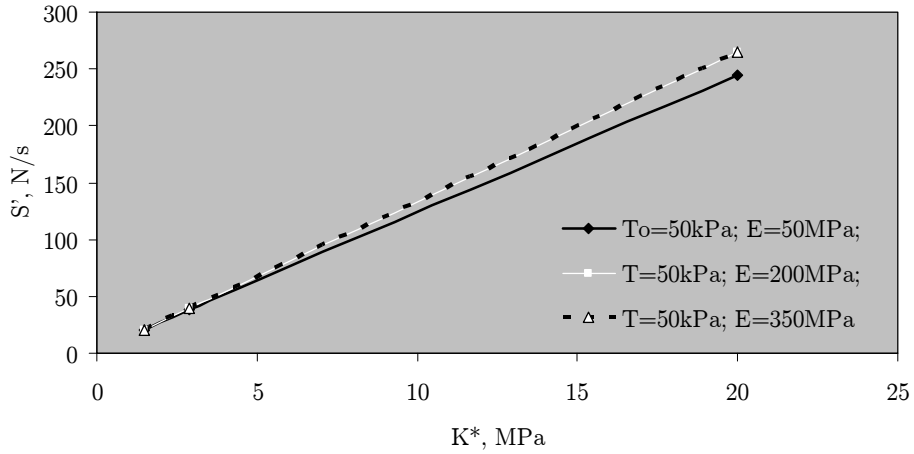

Figure 2.36 - Effect of cohesive element stiffness on loading slope.

3.2.5.2 Effect of the maximum traction

For F_{max}, $t(F_{max})$ the maximum traction is certainly significant (Figures 2.32 and 2.34). Figure 2.37 illustrates the effect of the maximum traction on the value of maximum force. The higher the value of maximum traction the higher was the maximum force. As the loading slope is unaffected by the maximum traction (Figure 2.34) therefore it is to be expected that $t(F_{max})$ also increases when maximum traction increases. Perhaps the dependency between maximum traction and maximum force is linear and non-linearity in Figure 2.37 can be explained by that fact that the cohesive element didn't undergo any damage (within six seconds of sliding) when the maximum traction was equal to 70kPa and therefore if the sliding were allowed for more than six seconds it is expected that the value of maximum force corresponding to the damage initiation of cohesive element will be much higher than is shown in Figure 2.37 (a point labeled as *"no-damage"*).

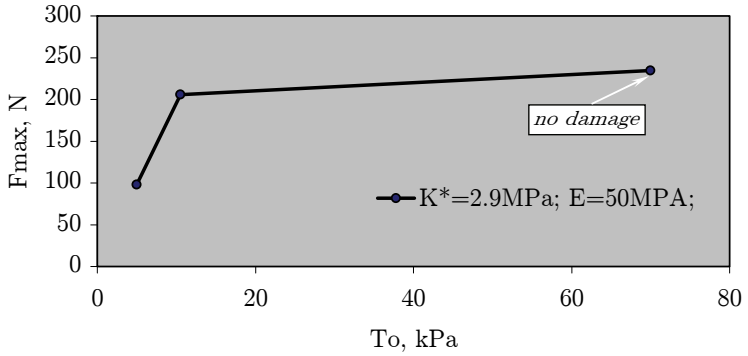

Figure 2.37 - Effect of maximum traction on maximum load.

3.2.5.3 Effect of the fracture energy

The value of the fracture energy affects the post-damage behavior of a cohesive element (Figure 2.38). A higher energy resulted in a bigger value of the area under the

TSL (Equation 1.20). Hence the post-peak slope in Figure 2.38 increased with the fracture energy. The reaction force in this figure was calculated as the sum of reaction forces at nodes to which displacements were applied; the values of reaction force correspond to E=200MPa, K^*=2.9MPa and T_0=10.5Pa.

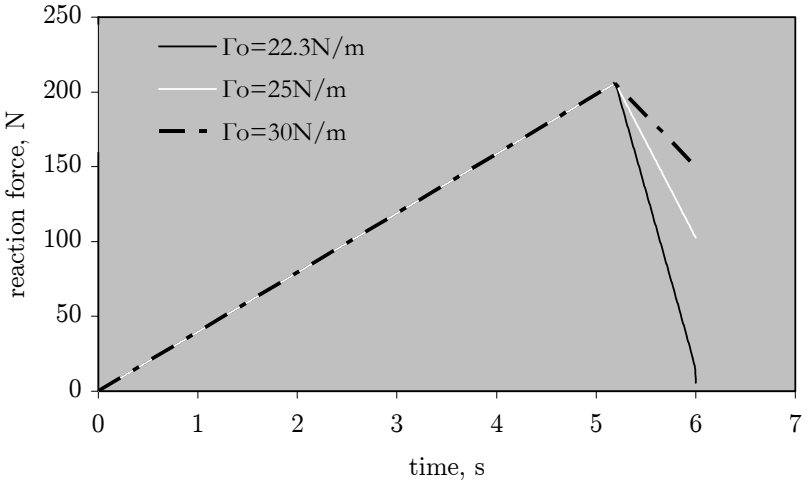

Figure 2.38 - Effect of fracture energy on evolution of reaction force in time.

ANALYSIS AND DISCUSSION 3

This chapter covers the following topics:

- → Discussion of some results presented in Chapter 2 and their comparison with previous studies;
- → Uncertainties of results presented in Chapter 2;
- → Discussion on a model ice microstructure and freeze-bond failure;
- → Finite element model of the freeze-bond shear test;
- → Modeling of ice-ridge structure interactions.

A short summary of the work is presented at the end of the chapter.

3.1 Freeze-Bond Shear Strength

The freeze-bond shear strength obtained from all experiments in Repetto-Llamazares, et al. (2009b) was $2.7 \pm 2.3 kPa$ which is one order of magnitude lower than the freeze-bond shear strength in the ridge keel, reported in the third chapter in Vershinin, et al. (2005). The obtained results of experiments (Repetto-Llamazares, et al. 2009b) were difficult to compare with earlier results of freeze-bond shear strength due to the following reasons:

- → Ice used in previous studies had different initial salinity and temperature;
- → Tested ice samples had different shape and size;
- → Experimental setup was not the same (different time to create freeze-bond was used as well as different confining pressure);
- → Loading procedure varied from one author to another (see Appendix A).

Even if the comparison of the results can be made using some assumptions it will not be possible to judge whether the obtained difference is due to use of model HSVA ice or due to the assumptions that were made.

It is unclear why the Log-Logistic distribution in Figure 2.1 approximated measured shear capacity of freeze-binds so well. It is uncertain whether it says something about the physics of freeze-bond sear capacity or it is simply related to the flexibility of the distribution and limited number of measurements. Nevertheless, it is interesting to note that Log-Logistic distribution also represents well the inferred heat flux over most of the Earth (Shapiro and Ritzwoller, 2004).

The decrease in the freeze-bond shear capacity at the higher temperatures (Figure 2.4) can be explained by the increased effect of ice softening near its melting point.

It was difficult to comment on the behavior of brittle samples (Figure 2.6), due to lack of data. From the experiments of Repetto-Llamazares, et al. (2009b) it was not possible to draw conclusions on whether the brittle behavior occurs randomly or whether there is a factor provoking such behavior?

As ice is a material with non-uniform properties varying in space and time, it is difficult to ensure that the ice sample to be tested next will have the same properties as the previous sample. Therefore the number of ice samples, prepared in order to make some statistics, should be larger than the recommended number for experiments with engineering materials as concrete, metal, ceramics and even soil. A randomized test setup might be applied to smooth results due to natural variability of ice.

In Subsection 2.2.5, due to the lack of additional information it was not possible to comment further on whether or not the microcrack was already initiated at lower yield point and subsequently followed by a main crack leading to failure of the freeze-bond. Hence it was difficult to say something about the fracture energy of ice itself from the conducted experiments without any further assumptions. Thus we could speak only about the area under the loading curve which indicates the total input of energy to the system.

For the ductile samples the higher energy input into the system (higher the value of freeze-bond shear capacity, higher the value of the area under the loading curve) resulted in a bigger height of the asperities created by the crack grow and fracture. Sinha (1982) argues that grain boundary sliding resulting initiation of microcracks which appear when critical delayed elastic strain is reached. This occurs when shear stress is generated across the grain boundaries and depends on the grain size. In accordance with Sinha (1979, 1982) large grains give longer time to start crack nucleation. Therefore if the bigger grains give higher ductile shear strength it could also lead to rougher surfaces. Hence, assuming that rate of change of asperity height is the same for all samples during the first second of post-peak behavior, the observed correlation between the area and the post-peak force *F1* in Figure 2.24 is straightforward.

3.1 Ice-Ice Friction in Freeze-Bonds

The ice-ice friction in freeze-bonds discussed in this section is, to the best of author knowledge, new, and suggests many avenues for further investigation.

In Subsection 2.2.4 factors affecting the coefficient of ice-ice friction included the roughness and hardness of the surfaces in contact and the type of molecular interaction between them. Modern sciences of surfaces, abrasion, and lubrication explain sliding friction in terms of chemical bonding and stick-slip processes (Beaty, 2009). The friction coefficient can take different values depending on whether the bodies with their surfaces in contact are motionless (static friction) or moving (dynamic friction). With a decrease in the value of the friction coefficient there is an increase of the error

in case of tilting (Schmitz, et al., 2009). In this study it was not possible to say either if the tested samples were tilted or if the samples started sliding relative to each other. Hence, only a similitude (an approximation) of friction coefficient was obtained.

For the high normal stresses the value of ice-ice friction coefficient similitude $\mu^* = 0.7$ (Subsection 2.2.4) was high in comparison with the reported data on ice-ice friction coefficient (Maeno, et al., 2003). From the other side the value of $\mu^* = 0.7$ (Subsection 2.2.4) agrees well with Lishman, et al. (2009), where authors report time-averaged ice-ice friction coefficient μ=0.6 for the slip rate of 3mm/s (experiments in the HSVA ice tank). They also mention relatively high roughness of the contact surfaces with visible asperities and notches on the millimetre scale.

Table 3.1 describes measurements of ice-ice friction coefficient similitude for model ice (μ^*) compared with ice friction coefficient (μ) measurements conducted by different authors.

Table 3.1 - Comparative table

Frederking and Barker (2002)	**Repetto-Llamazares, et al. (2009b) & This study**
Friction of sea ice on various construction materials, with known roughness	*Ice-ice post failure behavior, surface roughness is unknown*
?	*Constant velocity test*
The frictional force varies substantially*, even when the normal force is constant. Two different frequencies observed for the different samples would appear to be a function of the sample material surface.	Stick - slip force oscillations were noted.
Speed and specimen roughness has the strongest influence.	Ice surface roughness after the failure probably had the strongest influence.
Temperature has a weak effect on friction coefficient. There is also a weak trend of lower friction coefficient at higher contact pressure.	The temperature effect was complex. Friction coefficient similitude decreased with increasing normal stress.
Considerable variability in friction coefficient values over a single test sample is observed.	There were differences between one sample and another, the test parameters were being the same.

* Load oscillations were not related with stick-slip motion.

Fortt, et al. (2003)	**Repetto-Llamazares, et al. (2009b) & This study**
Sliding along the Coulombic shear faults in ice	*Freeze-bond shear strength experiments and ice-ice post failure behavior*
Fresh water S2 columnar ice grown in laboratory	*HSVA saline ice*
Constant velocity test	*Constant velocity test*

At high displacement velocities (0.8mm/s) the deformation is noisy. The applied stress increases, reaches a maximum, and then drops suddenly, followed by a "stick-slip". At intermediate speeds (0.08mm/s) the deformation is less noisy. Stress versus displacement curves is characterized by an initial rapid increase, followed by a gradual rising to a rounded peak. There is no sudden-type failure; instead the stress gradually decreases.	For the velocity used in the experiments (0.7mm/s) stick-slip force oscillations were noted. Force versus time curves (after theirs peak) were characterized by sudden load drops and by a gradually decreasing force.
A little effect of grain size (column diameter) of the parent specimen on the behavior.	???
There is little evidence of damage extending beyond the fault into adjacent material.	Ice failed along the freeze-bond.
Within the lower confinement or sliding* range, the shear strength of the fault increases with increasing normal stress.	Freeze-bond strength slightly increased with increasing of normal pressure.
The concept of brittle versus ductile behavior is applied to the sliding* deformation of ice. At higher speeds (i.e., Vs > 0.08 mm/s) sliding* exhibits brittle-like behavior, which is characterized by sudden load drops and by strain-rate softening, while at lower speeds (e.g. Vs = 0.0008 mm/s) it exhibits ductile-like which is characterized by strain-rate hardening.	Attempt to apply the concept of brittle versus ductile behavior to the freeze-bond failure process has been done based on the post-peak behavior. It was not clear if such a criterion is a valid measure.
Within the brittle-like regime, the shear resistance obeys a power-law dependence on normal stress at the onset of sliding*, while once sliding* has commenced it obeys Coulomb's law. The parameters of Coulomb law are essentially independent of displacement.	Freeze-bond strength slightly increased with increasing of normal pressure. From the linear, power, exponential and logarithmic trend types, the 'power type' had the highest correlation coefficient (r^2); but still the value of r^2 was too low (< 0.5) to consider a power law as description of relationship between the freeze-bond shear strength and normal pressure (see Appendix C1). Beyond the failure (at the end of one second) the shear resistance increased linearly with normal stress and obeyed Coulomb's law.
It is likely that the onset of sliding requires the breaking of bonds that	Sliding* required the breaking of freeze-bonds.

reformed during the time lapse between the faulting and the sliding* stages.	

* "Sliding" means deformation within a narrow band of damage (i.e., the fault). That kind of deformation is rather chaotic and probably consists of a complicated mixture of several processes, including interfacial sliding, fracture, and melting and, at the lower speeds, creep and sintering.

Vs - sliding velocity

Maeno, et al. (2003)	Repetto-Llamazares, et al. (2009b) & This study
Pure polycrystalline distillated water ice	*HSVA saline ice*
Both surfaces were finished flat and smooth with careful planning	*Surfaces represent ice interface just after the failure*
Saw-toothed, stick-slip frictional behavior is noted for sliding velocity roughly from 10^{-3} to 10^{-5}m/s.	Saw-toothed behavior was dominating for sliding velocity of 0.0007m/s.
Maximum reported value μ=0.46 for sliding velocity of 0.0005m/s at -27°C and normal stress 2.9kPa.	μ^*=0.7 for sliding velocity of 0.0007m/s at -14°C, and normal stress 2.0kPa.
μ temperature dependence is complex	μ^* temperature dependence was complex
At temperatures lower than about -5°C, μ decreases with rise in temperature, but it increase at temperatures higher than - 5°C.	At temperatures lower than about -7°C, μ^* slightly decreased with rise in temperature, but it was almost constant at temperatures higher than -7 °C.
μ decreases with increasing of normal stress but it almost constant above 5kPa.	μ^* decreased with increasing of normal stress.
The temperature dependence of μ_0 resembles that of μ.	The temperature dependence of μ_0^* did not resemble that of μ^*.
The estimated adhesion strength ranges from 10 to 250Pa.	The adhesion strength ranged from 1.2 to 2.1 kPa.
Adhesion strength increases as the temperature is lowered.	Adhesion strength increased as the temperature was lowered.

Nanetti, et al. (2008)	Repetto-Llamazares, et al. (2009b) & This study
Saline ice-steel friction, roughness of steel surface is known	*Ice-ice post failure behavior, surface roughness is unknown*
Creep test, Saline ice	*Constant velocity test, HSVA saline ice*
A stick-sleep motion with a characteristic frequency of 0.1Hz is observed.	Stick-slip force oscillations were noted.
The period decreases with time and tends to become a constant (the higher load the more evident this trend).	In most of the cases period of oscillations corresponded to the sampling frequency of 100Hz.

The amplitude is dampened with time, the higher the load the quicker the effect.	Force amplitude was dampened with time*.
There can be many differences between one sample and another, the test parameters being the same.	There can be many differences between one sample and another, the test parameters being the same.
Knekkis is a step machine, some of observed load oscillations might be due to a systematic behavior of the machine itself and not to the physics of ice/steel interaction.	Some of observed load oscillations might be due to a systematic behavior of the loading device itself and not to the physics of ice/ice interaction.
The ratio of the mean rate of axial displacement to the frequency of stick-sleep oscillations is comparable to the nominal roughness length.	???
The higher the roughness the later the onset of the stick-slip motion, and the higher the amplitude of the oscillations	???

* only one test sample 13_17_1 was considered

Sukhorukov and Marchenko (2009)	Repetto-Llamazares, et al. (2009b) & This study
Interaction of ice with steel surfaces	*Ice-ice post failure behavior, surface roughness is unknown*
Constant velocity test, freshwater ice	*Constant velocity test, HSVA saline ice*
Stick-slip oscillations of the load are observed in all experiments with high and middle surface roughness.	Stick-slip force oscillations were noted.
The axial displacement during stick-slip motion is comparable to the roughness length.	???

3.2 Analysis of Uncertainties

3.2.1 Experimental uncertainties

In the shear tests (Section 1.4) used to measure the shear strength of freeze-bonds, the ice sample in 'split' wooden frames was sheared laterally by moving the top wooden frame relative to the bottom frame, thereby producing a thin failure zone. Besides experimental uncertainties mentioned in Repetto-Llamazares, et al. (2009b), the shear stress generated on the horizontal plane is far from uniform, as failure is expected to propagate from the edges towards the centre of the sample (Figure 2.31, Discretization A). The presence of freeze-bond changes the stress state in the ice sample in comparison with the uniform ice. The cross-sectional area being sheared does not remain constant throughout the test, which makes the analysis of results more

difficult. The actual displacements of the freeze-bond may differ from those measured in the piston of the pulling system.

3.2.2 Model ice uncertainties

Consolidated parts of rafted ice found in ice-ridges were created by the refrigeration procedure under the laboratory conditions. As was mentioned by Zufelt and Ettema (1996) the freeze-bond strength between ice pieces may be insufficiently scaled, as refrigeration is used to consolidate ice piece accumulation. This fact makes comparisons with the full-scale results difficult.

3.2.3 Stick-sleep behavior or effect of the sampling frequency

In Table 3.1 five of six authors (including this study) reported stick-slip oscillations during the process of ice sliding. Besides, for the HSVA ice Lishman, et al. (2009) reports stick-slip behavior observed at low slip rates (3mm/s), with frictional buildup at fixed displacement followed by sudden movement and relaxation of slip.

In this study stick-slip behavior, for example, can be seen for the sampling frequency of 100Hz for the ice sample 13_17_1. Spectral analysis showed that the main frequency of oscillations is equal to the sampling frequency. This raises a question regarding the effect of sampling frequency on the obtained results. In Figures 3.1 to 3.3 the effect of sampling frequency is illustrated for the ice sample 13_17_1. These figures shows the results obtained from the freeze-bond shear test. The test was conducted at -14°C temperature, confinement pressure of 637Pa for submersion time of 20hours.

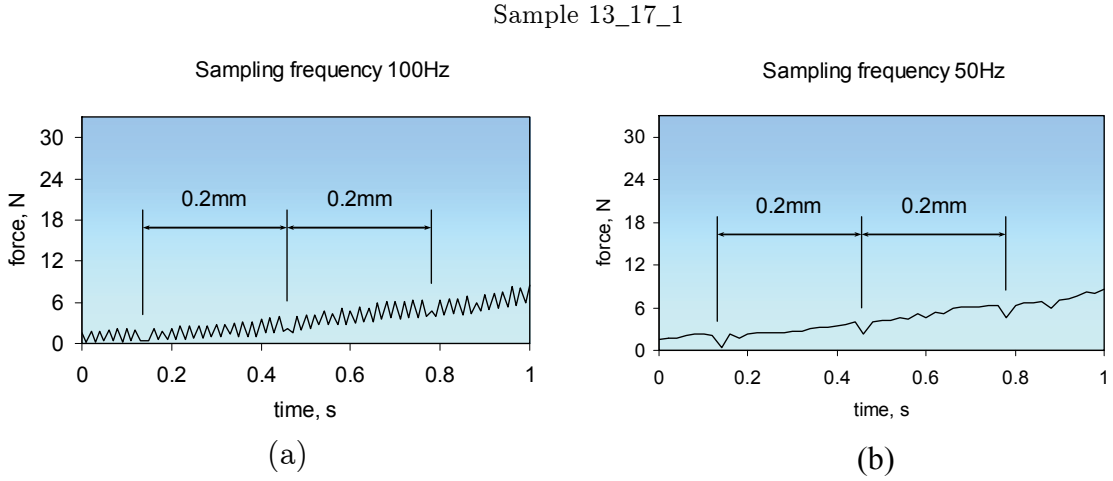

Figure 3.1 - Force versus time at the beginning of deformation (Sample 13_17_1). Effect of sampling frequency: (a) - sampling frequency of 100Hz; (b) - sampling frequency of 50Hz.

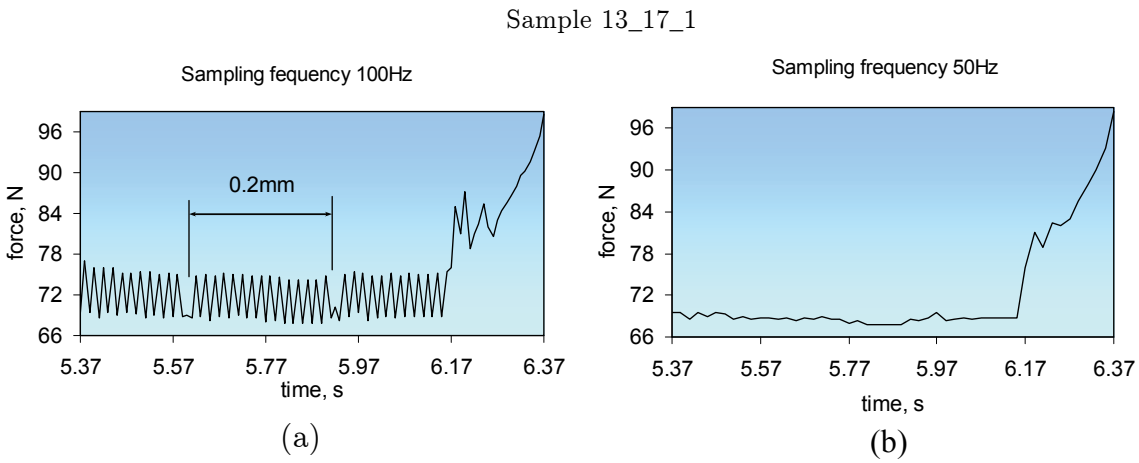

Figure 3.2 - Force versus time, one second prior to failure (Sample 13_17_1). Effect of sampling frequency: (a) - sampling frequency of 100Hz; (b) - sampling frequency of 50Hz.

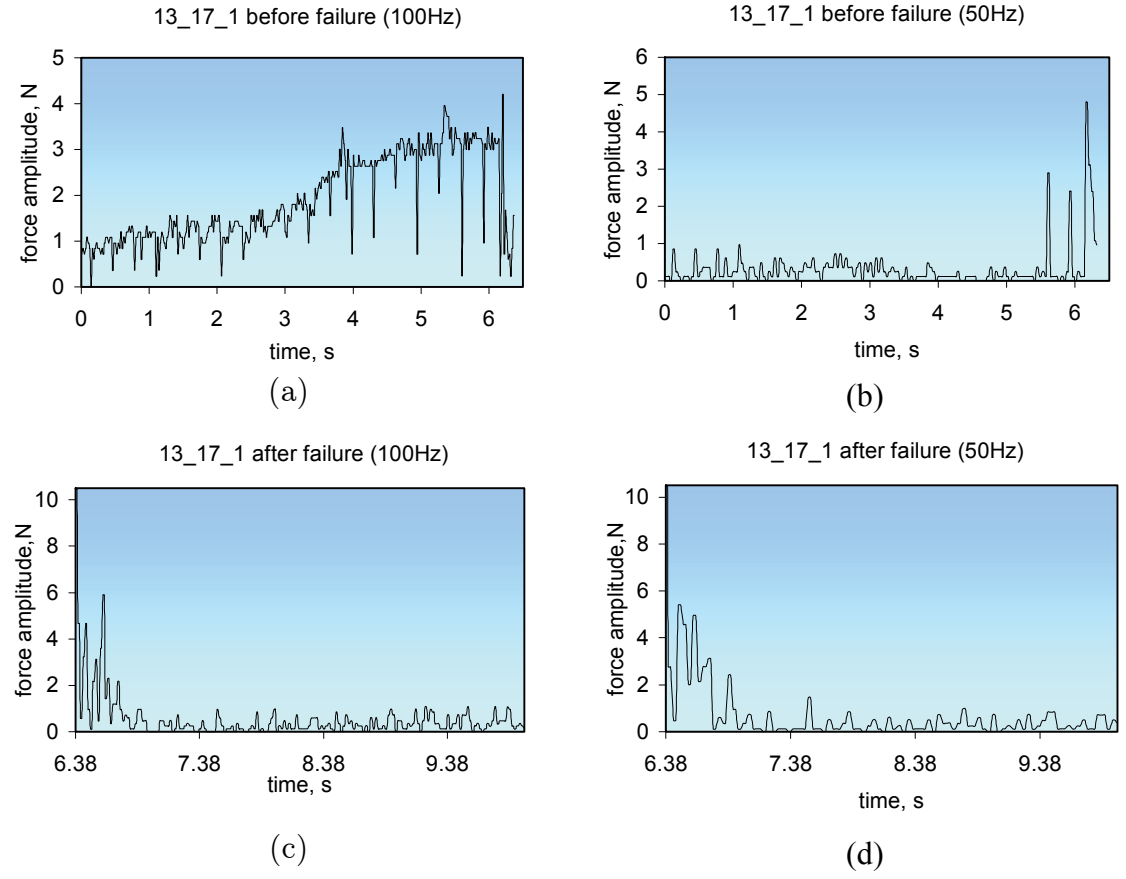

Figure 3.3 - Force amplitude versus time. Effect of sampling frequency (Sample 13_17_1): (a) - Sampling frequency of 100Hz, before the failure; (b) - Sampling frequency of 50 Hz, before the failure; (c) - Sampling frequency of 100Hz, after the failure; (d) - Sampling frequency of 50Hz, after the failure.

From Figures 3.1 to 3.3 a significant influence of the sampling frequency can be seen on the registered force during testing as well as its amplitude. Small force perturbations, corresponding to the horizontal 0.2mm piston displacement in the loading device, can be seen for both sampling frequencies. The reason for such perturbations was not clear. One reason could be related to the to the ice microstructure shown in Figure 1.20 (e.g. grain size in the freeze-bond area or spacing between the air bubbles). For a sampling frequency of 100Hz the force amplitude rose with time and decreased as failure progresses. From the registered force during testing (sampling frequency of 100Hz) every second point was deleted in order to get the values of force amplitude for a sampling frequency of 50Hz. For a sampling frequency of 50Hz the force amplitude was almost constant initially. Subsequently, three characteristic peaks of force amplitude can be seen just before fracture as shown in Figure 3.3b. It is probable that these peaks were related to the crack formation and growth. The highest peak started approximately at 6.2 seconds, which corresponded to the increase in force (see Figure 3.2a,b) and to the increase in the total consumption of energy by the system (Figure 2.19b). The height of the peak can be related to the crack length.

3.2.4 FB development as a function of submersion time and temperature

Earlier Shfrova (2007) showed that FB strength develops with time available for the creation of such a FB (submersion time). It was suggested that freeze-bond strength increases with the submersion time. After some time it reaches its maximum and starts to decrease. General temporal development of the strength is illustrated in Figure 3.4b. For the cold ice with -14°C as its initial temperature, freeze-bonding was already exhibited and was strong after one minute of submerging (Repetto-Llamazares, et al., 2009b). However FB was not observed until one hour of submersion for the warmer ice (with initial temperature of -3°C). Hence, temperature dependence of freeze-bond shear capacity as well as the temperature dependency of any other parameters considered in this analysis should be treated with accuracy.

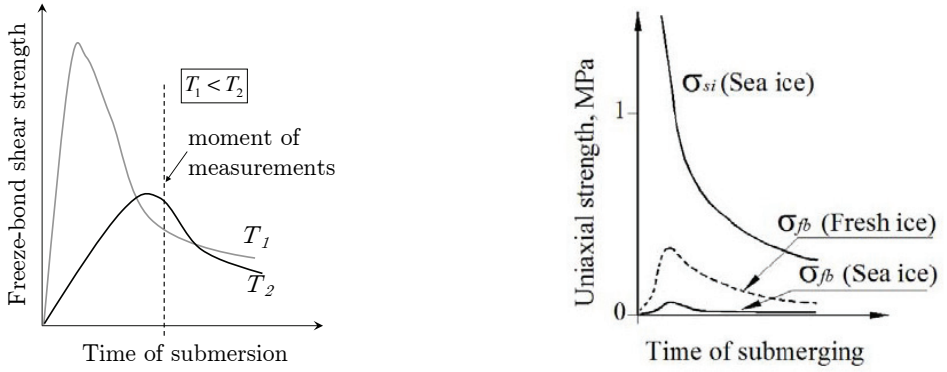

Figure 3.4 - Hypothetic development of freeze-bond strength: (a) - suggested by Prof. K. V. Høyland (personal communication, 2009); (b) - from Shafrova (2007).

If shear capacity of freeze-bonds is a function of time and temperature as given in Figure 3.4a (the relations of uniaxial strength versus submersion time proposed in Figure 3.4b are based on the observations) then, at a fixed submersion time it will be hard to say if, for example, colder ice will exhibit a stronger freeze-bond.

If the hypothesis in Figure 3.4a is correct, its effect on the re-compaction and deformation process of the rubble in the ice-ridge, described in Vershinin, et al. (2005) still remains unclear.

3.2.5 Uncertainties of finite element model

No constitutive model describing the fracture of model ice with air bubbles incorporated into its structure exists. To simplify the model the assumption that ice is an isotropic and homogeneous elastic medium had been made. This assumption is however debatable as (i) it can be seen from the thin section in Figure 1.20 the distribution of air bubbles is not homogeneous along the entire sample thickness (ii) in some registers a nonlinear behavior of force in time can clearly be seen. The material property (elastic modulus of 200MPa) was assumed to be in the range of reported values in Evers and Jochmann (1993). The actual value of E during experiment was unknown. Besides, E can vary from one experiment to another, since the internal structure of the ice is not completely homogeneous (during testing there were samples with higher air content than the other ones) as mentioned in Repetto-Llamazares, et al. (2009b).

In the cohesive model, the TSL shape and the behavior under mixed-mode conditions were assumed in the model. Unless both the experimental uncertainties (i.e. the surface of the ice was uneven and quality of the initial contact surface of the ice blocks was unknown; density, salinity and air content of each sample were not known, etc. as mentioned by Repetto-Llamazares, et al. (2009b)) and the uncertainties of numerical approximation (i.e. constitutive behavior of model ice and properties of tested ice; TSL shape; behavior under mixed-mode loading) are controlled, it will not be possible to judge whether the model or the retrieved cohesive element properties should be rejected or not.

3.3 Model Ice and Freeze-bond Failure Mode

The structure of the model ice (Subsection 1.4.2, Figure 1.20) differs from the structure of natural sea ice. For the natural sea ice the most important parameter in characterizing the substructure is the brine layer spacing or platelet width (Chapter 3 in Loset, et al., 2006). Is the same true for model ice? From Evers and Jochmann (1993) it is known, that higher air content results in weakening of the crystal structure and lowering of ice strength. Such model ice has well scaled mechanical properties like density and E/σ ratio. When the piece of ice as in Figure 1.20 is loaded, stress concentrations around inhomogenities may cause the formation of microcracks. These microcracks may grow and develop into one macrocrack. Under constant load a microcrack can grow after its formation eventually leading to failure which is, by definition, brittle failure. From Figure 1.20 it can be seen that even if the assumption is made that failure occurs along the freeze-bond, the high degree of variability in the

shear strength (for a given experimental procedure) can still be expected due to complex initial conditions along a freeze-bond.

Though the understanding of fracture processes in ice is important for establishing correct ice-ridge structure interaction descriptions, the condition under which the first microcrack appears as well as the criterion for the ductile-brittle transition in ice is under discussion for the natural ice. The same is true for the model ice and therefore there is not enough information at present to discuss the possible effects of model ice microstructure (i.e. grain size, orientation, air content) and the effects due to the presence of freeze-bonds on the ice failure modes. From experiments (Section 1.4) it was not possible to say which conditions provoke brittle or ductile (respectively *failure mode A and B* in Repetto-Llamazares, et al., 2009b) behavior. Besides, a few tested samples were failed in the brittle mode (Table 2.3), which created difficulties during their analysis. It was mentioned by Vershinin, et al. (2005) that the ice blocks in a ridge keel are under high confinement and therefore they might not exhibit a brittle behavior. This study therefore focused on the definition and analysis of ice samples, which exhibit ductile behavior, which was thought to be reasonable.

3.4 Numerical Simulations

The state of stress in three-dimensional model with discretization A (Figure 2.31) might be closer to the existing reality. Neither the boundary conditions, nor the discretization used, nor the effects of nonlinear geometry significantly influenced the reaction force. It was mainly affected by the elastic properties of ice and cohesive element properties. Therefore the numerical model can not model FB shear strength as a function of normal pressure unless other cohesive behavior is specified. In order to improve the model it is possible to define a constitutive response of cohesive element (instead of using traction-separation behavior) assuming, for instance, elastic-plastic FB behavior with a yield function $\Phi = \tau + f(\sigma)$ or introduce a new damage initiation criterion (which depends on a state of compression) into the traction-separation model. As the ice was assumed to be an elastic homogeneous and isotropic medium and only the fracture of cohesive elements was defined, the peak force (Figure 2.30) is a function of cohesive element properties. The size of cohesive elements and therefore their properties depend on the goal of the simulation and the assumptions of the cohesive model. In order to simulate ice fracture process (e.g. speed of the crack growth, stress state along the failure plane) the 'true' values of the fracture energy (or maximum separation), maximum traction together with the sufficient discretization should be used in order to ensure that each of these cohesive elements contains sufficient information about the crack growth in the material.

Table 3.2 summarizes cohesive zone model parameters, which were used for modeling ice fracture process. It is important to note that in Gürtner (2009b) unknown CE properties for HSVA model ice were retrieved by trial and error to match FE solution with experimental results. Gürtner (2009b) writes that the cohesive element properties are true material properties.

Table 3.2 - Fracture properties of ice in assumption of cohesion zone model (CE - cohesive elements; TSL - traction-separation law; χ_1 and χ_2 - separation measures; T_0 - maximum traction; δ_0 - critical separation; Γ_0 - cohesive energy).

Author	Ice	Discretization	Cohesive properties (fracture parameters)			
			TSL	T_0, [kPa]	δ_0, [μm]	Γ_{0N}/ Γ_{0T}, [N/m]
Wang, et al. (2006)	First-year sea ice in McMurdo Sound, Antarctica	?	Bilinear (Figure 1.14b), with separation measure 0.72	130	110	12.7[B]
Gürtner, et al. (2008)	Model HSVA	FE mesh: 20x20mm, 5625 elements in each layer. The total number of CE layers: 2[A].	Trilinear (Figure 1.14c) with separation measures 0.1 and 0.85	71[C]	200[C]	12/19[C]
Gürtner (2009b)	Model HSVA	FE mesh: 50x50mm, ~2500 elements in each layer. The total number of CE layers: 2[A].	Trilinear (Figure 1.14c) with separation measures 0.2 and 0.65	35[C]	70[C]	1.8[D]
Gürtner (2009b)	First-year sea ice	FE discretization: 200x200mm, 2500 elements in each layer. The total number of CE layers: 4[A].	Linear (Figure 1.14a) with normal stiffness 5Gpa/m and tangential stiffness 50Gpa/m	600[C]	?	?
Paavilainen et al. (2009)	?	2D discrete elements 45x45mm tied by the Timoshenko non-linear beam elements	Linear (Figure 1.14a) with stiffness 70MPa	50	725	10-15[F]
This study 3D	Model HSVA	FE discretization: 140x140mm, one element and one CE layer.	Triangular (Figure 1.16) with normal penalty stiffness is equal to tangential penalty stiffness of 2.9MPa	10.5	4248[E]	22.3 /22.3[E]
This study 3D	Model HSVA	FE mesh: 47x47mm, nine CE elements and one CE layer.	Triangular (Figure 1.16) with normal penalty stiffness is equal to tangential penalty stiffness of 2.9MPa	10.5	3810[E]	20 /20[E]

[A]The number of elements and the total number of CE layers were not specified by the author. They were calculated from available information (figures, ice floe dimensions, etc.);
[B]Critical fracture energy (Wang, et al., 2009);
[C]Horizontal cohesive elements (Gürtner, 2009b);
[D] The value was back-calculated from the TSL using Equation 1.20;
[E] The values were limited by the convergence of numerical solution;
[F]The value was based on the personal communication with J. Paavilainen.

Gürtner, et al. (2008) mentioned that the maximum traction may be related to the tensile capacity of the HSVA ice, and cohesive element properties given in Table 3.2 give acceptable results for the in-plane direction. In Wang, et al. (2006) the particular shape of TSL is regarded as a material property. Information presented in Wang, et al. (2006) is obtained through back-calculations such that experimental results match the predicted results, where TSL was assumed to be independent of the rate of separation. In Paavilainen, et al. (2009) ice sheet is modeled with elastic beams and its fracture is modeled according to finite element method by using nonlinear Timoshenko beam elements and a cohesive crack model. Besides the beam elements tied discrete elements together. Hence, such a modeling technique (combined finite-discrete element method) was different from the method used in Gürtner, et al. (2008), Gürtner (2009b) and in this study. It should be noted here that the laws used for coupling of normal and tangential separations as well as the fracture criterion vary among different authors.

In this study the value of the maximum traction (T_0=10.5kPa), from retrieved properties of cohesive element, seems to be physically plausible for representation of freeze-bond tensile strength. The value of the fracture energy (Γ_0=20-22N/m) and therefore value of the critical separation ($\delta_0 \approx 4mm$), corresponding to Γ_0 are high enough to be full-scale material properties. Use of finer FE mesh might help to decrease the Γ_0 value and hence δ_0.

If we assume that the maximum traction specified in the numerical simulations by Gürtner, et al. (2008), Gürtner (2009b) and in this study related to the tensile strength of the model ice and strength of freeze-bonds respectively then the ratio between these strengths was in the order of 0.15-0.3 which corresponds to the laboratory experiments with the arctic sea-ice (for a submerging time up to 60hours) where the ratio between the FB strength and the strength of the ice itself is found to be 0.15 ± 0.15 (Shafrova, 2007).

In the numerical model the actual loading slope was approximated by a linear function. For some of the tested samples (Section 1.4) this assumption might not model all characteristics of loading behavior well. Figure 3.5 shows representative plots of the ductile curves from the experiments of Repetto-Llamazares, et al. (2009b). Figure 3.5 illustrates typical nonlinear behavior of the ice sample plus testing device prior to fracture. Therefore for this sample, the assumption regarding liner behavior prior to fracture is incorrect and retrieved cohesive properties for this sample might not be realistic.

It should be noted that within this study only shear test for only one ice sample was simulated. Therefore, by using the finite element model (Section 1.5) and by tuning

cohesive element properties consequently for the other brittle samples (Section 2.1) it is expected that there will be some variation in the tuned values of maximum tractions due to the presence of high variation in the shear capacity of FB for brittle samples.

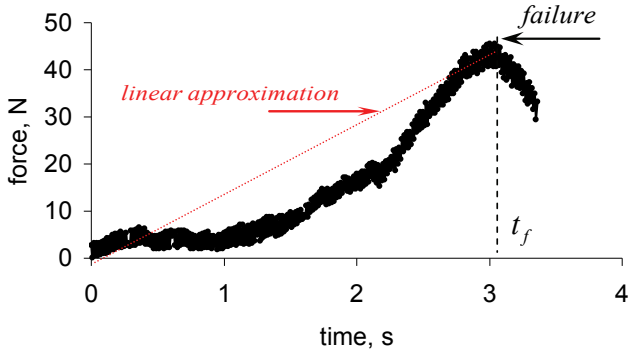

Figure 3.5 - A force measured during freeze-bond shear experiments: Ductile sample 1_13kg_2.

To simulate shear tests for the ductile samples trilinear (trapezoidal) TSL shape (Figure 1.14c) should be used. Unfortunately, the influence of the TSL shape on the results was not investigated in this work as a TSL shape other than that in Figure 1.16 would have to be implemented in the ABAQUS UMAT routine (due to time constraints it hasn't been done in this study).

It can be illustrated by the representative example (Figure 3.5) taken from experimental data that the model described in Section 1.5 needs some improvements to be able take into account nonlinear behavior prior to failure as well as confining pressure dependence. Temperature dependence as well as a constitutive model, describing ice behavior other than linear elastic behavior, can be implemented in the model, where the anisotropy and non-homogeneity of ice can be included. Besides, the anisotropy of freeze-bond can be modeled by specifying different cohesive parameters in different directions, and their behavior under mixed-mode conditions can be formulated in different ways. By combining finite element analysis with random field theory, an investigation can be performed, for instance, on the shear capacity of freeze-bonds with spatially random cohesive properties. As a result of such 'improvements' in the numerical model, the model becomes more complex and hence, more input parameters will be needed. This raises the traditional question of where to get reliable material data.

For the cohesive model in ABAQUS 6.8 it is important to note that the geometrical size of the zone discretized with cohesive elements should be narrow compared to the size of the specimen and interfacial strengths are relatively weak when compared with the adjoining material, as is the case in composite laminates.

3.5 Modeling of Ice-ridge Structure Interactions

With rising human demands the number of techniques for modeling crack growth process in different engineering materials such as metals, concrete, ceramics, etc. are

also continuously rising but there are no guidelines or recommendations on when to use which technique (Gürtner, 2009a).

Though it has been shown by several authors that the cohesive parameters are not material constants in a strict sense (Seigmung and Brocks, 1999) and as mentioned by Paavilainen (2009), that the element length does have an effect on the parameters of the cohesive model (the Young's modulus, tensile strength and critical crack opening displacement are connected to the element length by an inequality, which limits the choice of material parameters and element length), the modeling technique proposed by Gürtner (2009b) and extended by Konuk, et al. (2009a,b) for the ice-ridges seems to be very much in perspective. The positive aspect of the cohesive element framework proposed by Konuk, et al. (2009a) for modeling dynamic interaction of ice-ridges with structure is that the approach can lead to very good results in terms of simulated force and with an increase in computational power it will be possible to take into account a random field theory in the models. With current state-of-the-art knowledge in ice mechanics, to implement such approach several, probably, *phenomenological* but it seemingly *physically plausible* parameters T_0 and Γ_0 of the ice and the freeze-bonds will be needed. These parameters for both ice and freeze-bonds can be found from the experiments. In future the concept in Konuk, et al. (2009a) can be incorporated in large numerical models that can take into account not only temporal and spatial variability of the ice properties. As example, the numerical scheme for predicting ice loads exerted on structures located in ice infested waters was proposed in Appendix E. For this numerical scheme not just statistical data on physical and mechanical properties of ice but also climate data of the area (temperature, wind, etc.) will be needed to compute ice loads.

3.6 Summary

An overview of the problem of ice-ridge structure interactions was done and weak knowledge areas were outlined.

Within the interpretation of the results of freeze-bond shear experiments:

→ An attempt to present obtained results of freeze-bond shear strength from statistical standpoint was done. The log-logistics distribution with mean 2446 and variance $4.6 \cdot 10^6$ well represented the set of freeze-bond shear strength values, expressed in pascals.

→ Ductile samples were separated from brittle ones based on: (i) visual observations of post-peak behavior of loading history, (ii) critical value of unloading slope, (iii) critical value of loading slope. Approach (i) in combination with (ii) was recommended to use in future. Technique (iii) seems to be a weak measure as actual loading slope was varying during experiments.

→ Several types of load oscillations were noted ('saw (1)', 'saw (2)', 'saw (3)', 'line' and 'mix'). Observed oscillations were related to the effect of sampling

frequency and the model ice structure. In most of the measurements, the frequency of measured load oscillation was equal to the sampling frequency of 100Hz.

→ Post-peak force behavior was analyzed for total 58 test runs. For all tests the values of measured force at the end of the first second after failure converged to values between 8-30N depending on the normal load and submersion time. The load value at the end of the first second after failure did not show significant variation in brittle or ductile samples.

→ The area under the loading curve prior to the load-peak (between the starting of the failure and the peak force) was calculated an analyzed for all the samples. An attempt to correlate the obtained values of the area to the fracture energy of ice was done. The area under the loading curve was proportional to the total input of energy to the system but further assumptions were needed to discuss the fracture energy of ice.

→ Analysis of frictional behavior was done, similar to the study in Maeno, et al. (2003). Obtained trends were compared with earlier results on ice-ice frictional behavior. Estimated frictional behavior of ice after the failure of the freeze-bond agreed with observations in Fort (2003), Maeno, et al. (2003), Frederking and Barker (2002) and Nanetti, et al. (2008).

Within the task of numerical simulations of the freeze-bond shear tests:

→ A finite element model for the simulation of freeze-bond shear test was built in ABAQUS 6.8. Cohesive element properties were retrieved by trial and error to match finite-element solutions with experimental results. Tuned maximum traction was found to be 10.5kPa, penalty stiffness of 2.9MPa, fracture energy of 22.3N/m.

→ Effects of problem dimensionality, modeling technique (surface-based modeling versus cohesive zone model) and boundary conditions as well as influence of finite element mesh were studied.

→ Factorial design of numerical simulation was used in order to study effects of variables (maximum traction, elasticity modulus of ice and cohesive-element penalty stiffness) together with their interaction effects, where two or more variables act together.

→ Retrieved cohesive element properties were compared with parameters used in earlier studies and some possible improvements for the model were suggested.

CONCLUSIONS and RECOMMENDATIONS for FUTURE WORK

4

4.1 Conclusions

In the state-of-the-art knowledge of ice-ridge structure interaction:

- → there are no common techniques for estimation of loads exerted by an ice-ridge on a structure;
- → existed calculation algorithms require initial data which is difficult to define in practice;
- → there is a lack of full-scale data available for research;
- → almost no numerical tools are available for modeling ice-ridges;
- → there is a lack of laboratory or full-scale tests, available for validation numerical models.

Besides, the existence of freeze-bonds in the ice-ridge might significantly affect ice-ridge failure process and therefore the load exerted onto a structure by an ice-ridge; there are almost no analytical, numerical or empirical models, which directly take into account the phenomenon of freeze-bonding.

This study showed that from the conducted experiments intended to study freeze-bond strength in model ice it is also possible to study ice fracture processes as well as post-failure behavior.

The major findings of this study were:

- → The shear capacity of freeze-bonds as well as the post-peak force and the total input of energy to the system prior to failure have similar trends. They increase with increase of normal load and decrease with submersion time.

- → For the experiments with low initial ice temperatures a linear dependency can be assumed between the shear capacity of freeze-bonds and the normal load as well as between the post-peak force and the normal load.

- → The force measured after one second since the peak force was reached represents the frictional force between two ice blocks. Estimated frictional behavior agrees with observations in Fort (2003), Maeno, et al. (2003), Frederking and Barker (2002) and Nanetti, et al. (2008).

→ The fracture energy for freeze-bonds can not be extracted directly from measurements without further assumptions.

→ There is a correlation between the area under the curve prior to failure and the force measured after one second since the peak force was reached.

→ By improving the experimental procedure as described in Repetto-Llamazares, et al. (2009b) it will be possible to study not only FB process but also the frictional behavior after fracture. By video monitoring of the crack initiation and growth it will be possible to study fracture process inside the freeze-bond.

→ The peak load is completely determined by the maximum traction strength and the initial part of TSL. Retrieved material parameters of freeze-bond for cohesive zone model (maximum traction of 10.5kPa, corresponding to the tensile strength of freeze-bond), seem to be physically plausible and a ratio between the freeze-bond tensile strength (found in this study) and the tensile strength of ice (Gürtner, 2009b) coincides with observations in Shafrova (2007).

→ Capabilities of ABAQUS 6.8 are sufficient for modeling brittle fracture of ice. A good constitutive model of HSVA ice is needed in order to verify obtained properties of freeze-bond.

→ In order to use physically plausible material properties for cohesive zone model sufficient discretization of the cohesive zone has to be made. Despite the same results, modeling of the given problem using a cohesive zone model is preferable to modeling with a surface-based approach in terms of specified parameters of the model.

→ Method proposed by Konuk, et al. (2009a) for the modeling of ice-ridges seems to be very much in perspective but in order to implement it, additional investigations, concentrating on both ice and freeze-bond behavior under mixed-mode loading at different temperatures, are needed.

4.1 Recommendations for Future Work

The analyses discussed in this work demonstrate both the difficulties encountered in interpreting and explaining experimental results and the difficulties encountered in numerical modeling of the experiments. In view of the urgent need for better information on the material properties of the model ice and freeze-bonds, the author recommends that:

→ studies be conducted to better understanding freeze-bonging process in both model and natural sea ice to compare the difference in the fracture behavior of different microstructures of ice.

→ laboratories provide data on fracture properties of tested ice, and carry out studies on the behavior of model ice under mixed-mode loading conditions.

In view of the significant variability in the freeze-bond shear strength over ice samples (the test parameters being the same) and due to unexplainable difference in the failure behavior of model ice (ductile/brittle), it is also considered important to put greater emphasis on the experimental setup for evaluation of freeze-bond shear strength.

Better analysis essentially depends on the improvement made in the planning of the experiment and obtaining of better statistics of freeze-bond shear capacity of model ice for each of two different failure modes (brittle/ductile). Considering the discrepancies observed in values of freeze-bond shear strength measured by different authors, the author recommends that:

→ different scientists actively participate in investigations and possibly on standardization of methods for measuring strength of freeze-bonds.

In addition to continuation of freeze-bond strength studies combined with the numerical modeling of the experiments, it might be recommended that:

→ consideration be given to improvements of existing analytical and numerical models, for calculation of loads for scenario of ice-ridges interactions with structures.

In view of the importance of variation in environmental conditions for the load exerted on structure from an ice-ridge, the author further recommends:

→ that studies on the approaches, combining thermodynamics and mechanics of ice, for estimation of ice loads on structures should be continued.

Finally, the difficulties of carrying out analysis of the experiments in presence of high dispersion in the result values were noted, and therefore strongly recommended that:

→ future experiments with ice should have enough statistical output in order to comply with the requisites of probabilistic methods.

REFERENCES

ABAQUS Documentation for Version 6.8.

Antony, J. (2003). *Design of Experiments for Engineers and Scientists*. Butterworth-Heinemann, Oxford, 152p.

Anvari, M. (2008). *Simulation of Dynamic Fracture in Aluminum Structures*. Norwegian University of Science and Technology, Department of Engineering Design and Materials. Doctoral thesis, 99p.

Barrenblatt, G.I. (1962). The Mathematical Theory of Equilibrium Crack in the Brittle Fracture. *Advances in Applied Mechanics*, Vol. 7, pp. 55-125.

Beaty, W.J., "*Recurring Science Misconceptions in K-6 Textbooks*", 2009-APR-30
<http://amasci.com/miscon/miscon4.html#fric>

Belov, R.M. (2004). *Finite Element Modeling and Investigation of Symmetric Rolling*. St. Petersburg: Saint Petersburg State Polytechnic University, Department of Mechanical Engineering and Control. Master thesis, 126p. (in Russian).

Belytschko, T., Liu, W.K. and Moran, B. (2006). *Nonlinear Finite Elements for Continua and Structures*. WILEY, 650p.

Blackerby, J. (2006). *Numerical Simulation of Dynamic Ice Forces on Offshore Structures*. Clarkson University NSF REU: Marine Science and Engineering in China. Report, 13p.

Brady, J., "*Icebreakers*", Virtual Finland, 2009-MAY-05,
<http://finland.fi/netcomm/news/showarticle.asp?intNWSAID=25894&LAN=ENG>

Bruun, P.K. and Gudmestad, O.T. (2006). A Comparison of Ice Loads from Level Ice and Ice Ridges on Sloping Offshore Structures Calculated in Accordance with Different International and National Standards. *Proceedings of 25th International Conference on Offshore Mechanics and Arctic Engineering*, OMAE2006-92007.

Camanho, P.P.and Davila, C.G. (2002). *Mixed-mode Decohesion Finite Elements for the Simulation of Delamination in Composite Materials*. NASA/TM-2002-211737.

Chehayeb, F.S., Connor, J.J. and Sunder, S.S. (1986). Numerical Modeling of Ice-Structure Interaction. *Proceedings of Ice Technology Conference*. Massachusetts Institute of Technology, Cambridge, Massachusetts, pp. 431-444.

Collins, M. and Amos, C. (2008). *Applied Sediment Dynamics*. SOES 3014/6011. Lecture Notes.

Derraji-Aouat, A. and Lau, M. (2005). Ice Loads on Power Generating Stations in the Bell Isle Straight. *Proceedings of the 18th International Conference on Port and Ocean Emgineering Under Arctic Conditions*, Vol. 1, pp. 387-398.

Duff, I.S. and Reid, J.K. (1983). The Multifrontal Solution of Indefinite Sparse Symmetric Linear Equations. *ACM Transactions on Mathematical Software*, Vol. 9, pp. 302-325.

Dugdale, D.S. (1960). Yielding of Steel Sheets Containing Slits. *Journal of the Mechanics and Physics of Solids*, Vol. 8, pp. 100-104.

Eckard, C.W., "*Advantages and Disadvantages of FEM Analysis in an Early State of the Design Process*", 2009-MAY-05,
<http://www.mscsoftware.com/support/library/conf/auto00/p06400.pdf>

Ettema, R. and Shaefer, J.A. (1986). Experiments on Freeze-Bonding Between Ice Blocks in Floating Ice Rubble. *Journal of Glaciology*, Vol. 32, pp. 397-403.

Ettema, R. and Urroz, G.E. (1989). On Internal Friction and Cohesion in Unconsolidated Ice Rubble. *Cold Regions Science and Technology*, Vol. 16, pp. 237-247.

Evers, K.U. and Jochsmann, P. (1993). An Advanced Technique to Improve the Mechanical Properties of Model Ice Developed at the HSVA Ice Tank. *Proceedings of the 12th International Conference on Port and Ocean Engineering under Arctic Conditions*, pp. 877-888.

Falk, M., Needleman, A. and Rice J.R. (2001). A Critical Evaluation of Cohesive Zone Models of Dynamic Fracture. *Journal de Physique IV*, Vol. 11, pp. 43-50.

Feih, S. (2005). *Development of a User Element in ABAQUS for Modelling of Cohesive Laws in Composite Structures*. Technical report, Risø-R-1501, 52p.

Fialko, S.Y. (2003). The Nested Substructures Method for Solving Large Finite-element Systems as Applied to the Thin-walled Shells with High Ribs. *International Applied Mechanics,* Vol. 39, No. 3, pp. 324-331.

Fortt, A., Schulson, E.M. and Russell, E. (2003) Sliding along Coulombic Shear Faults in Ice. *Canadian Journal of Physics*, Vol. 81, pp. 519-529.

Frederking, R. and Barker, A. (2002). Friction of Sea Ice on Various Construction Materials. *Proceedings of 16th IAHR International Symposium on Ice*, Vol. 1, pp. 442-450.

Gudmestad, O.T., Løset, S., Alhimenko, A.I., Shkhinek, K.N., Tørum, A. and Jensen, A. (2007). *Engineering Aspects Related to Arctic Offshore Developments*. St. Petersburg, 255p.

Gürtner, A. (2009a). "*State of the Art Methods in Simulating Crack Propagation in Solids with the Finite Element Method.*" Trial lecture on 25.02.09. Norwegian University of Science and Technology, Trondheim.

Gürtner, A. (2009b). *Experimental and Numerical Investigations of Ice-Structure Interaction*. Norwegian University of Science and Technology, Department of Civil and Transport Engineering. Doctoral thesis, 182p.

Gürtner, A., Konuk, I., Gudmestad, O.T. and Liferov, P. (2008). Innovative Ice Protection for Shallow Water Drilling Part III – Finite Element Modelling of Ice Rubble Accumulation. *Proceedings of 27th International Conference on Offshore Mechanics and Arctic Engineering*, OMAE2008-57915.

Harris, C.O. (1959). *Introduction to Stress Analysis*. MacMillan, New York, 330p.

Heinonen, J. (2004). *Constitutive Modeling of Ice Rubble in First-Year Ridge Keel.* Helsinki University of Technology, Espo. Doctoral thesis, 142p.

Heinonen, J. (1999). Simulating Ridge Keel Failure by Finite Element Method. *Proceedings of the 15th International Conference on Port and Ocean Engineering under Arctic Conditions*, Vol. 3, pp. 956-963.

Heinonen, J. and Määttänen, M. (2001). Full-Scale Testing of Ridge Keel Mechanical Properties in LOEIF-Project. *Proceedings of the 16th International Conference on Port and Ocean Engineering under Arctic Conditions*, Vol. 2, pp. 1435-1444.

Hilber, H.M., Hughes, T.J.R. and Taylor, R.L. (1978). Collocation, Dissipation and 'Overshoot' for Time Integration Schemes in Structural Dynamics. *Earthquake Engineering and Structural Dynamics*, Vol. 6, pp. 99-117.

Hillerborg, A., Modeer, M. and Petersson, P.E. (1976) Analysis of Crack Formation and Crack Growth in Concrete by Means of Fracture Mechanics and Finite Elements. *Cement and Concrete Research*, Vol. 6, pp. 773-782.

Horrigmoe, G., Zeng, L.F, and Andersn, R. (1994). Modelling Ductile Bahaviour of Columnar Ice Using Computational Plasticity. *Proceedings of the 12th IAHR International Symposium on Ice*, Vol. 1, pp. 282-291.

Irons, B. (1970). A frontal solution of program for finite element analysis. *International Journal for Numerical Methods in Engineering*, Vol. 2, pp. 5–32.

Jefferies, M.G., Kärnä, T. and Løset, S. (2008). Field Fata on the Magnification of Ice Loads on Vertical Structures. *Proceedings of the 19th IAHR International Symposium on Ice*, Vol. 2, pp. 1115-1134.

Johannessen, O.M., Alexandrov, V.Y., Frolov, I.Y., Sandven, S., Pettersson, L.H., Bobylev, L.P., Kloster, K., Smirnov, V.G., Mironov, Y.U. and Babich, N.G. (2006). *Remote Sensing of Sea Ice in the Northern Sea Route: Studies and Applications*. Springer Berlin Heidelberg, 544p.

"*Jäänmurtajien historia*," Wikipedia, Wikimedia Foundation, Inc., 2009-APR-30, <http://fi.wikipedia.org/wiki/Jäänmurtajien_historia> (In Finish)

Kato, M., Iijima, Y., Arakawa, M., Okimura, Y., Fujimura, A., Maeno, N. and Mizutani, H. (1995). Ice-on-Ice Impact Experiments. *Icarus*, Vol. 113, pp. 423-441.

Kim, J.H., Lee, C.S. and Kim, S.J. (2005). High-performance Domain-wise Parallel Direct Solver for Large-scale Structural Analysis. *AIAA Journal*, Vol. 43, pp. 662-670.

King, S.M., "*Simulation Using ABAQUS Explicit of Quasi-static Process Involving Complex contact that Occur in Supertension Cable Engineering*", 2009-MAY-21, < http://www.isheu.com/data_489_1.aspx >

Konuk, I., Gürtner, A., and Yu, S., (2009a) A Cohesive Element Framework for Dynamic Ice-Structure Interaction Problems – Part I: Review and Formulation, Submitted to the *28th International Conference on Ocean, Offshore and Arctic Engineering*, Honolulu, OMAE2009-7926.

Konuk, I., Gürtner, A., and Yu, S., (2009b) A Cohesive Element Framework for Dynamic Ice-Structure Interaction Problems – Part II: Implementation. Submitted to the *28th International Conference on Ocean, Offshore and Arctic Engineering*, Honolulu, OMAE2009-802502.

Kwon, K.E., Cho, S.W., Choi, Y. and Lee, G.B. (2003). Application of Multi-Frontal Method in Collaborative Engineering Environment. *International Journal of CAD/CAM*, Vol. 3, pp. 51-60.

Liferov, P. (2005). Review of Ice Rubble Behaviour and Strength, Part II: Modelling. *Cold Regions Science and Technology*, Vol. 41, pp. 153-163.

Liferov, P. and Bonnemaire, B. (2005). Review of Ice Rubble Behaviour and Strength, Part I: Testing and Interpretation of the Results. *Cold Regions Science and Technology*, Vol. 41, pp. 135-151.

Liferov, P. Jensen, A. and Høyland, K.V. (2003). 3D Finite Element Analysis of Laboratory Punch Tests on Ice Rubble. *Proceedings of the 17th International Conference on Port and Ocean Engineering under Arctic Conditions*, Vol. 2, pp. 599-610.

Lin, G., Cornec, A. and Schwalbe, K.H. (1998). Three-dimensional Finite Element Simulation of Crack Extension in Aluminum alloy 2024FC. *Fatigue and Fracture of Engineering Materials and Structures*, Vol. 21, pp.1159-1173.

"*Linear elasticity*," Wikipedia, Wikimedia Foundation, Inc., 2009-MAY-04, <http://en.wikipedia.org/wiki/Linear elasticity>

Lishman, B., Sammonds, P. Feltham, D. and Wilchinsky, A. (2009) The Rate- and State- Dependence of Sea Ice Friction. Submitted to the *20th International Conference on Port and Ocean Engineering under Arctic Conditions*, Luleå.

Lundquist, E. "*Arctic sea routes opening up with climate change*", People & the Planet website, 2009-MAY-11, < http://www.peopleandplanet.net/doc.php?id=3383>

Løset, S. (1994a). Discrete Element Modeling of a Broken Ice Field- Part I: Model Development. *Cold Regions Science and Technology*, Vol. 22, pp. 339-347.

Løset, S. (1994b). Discrete Element Modeling of a Broken Ice Field- Part II: Simulation of Ice Loads on a Boom, *Cold Regions Science and Technology*, Vol. 22, pp. 349-360.

Løset, S., Shkhinek, K.N., Gudmestad, O.T. and Høyland, K.V. (2006). *Actions from Ice on Arctic Offshore and Coastal Structures*. St. Petersburg, 271p.

Määttänen, M. and Lija, V.P. (2005). *Comparison of Existing Ice Load Design Recommendations*. Background for ISO 19906 Arctic Offshore Structures Standard EU-project STANDICE TREN/04/FP6EN/S07.31041/503721, 52p.

Macal, M. C. (2005). "*Model Verification and Validation*". Workshop on Threat Anticipation: Social Science Methods and Models, The University of Chicago and Argonne National Laboratory.

Maeno, N., Arakawa, M., Yasutome, A., Mizukami, N. and Kanazawa, S. (2003) Ice-Ice Friction Measurements, and Water Lubrication and Adhesion-Shear Mechanisms. *Canadian Journal of Physics*, Vol. 81, pp. 241-249.

"*Making Waves*", Oceanic Consulting Corporation, 2009-MAY-12 <http://www.oceaniccorp.com/pdfs/FALL2003.pdf>

Martonen, P. (2003). *Ice Ridge Load Simulations Based on a Multi Surface Failure Criterion Using the Finite Element Method.* Helsinky University of Technology, Espo. Master thesis.

Masterson, D.M. and Frederking, R. (2006). Experience with the Canadian Standards Association Offshore Structures Code. *Proceedings of the 16th International Offshore and Polar Engineering Conference*, Vol. 1, pp. 14-20.

MATLAB version 7.1.0.246 (R14) Service Pack 3, The MathWorks, Inc., (2005).

McKenna, R.F., Spencer, D., Lau, M., Walker, D. and Crocker, G.B., (1997). Modelling the Forces Exerted by Pack Ice Consisting of Small Floes. *Proceedings of the 16th International Conference on Offshore Mechanics and Arctic Engineering/14th International Conference in Port and Ocean Engineering Under Arctic Conditions,* Vol. 4, pp. 329-338.

Moslet, P.O. (2008). Medium Scale Ice-Structure Interaction. *Cold Regions Science and Technology*, Vol. 54, pp. 143-152.

Nanetti, M., Marchenko, A. and Høyland, K.V., (2008). Experimental Study on Friction between Saline Ice and Steel. *Proceedings of the 19th IAHR International Symposium on Ice*, Vol. 1, pp. 921-936.

Needleman, A. (1987). A Continuum Model for Void Nucleation by Inclusion Debonding. *Journal of Applied Mechanics*, Vol. 54, pp. 525-531.

Needleman, A. (1990). An Analysis of Decohesion along an Imperfect Interface, *International Journal of Fracture*, Vol. 42, pp. 21-40.

Nevel, D. (2001). First Year Ice Ridge Acting on Conical Structure-Pressure Ridge Interaction. *Proceedings of the 16th International Conference on Port and Ocean Engineering under Arctic Condition*, Vol. 1, pp. 369-374.

Paavilainen, J., Tuhkuri, J. and Polojärvi, A. (2009). Simulations of Ice Pile-up Process with 2D Combined Finite-Discrete Element. Submitted to *20th International Conference on Port and Ocean Engineering under Arctic Conditions*, Luleå.

"*Pilot (Icebreaker)*," Wikipedia, Wikimedia Foundation, Inc., 2009-APR-30, <http://en.wikipedia.org/wiki/Pilot (icebreaker)>

Repetto-Llamazares, A.H.V., Høyland, K.V., Serré, N., Evers, K.U., Jochman P. and Liferov, P. (2009a). Model Testing of Ice Ridge Loads on Structures Part II: Ridge Building and Physical Properties. Submitted to the *20th International Conference on Port and Ocean Engineering under Arctic Conditions*, Luleå.

Repetto-Llamazares, A.H.V., Jochman, P., Evers K.U. and Høyland, K.V. (2009b). Model Testing of Ice Ridge Loads on Structures Part IV: Preliminary Results of Freeze Bond Shear Strength Experiments. Submitted to the *20th International Conference on Port and Ocean Engineering under Arctic Conditions*. Luleå.

Sand, B. and Horrigmoe, G. (1998). Simulations of Ice Ridge Forces on Sloping Structures. *Proceedings of the 8th ISOPE Conference*, Vol. 2, pp. 476-482.

Sand, B. and Horrigmoe G. (2001). Simulations of Ice Ridge Forces on Conical Structures. *Proceedings of the 11th ISOPE Conference*, Vol. 1, pp. 754-760.

Sand, B. and Fransson, L. (2006). Nonlinear Finite Element Simulations of Ice Sheet Forces on Conical Structure. *Proceedings of 25th International Conference on Ocean, Offshore and Arctic Engineering*, OMAE2006-92520.

Scheider, I. (2001). *Cohesive Model for Crack Propagation Analyses of Structures with Elastic-Plastic Material Behavior. Foundations and Implementation*, Technical report, GKSS, department WMS, 39p.

Scheider, I. and Brocks, W. (2003a). Simulation of Cup-cone Fracture Using the Cohesive Model. *Engineering Fracture Mechanics*, Vol. 70, pp. 1943-1961.

Scheider, I. and Brocks, W. (2003b). The Effect of the Traction Separation Law on the Results of Cohesive Zone Crack Propagation Analyses. *Key Engineering Materials*, Vol. 251, pp. 313-318.

Schmitz, T.L., Action, J., Ziegert, J.C., Sawyer, W.G. "*Dynamic Friction Coefficient Measurements: Device and Uncertainty Analysis*". University of Florida, Department of Mechanical and Aerospace Engineering, 2009-MAY-08, <http://highspeedmachining.mae.ufl.edu/htmlsite/presentations/dr_schmitz/aspe_04_friction_present.pdf>

Shafrova, S. (2007). *First-Year Sea Ice Features: Investigation of Ice Field Strength Heterogeneity and Modelling of Ice Rubble Behaviour*. Norwegian University of Science and Technology. Doctoral thesis. 170p.

Shafrova, S., Liferov, P. and Shkhinek, K.N. (2004). Modelling Ice Rubble with a Pseudo-Discrete Continuum Model. *Proceedings of the 17th IAHR International Symposium on Ice,* Vol. 2, pp. 265-273.

Shapiro, N.M. and Ritzwoller, M.H. (2004). Inferring Surface Heat Flux Distributions Guided by a Global Seismic Model: Particular Application to Antarctica. *Earth and Planetary Science Letters.* Vol. 223, pp. 213-224.

Shkhinek, K., Blanchet, D., Jilenkov, A. and Shafrova, S. (2007). Ice Loads Dependence on the Field Heterogeneity. *Proceedings of the 19th International Conference on Port and Ocean Engineering under Arctic conditions*, pp. 245-255.

Siegmung, T. and Brocks W., (1999). Prediction of the Work of Separation and the Implications to Modeling. *International Journal of Fracture*, Vol. 99, pp. 97-116.

Siegmund, T. and Needleman, A. (1997). A Numerical Study of Dynamic Crack Growth in Elastic-viscoplastic Solids. *International Journal of Solids and Structures*, Vol. 34, pp.769-787.

Sinha, N.K. (1979). Grain Boundary Sliding in Polycrystalline Materials. *Philosophical Magazine*, Vol. 40, pp. 825-842.

Sinha, N.K. (1982). Delayed Elastic Strain Criterion for First Cracks in Ice. *Proceedings of the IUTAM Conference on Deformation and Failure of Granular Materials*, pp. 323-330.

Suhanovsky, A. and Slobodyanyuk, I. (2007). *Arctic Russia. ROSHYDROMET in High Latitudes*. SK-Russia, 307p. (in Russian).

Sukhorukov, S. and Marchenko, A. (2009). Stick Slip Interaction of Ice with Steel Surfaces. Submitted to the *20th International Conference on Port and Ocean Engineering under Arctic Conditions*, Luleå.

Surkov, G.A. and Truskov, P.A. (1993). Method for Evaluation of the First-Year Ice Hummock Strength. *Proceedings of the 3rd International Offshore and Polar Engineering Conference*, Vol. 2, pp. 640-642.

Surkov, G.A., Astaf'yev, V.N., Polomoshnov, A.M., Zemlyuk, S.V. and Truskov, P.A. (2001). Strength Characteristics of Hummock Formations. *Proceedings of the 11th International Offshore and Polar Engineering Conference*, Vol. 1, pp. 770-774.

Szabó, B. (2007). "On the Calibration and Validation of Mathematical Models", ESRD, 2009-MAY-21,
<http://www.esrd.com/docs/Technical%20Briefs/pFEM˙Validation.pdf >

Timco, G.W., Croasdale, K. and Wright B. (2000). *An Overview of First-Year Ice Ridges*. Technical report HYD-TR-47, Canada, 157p.

Timco, G.W. and Croasdale, K.R. (2006). How Well Can We Predict Ice Loads. *Proceedings of the 18th IAHR International Symposium on Ice*, Vol. 1, pp.167-174,

Timco, G.W., Frederking, R., Kamesaki, K. and Tada, H. (1999a). Comparison of Ice Load Calculation Algorithms for First-Year Ridges. *Proceedings International Workshop on Rational Evaluation of Ice Forces on Structures*, pp. 88-102.

Timco, G.W., Wright, B., Johnston, M. and Frederking, R. (1999b). First Year Ice Ridge Loads on Molikpaq. *Proceedings of RAO'99 Conference*, pp. 172-179.

Toikka, M. and Hallikainen, M. (1992). Radar Backscatter Signatures of Baltic Sea Ice. *Proceedings of the IGARSS'92 conference*, Vol. 2, pp. 1527-1529.

Trumars, J. (2009). The Factorial Design Method in Design of Experiments and Interpretation of Results. Submitted to *the 28th International Conference on Ocean, Offshore and Arctic Engineering*, Honolulu, OMAE2009-79316.

Tvergaard, V. and Hutchinson, J.W. (1992). The Relation between Crack Growth Resistance and Fracture Process Parameters in Elastic-plastic Solids. *Journal of the Mechanics and Physics of Solids*, Vol. 40, pp. 1377-1397.

Tvergaard, V. (1990a). Effect of Fibre Debonding in a Whisker-Reinforced Metal. *Materials Science and Engineering*, Vol. 125, pp. 203-213.

Tvergaard, V. (1990b). Material Failure by Void Growth to Coalescence. *Advances in Applied Mechanics*, Vol. 27, pp. 83-151.

Varstad, P. (1983). *On the Mechanics of the Ice Loads on Ships in Level Ice in the Baltic Sea*. VTT – Technical Research Centre of Finland, Ship Laboratory Publication 11, Doctoral thesis, 91p.

Vershinin, A.S., Truskov, P.A. and Kuzmichev, K.V. (2005). *Ice Actions on the Structures of the Sakhalin Shelf*, Institute Giprostroimost, Moscow, 208 p. (in Russian).

Vershinin, S.A., Truskov, P.A. and Liferov, P.A. (2008). *Ice Action on Seabed and Subsea Structures*. IPK, Moscow. 220 p.

Wang, M.Z. (2000). A Method for Calculation of Ridge Crack Loads on a multifaceted Conical Structure. *Proceedings of the 10th ISOPE Conference*, Vol. 1, pp. 633-639.

Wang, S., Dempsey, J.P., and Cole, D.M. (2006). In-Situ Fracture of First-Year Sea Ice on McMURDO SOUND: TEST A2-SP8. *Proceedings of 18th International Conference on Port and Ocean Engineering Under Arctic Conditions*, Vol. 3, pp. 1071-1082.

Wright, B. and Timco, G.W. (1994). A Review of Ice Forces and Failure Models on the Molikpaq. *Proceedings of the 12th International Association for Hydraulic Research Ice Symposium*, Vol. 2, pp. 816-825.

Yu, B., Wu, W., Xu, N., Yue, Q. and Liu, S. (2007). Numerical Simulation of Dynamic Ice Forces on Conical Structures. *Proceedings of the 19th International Conference on Port and Ocean Engineering Under Arctic Conditions*, Vol. 1, pp. 277-285.

Yue, J. J., "*Energy Concepts for Fracture*", 2009-MAY-11, <http://www.sv.vt.edu/classes/MSE2094_NoteBook/97ClassProj/anal/yue/energy.html>

Zhang, X., Mai, Y.W. and Jeffrey, R.G. (2003). A Cohesive Plastic and Damage Zone Model for Dynamic Crack Growth in Rate-dependent Materials. *International Journal of Solids and Structures*, Vol. 40, pp. 5819-5837.

Zienkiewicz, O.C., Taylor, R.L. and Zhu, J.Z. (2005). *The Finite Element Method: Its Basis and Fundamentals*. Butterworth-Heinemann, 752p.

Zufelt, J.E. and Ettema, R. (1996). *Model ice properties*. U.S. Army Cold Regions Research and Engineering Laboratory, Hanover, New Hampshire, CRREL Report 96-1, 19p.

APPENDIX A

A - History of the Freeze-Bond Experimental Setup

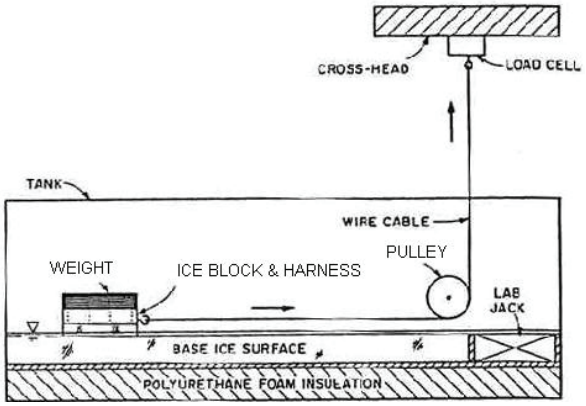

Experimental setup (Ettema and Shaefer, 1986)

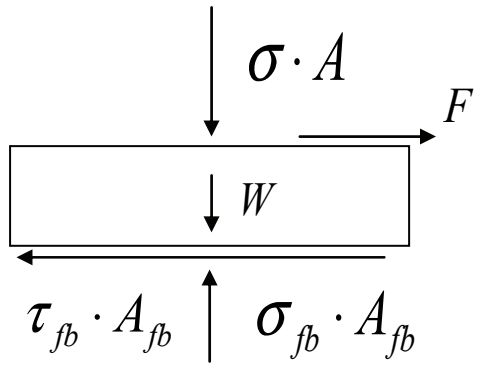

A scheme of loads, acting on the tested ice sample.

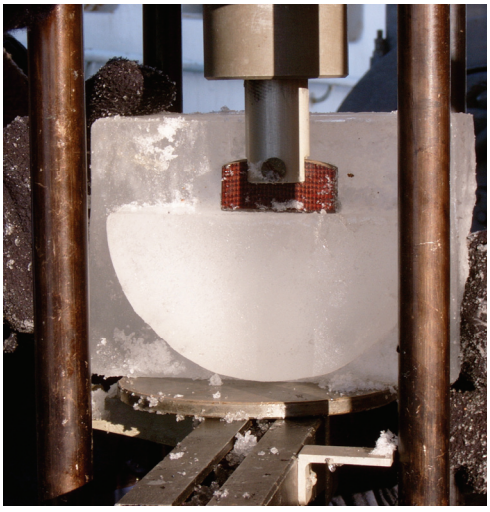

Experimental setup (Prof. A. Marchenko, personal communication, 2006)

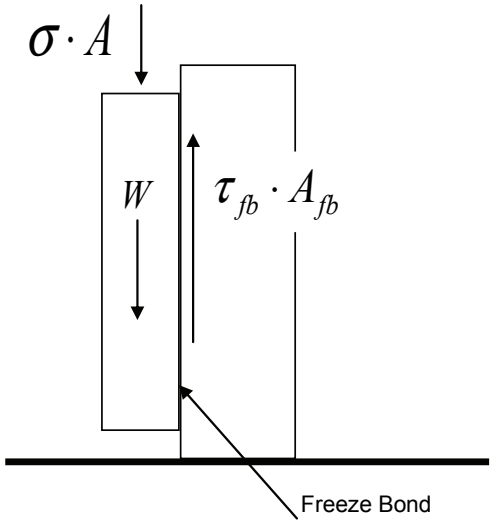

A scheme of loads, acting on the semicircular ice sample (side view).

History of the Freeze-Bond Experimental Setup
(continuation)

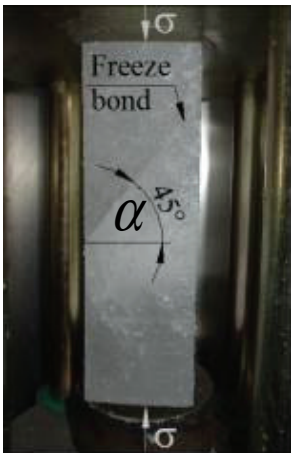

Experimental setup (Shafrova, 2007)

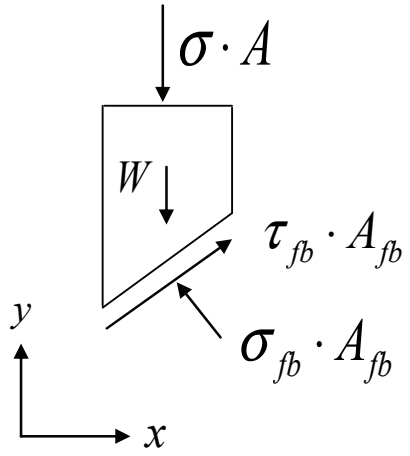

A scheme of loads, acting on the upper piece of the tested ice sample.

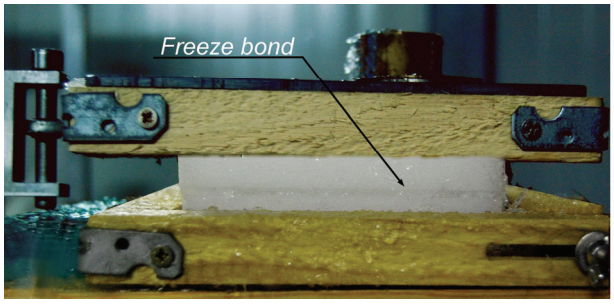

Experimental setup (A.H.V. Repetto-Llamazares, personal communication, 2009)

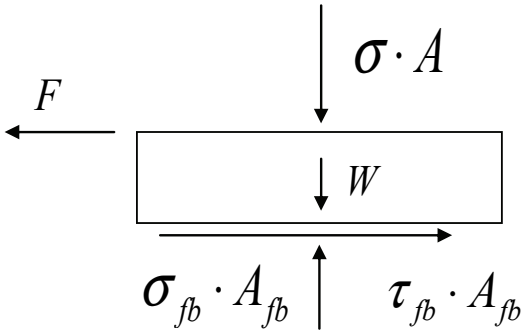

A scheme of loads, acting on the upper piece of the tested ice sample.

APPENDIX B

B - Estimated Parameters

Table B - Estimated parameters. Start time of the failure process (t_{sf}); failure time (t_f); approximated loading slope *(S')*; post-peak force measured after one second of the peak occurrence *(F1)*; area under the loading curve (A); approximated area under the loading curve (aprx(A)).

test	file	failure force, (N)	t_{sf}, (s)	t_f, (s)	(t_f-t_{sf}), (s)	S', (N/s)	F1, (N)	type failure	post-peak	A, (N*s)	aprx(A), (N*s)	|A-aprx(A)|, (N*s)	# slope change
	13_7_1	50.68	52.5	53.58	1.08	46.93	20	saw (3)	roof	15.39	27.37	11.98	2
	13_7_2	31.24	14.66	15.8	1.14	27.40	15	saw (3)	roof	18.22	17.81	0.41	3
	13_7_3	16.21	390.62	393.36	2.74	5.92	13	saw (3)	roof	23.08	22.21	0.87	5
	13_7_4	213.84	14.11	17.53	3.42	62.53	13	saw (3)	drop	357.37	365.67	8.30	4
	23_7_1	52.08	18.32	19.79	1.47	35.43	27	saw (3)	roof	33.33	38.28	4.95	1;2
	23_7_3_jump	174.36	159.28	162.62	3.34	52.20	21	saw(1)	drop	301.91	291.18	10.73	6
	23_7_3	192.16	991	993.39	2.39	80.40	24	saw(3)	drop	201.52	229.63	28.11	4
10110													
	buoy_1	39.99	13.27	16	2.73	14.65	15	saw(2)	roof	35.64	54.59	18.95	5
	buoy_2	18.57	298.07	298.71	0.64	29.02	9	saw(3)	roof	5.54	5.94	0.40	1;2
	buoy_3	31.28	378.17	379.59	1.42	22.03	15	saw(3)	roof	21.15	22.21	1.06	4
	buoy_4	15.1	522.3	523.74	1.44	10.49	9	saw(3)	roof	9.3	10.87	1.57	4
					0								
	7_4_1	46.84	1396.28	1397.75	1.47	31.86	28	saw(1)	roof	31.47	34.43	2.96	4
	7_4_2_jump	84.2	13.63	16.57	2.94	28.64	20	saw(mix)	drop	117.53	123.77	6.24	1;3
	7_4_3	47.46	7.29	10.32	3.03	15.66	31	saw(1)	roof	59.17	71.90	12.73	5
	13_17_1	98.51	8.22	14.59	6.37	15.46	15	saw(1)+line	drop	311.78	313.75	1.97	4
	13_17_2	26.86	23.71	27.03	3.32	8.09	18	saw(1)	roof	35.85	44.59	8.74	3/drop
	13_17_3	24.08	19.02	20.98	1.96	12.29	17	saw(1)	roof	25.01	23.60	1.41	8
	23_17_1	205.68	16.97	22.21	5.24	39.25	22	saw(1)	drop	498.23	538.88	40.65	1;2
10120	23_17_2	117.36	16.14	17.8	1.66	70.70	24	saw(1)	drop	85.77	97.41	11.64	1;2
	buoy_17_1	18.04	29.81	32.79	2.98	6.05	15	saw(1)	roof(flat)	17.89	26.88	8.99	3/drop
	14_4kg_1	38.44	808.59	809.85	1.26	30.51	22	saw(1)	roof	27.37	24.22	3.15	4
	14_4kg_2	48.17	182.41	184.23	1.82	26.47	33	saw(3)	roof	35.13	43.83	8.70	5
	1_13kg_1	24.3	225.28	226.8	1.52	15.99	13	saw(1)	roof	13.79	18.47	4.68	1;2
	1_13kg_2	45.48	416.94	419.98	3.04	14.96	20	saw(1)	roof	43.88	69.13	25.25	4
	1_13kg_3	34.73	271.49	274.17	2.68	12.96	20	saw(1)	roof	28.17	46.54	18.37	8
	1_300gr_1	51.71	239.33	244.27	4.94	10.47	12	saw(1)mix	drop	150.89	127.72	23.17	5strange
	1_300gr_2	23.74	465.88	467.47	1.59	14.93	11	line	roof	15.8	18.87	3.07	4
	1_300gr_3	35.88	199.32	201.26	1.94	18.49	13	line	roof	28.56	34.80	6.24	3
10130													
	1_4kg_1	42.1	262.24	265.06	2.82	14.93	27	saw(1)	roof	47.81	59.36	11.55	1;3
	1_4kg_2	40.21	259.84	261.96	2.12	18.97	29	saw(1)	roof	43.96	42.62	1.34	1;2
	1_4kg_3	63.68	29.74	33.98	4.24	15.02	24	saw(1)	rop (smal	85.09	135.00	49.91	3
	1_buoy_1	51.9	1438.14	1439.54	1.4	37.07	11	saw(1)	drop(small	22.52	36.33	13.81	2
	1_buoy_2	53.07	196.49	200.85	4.36	12.17	11	saw(1)	drop	63.81	115.69	51.88	7
	1_buoy_3	24.22	169.66	171.3	1.64	14.77	11	saw(1)	roof	15.07	19.86	4.79	4
	7_1h_13_1	26.72	459.7	461.39	1.69	15.81	14	saw(1)	roof	20.95	22.58	1.63	4
	7_1h_13_2	61.36	137.53	139.63	2.1	29.22	19	saw(3)	roof	36.84	64.43	27.59	4
	7_1h_13_3	85.78	234.24	236.25	2.01	42.68	25	saw(3)	roof	59.16	86.21	27.05	5
	7_4h_13_1	30.59	463.36	464.34	0.98	31.21	13	saw(3)	roof	16.29	14.99	1.30	3
	7_4h_13_2	37.71	228.68	230.6	1.92	19.64	21	saw(1)	roof	32.65	36.20	3.55	3;4
	7_4h_13_3	41.57	261.66	263.28	1.62	25.66	19	saw(1)	roof	18.68	33.67	14.99	6
10210					0								
	7_10h_1	49.79	13.15	20.55	7.4	6.73	15	saw(mix)	drop	114.61	184.22	69.61	5
	7_10h_2	31.35	307.41	309.57	2.16	14.51	14	line	roof	24.8	33.86	9.06	5
	7_10h_3	122.67	108.79	116.19	7.4	16.58	14	line mix	drop	510.44	453.88	56.56	3
					0								
	13_7_1	50.68	52.5	53.58	1.08	46.93	20	saw (3)	roof	15.39	27.37	11.98	2
	13_7_2	31.24	14.66	15.8	1.14	27.40	15	saw (3)	roof	18.22	17.81	0.41	3
	13_7_3	16.21	390.62	393.36	2.74	5.92	13	saw (3)	roof	23.08	22.21	0.87	5
	13_7_4	213.84	14.11	17.53	3.42	62.53	13	saw (3)	drop	357.37	365.67	8.30	4

10220	4h_12_1	32.79	6165.99	6168.72	2.73	12.01	19	line	roof	42.26	44.76	2.50	7strange
	4h_12_2	35.2	14.69	17.19	2.5	14.08	13	line	roof	20.13	44.00	23.87	3
												0.00	
	1h_12_1	43.35	16.83	18.58	1.75	24.77	17	line	drop	26.37	37.93	11.56	3
	1h_12_2	49.95	13.64	16.12	2.48	20.14	28	line	roof	13.87	61.94	48.07	strange
	10h_12_1	32.95	551.81	553.89	2.08	15.84	16	saw(3)	roof	21.36	34.27	12.91	3
	10h_12_2	43.85	292.71	294.96	2.25	19.49	16	saw(3)	roof	33.85	49.33	15.48	3
	10h_12_3	27.77	9.17	11.3	2.13	13.04	13	saw(3)mix	roof	26.3	29.58	3.28	6
	13_17_2	26.86	23.71	27.03	3.32	8.09	18	saw(1)	roof	35.85	44.59	8.74	3/drop
	13_17_3	24.08	19.02	20.98	1.96	12.29	17	saw(1)	roof	25.01	23.60	1.41	8
10410	FB_R3_1	35.95	871.62	873.93	2.31	15.56	18	saw(1)	roof	37.74	41.52	3.78	3
	FB_R3_2	12.55	376.9	379	2.1	5.98	9	saw_mix	roof	12.21	13.18	0.97	5
	FB_R3_3	24.04	267.12	269.26	2.14	11.23	11	saw(1)	roof	32.56	25.72	6.84	5
	FB_R3_4	22.66	332.98	340.11	7.13	3.18	15	saw(1)	roof	56.45	80.78	24.33	6strange
10510	FB_R4_1	21.54	24.71	27.85	3.14	6.86	17	mix	roof	31.83	33.82	1.99	1;3
	FB_R4_2	19.96	451.5	454.65	3.15	6.34	14	mix	roof	17.95	31.44	13.49	2
	FB_R4_3	18	424.04	426.52	2.48	7.26	14	saw(1)	drop	19.7	22.32	2.62	8
	FB_R4_4	44.83	94.32	97.96	3.64	12.32	21	saw(1)	roof	59.91	81.59	21.68	1;3

In Table, term *'roof'* corresponds to the ductile fracture (criterion (i)), and *'drop'* to the brittle fracture (criterion (i)). Distinction between the *'roof'* and *'drop'* made by visual observations.

Appendix

C

C1 - Power-Law Fit

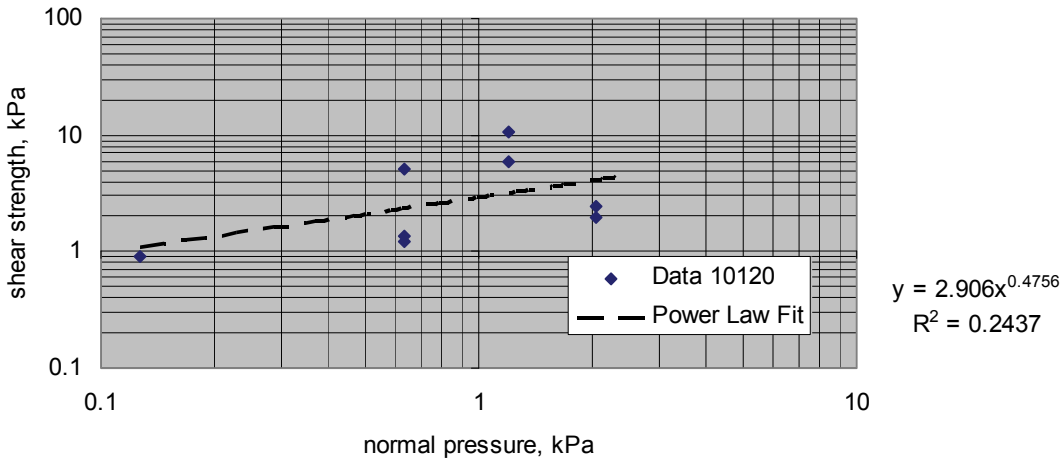

Figure C1 - Log-log plot of the freeze-bond shear strength as a function of normal pressure.

C2 - Post-failure Behavior

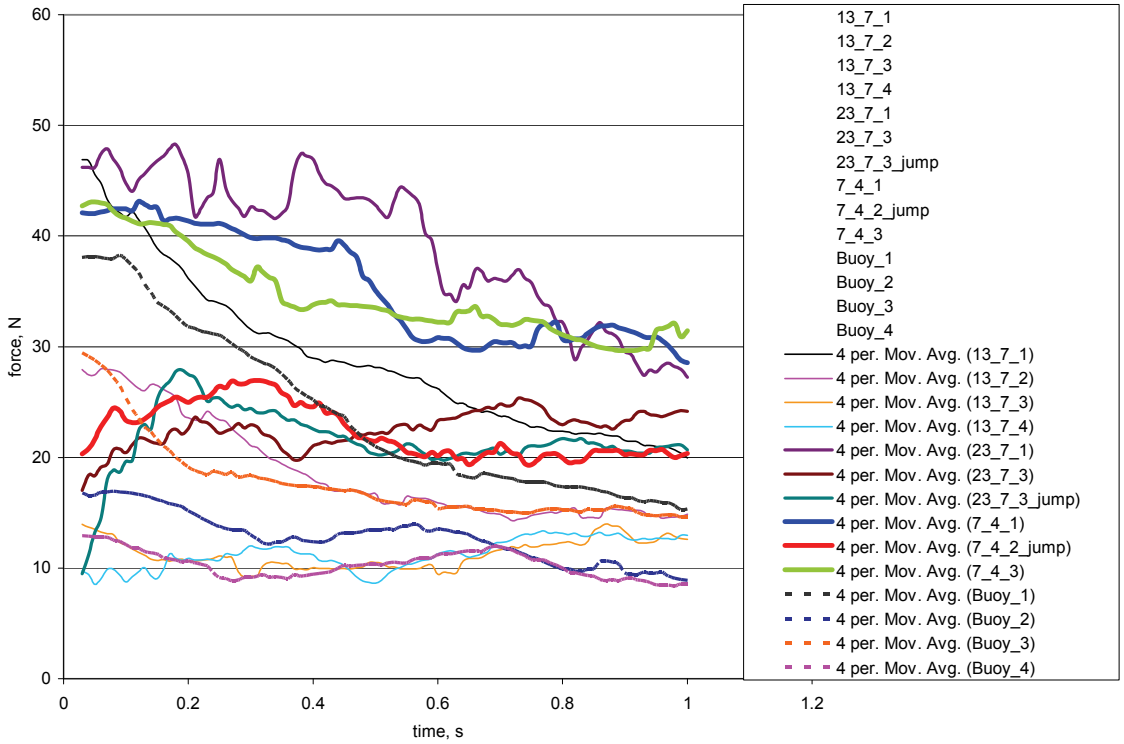

Figure C2- Force history - Test 10110.

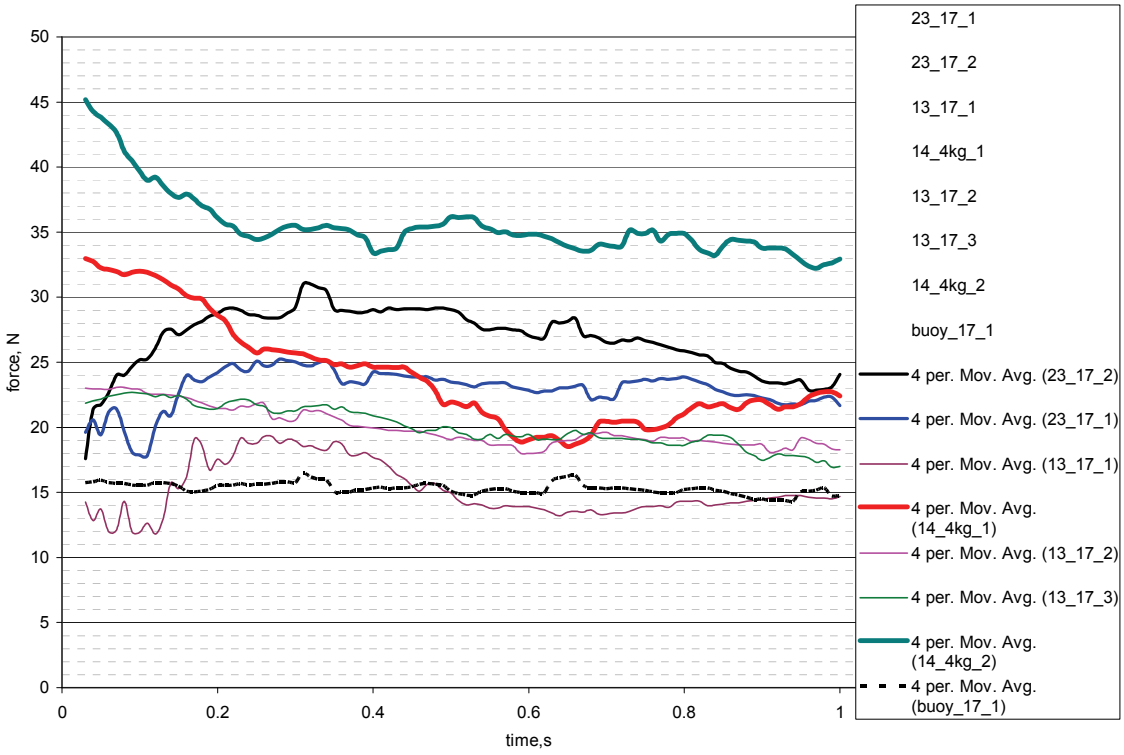

Figure C3 - Force history - Test 10120.

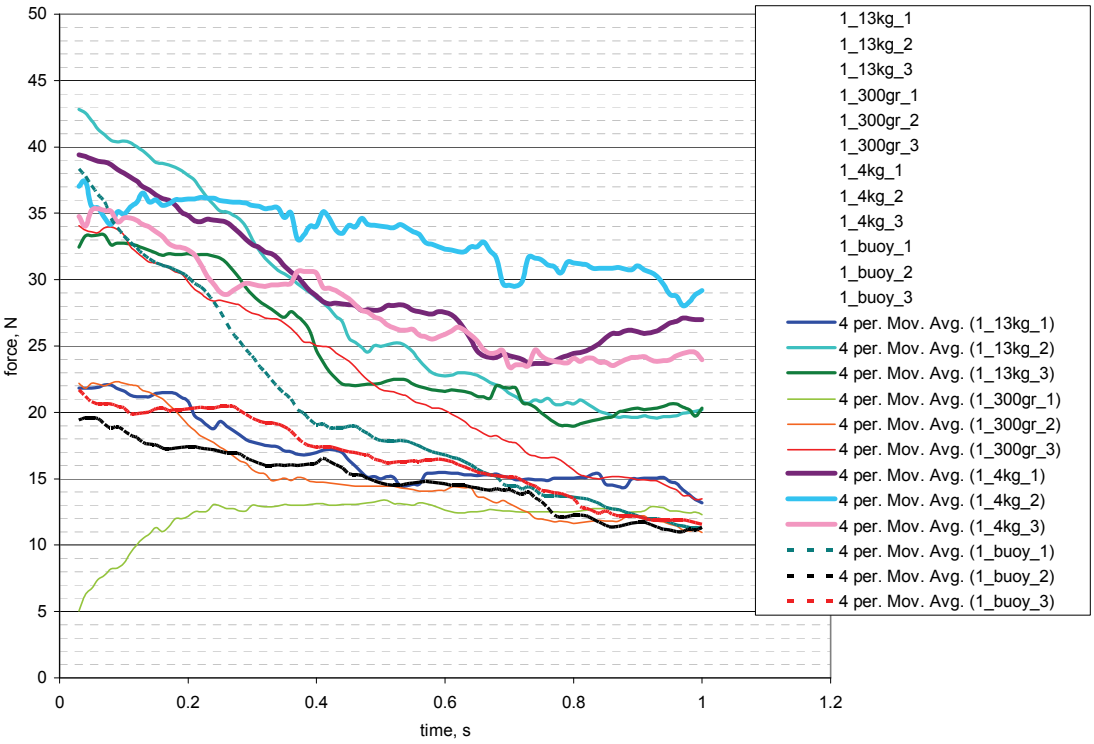

Figure C4 - Force history - Test 10130.

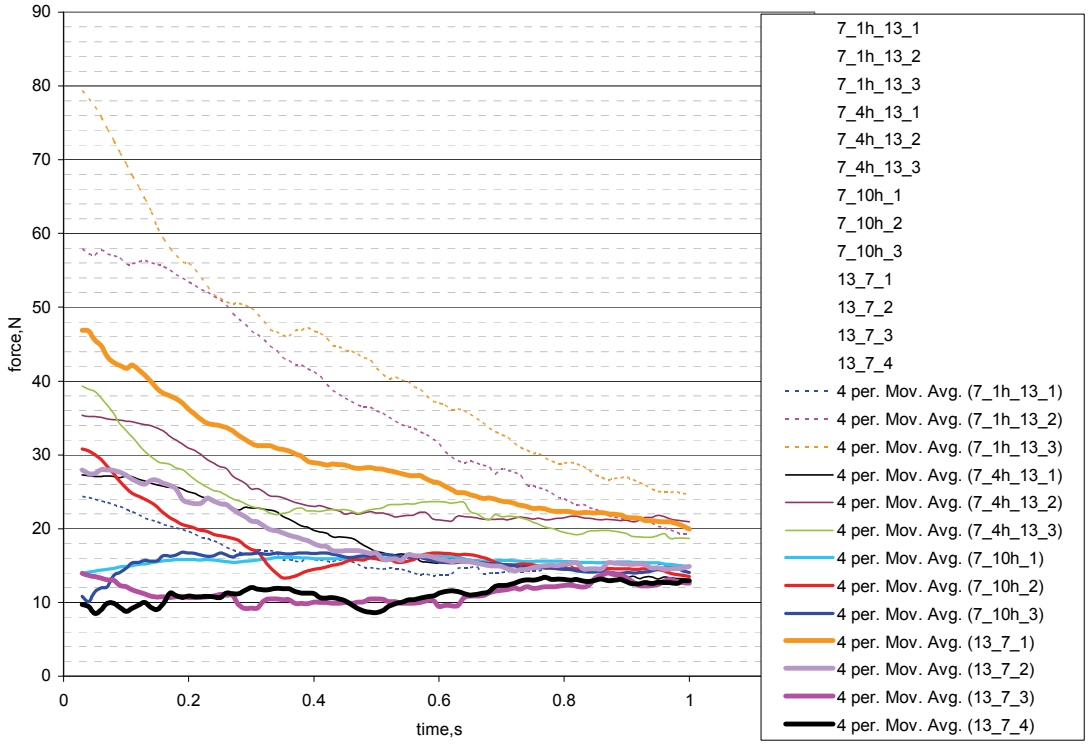

Figure C5 - Force history - Test 10210.

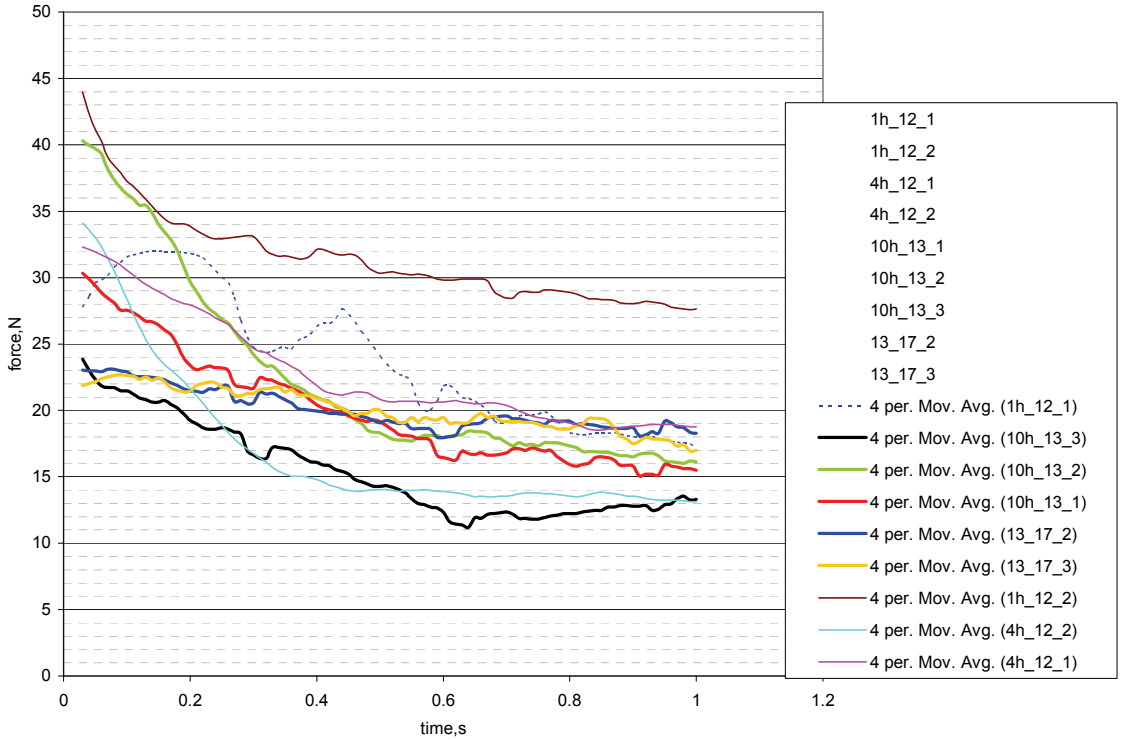

Figure C6 - Force history - Test 10220.

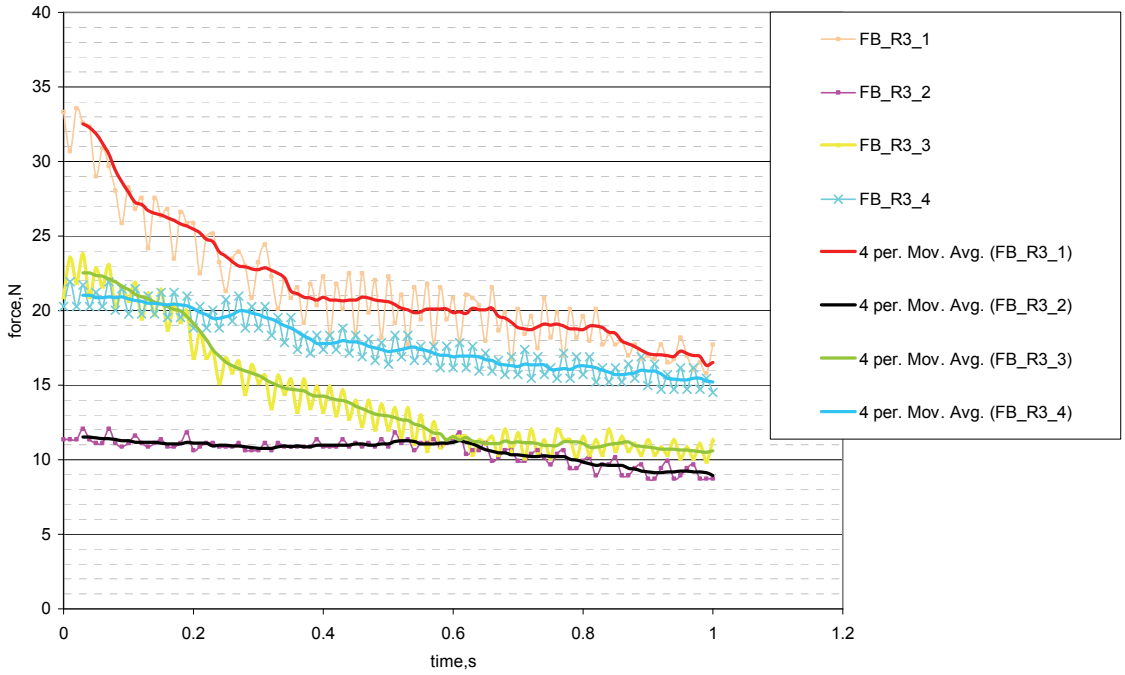

Figure C7 - Force history - Test 10410.

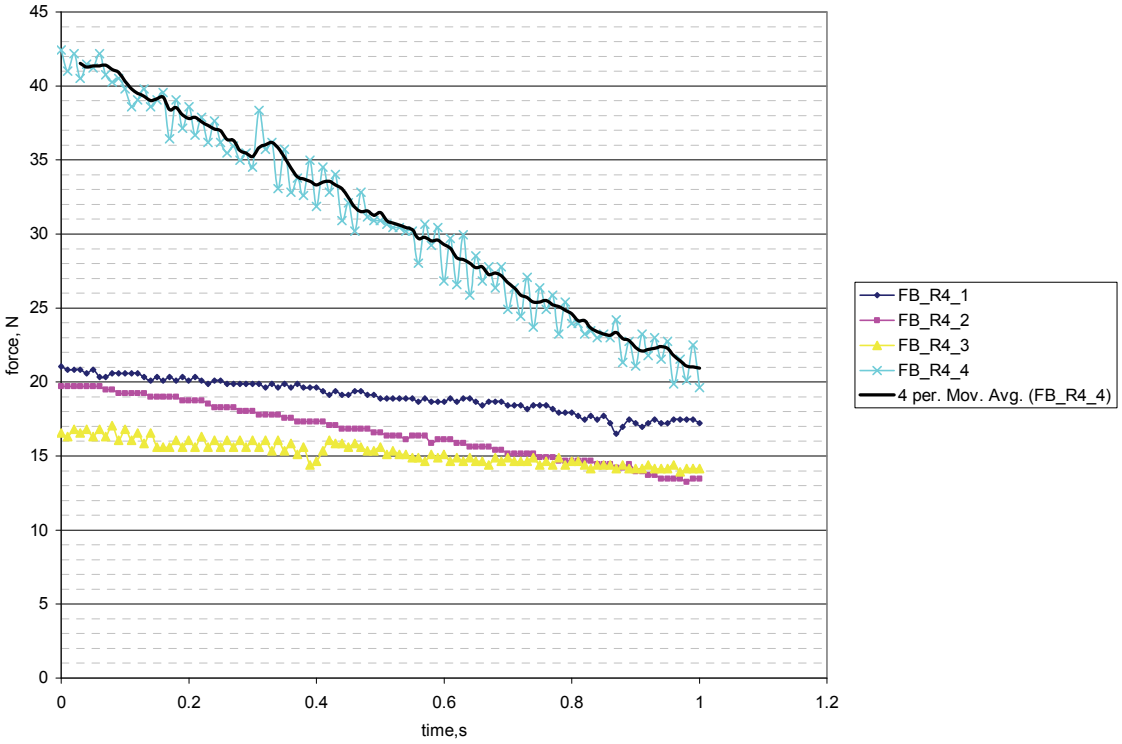

Figure C8 - Force history - Test 10510.

Appendix D

D1 - Cohesive Element Verification

From previous verification tests (ABAQUS, Verification manual) on cohesive-element kinematics it is known that: (i) the response of two-dimensional cohesive elements for the deformation in the pure normal and the pure shear mode matches analytical results; (ii) degradation of the response of a cohesive element begins when specified damage initiation criterion is met. The damage variable evolves according to the evolution law specified in terms of displacements or energy dissipation.

Figure D1.1 shows a simple two element model which was based on the model in Feih (2005). The difference between the model in Feih (2005) and in this study is that instead of verification of UEL user subroutine, a performance of ABAQUS version 6.8 was tested in modeling of cohesive laws in composite strictures.

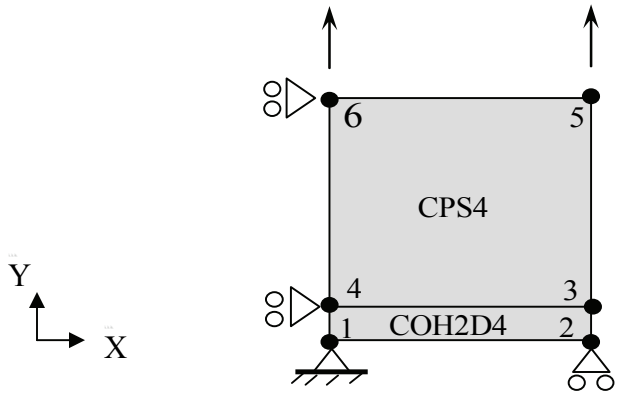

Figure D1.1 - Verification model, where COH2D4 is a four-node, two-dimensional cohesive element; CPS4 is a four-node bilinear plane stress element.

The nodes 1-4 initially coincide in their position; in Figure D1.1 they are plotted apart for a better understanding of the node numbering.

The input file for the two-element model (Figure D1.1) is given below. The elements is under plane-stress condition (element, type=CPS4) and the material is linear elastic (elastic, type=ISOTROPIC).

```
*HEADING
 Cohesive Element Test - COH2D4
*NODE
1,0.0,0.0
2,1.0,0.0
3,1.0,0.0
4,0.0,0.0
5,0.0,1.0
6,1.0,1.0
*NSET,NSET=ALL
5
*ELEMENT,TYPE=COH2D4,ELSET=ALL
1,1,2,3,4
*ELEMENT,TYPE=CPS4,ELSET=eall
2,4,3,6,5
*SOLID SECTION,elset=eall,material =mat1
*MATERIAL,NAME=MAT1
*ELASTIC,TYPE=ISOTROPIC
5E9,0.3
*COHESIVE SECTION,elset=all,material=mat2,response=traction separation,stack direction=2
*MATERIAL, NAME=MAT2
*ELASTIC, type=traction
1.0e05,1.0e05,1.0e05
*DENSITY
100.0,
*DAMAGE INITIATION, CRITERION=MAXS
35E3,35E4
*DAMAGE EVOLUTION, TYPE=DISPLACEMENT, SOFTENING=LINEAR
1.05
** apply boundary conditions
*BOUNDARY
1, 1, 2
2, 2, 2
4, 1, 1
5, 1, 1
** history data
*STEP, NLGEOM
*STATIC
0.01, 1.0,,0.01
*CONTROLS, PARAMETERS=TIME INCREMENTATION
7, 10, 9, 16, 10, 4, 20, 10, 6
*BOUNDARY
5, 2, 2, 1.0
6, 2, 2, 1.0
*OUTPUT, FIELD,FREQ=1
*ELEMENT OUTPUT
S,
E,
*NODE OUTPUT
U,
RF,
*OUTPUT,HISTORY,FREQ=1
*NODE OUTPUT,NSET=ALL
U2,
RF2
*END STEP
```

Figure D1.2 shows results created by ABAQUS/CAE. As the stiffness of the top element is large compared to the input stiffness of cohesive element the stress distribution in loading direction appears constant (Figure D1.2a). The displacement field in the X-direction, which is caused by Poisson effect, varies linearly (Figure D1.2b). The original TSL is obtained from the reaction forces and nodal displacements (Figure D1.2c).

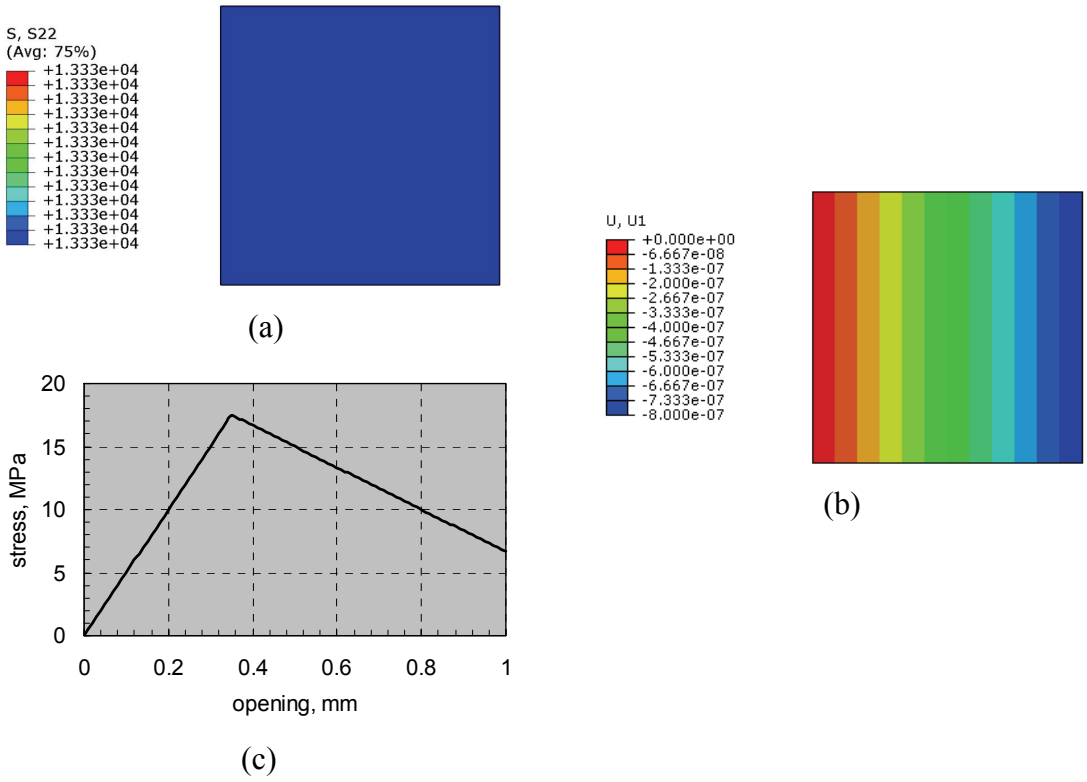

Figure D1.2– Results created by ABAQUS/CAE: S22 are normal stresses acting in loading direction (Y-direction); U1 are displacements in the X-direction.

D2 - Input Files

```
*HEADING
 Shear test for COHESIVE BEHAVIOR
**************************
**TEST CASE II: SIMPLE SHEAR (MODE 2)
**************************
*NODE, NSET=SPEC1_MODE2
21, 0., 0., 0.
22, 0.14, 0., 0.
23, 0.14, 0., 0.14
24, 0., 0., 0.14
25, 0., 0.03, 0.
26, 0.14, 0.03, 0.
27, 0.14, 0.03, 0.14
28, 0., 0.03, 0.14
121,0., 0.03, 0.
122, 0.14, 0.03, 0.
123, 0.14, 0.03, 0.14
124, 0., 0.03, 0.14
125, 0., 0.06, 0.
126, 0.14, 0.06, 0.
127, 0.14, 0.06, 0.14
128, 0., 0.06, 0.14
*NSET, NSET=SPEC1_MODE2_TOP
125, 126, 127, 128
*NSET, NSET=SPEC1_MODE2_BOT
21, 22, 23, 24
*ELEMENT, TYPE=C3D8,
ELSET=SPEC1_MODE2
21, 21, 24, 23, 22, 25, 28, 27, 26
121, 121, 124, 123, 122, 125, 128, 127, 126
*ELSET, ELSET=EALL_DISP
SPEC1_MODE2
*SURFACE, NAME=SPEC1_MODE2_SURF1
21,S2
*SURFACE, NAME=SPEC1_MODE2_SURF2
121,S1
**
*SURFACE INTERACTION,NAME=COH_DISP
*COHESIVE BEHAVIOR
2.9E6,2.9E6,2.9E6
*DAMAGE INITIATION, CRITERION=QUADS
10.5e3, 10.5e3, 10.5e3
*DAMAGE EVOLUTION, TYPE=ENERGY,
MIXED MODE BEHAVIOR=POWER LAW,
POWER=1, SOFTENING=LINEAR
24, 24, 24
*SOLID SECTION, ELSET=EALL_DISP,
MATERIAL=MAT
*MATERIAL, NAME=MAT
*ELASTIC
200e6,0.3
*DENSITY
810.
*NSET, NSET=NALL_BOT
```

```
*HEADING
Shear test simulation one COH3D8 and two solids
C3D8
**************************
**TEST CASE SIMPLE SHEAR
**************************
*NODE, NSET=SPEC1_MODE2
21, 0., 0., 0.
22, 0.14, 0., 0.
23, 0.14, 0., 0.14
24, 0., 0., 0.14
25, 0., 0.03, 0.
26, 0.14, 0.03, 0.
27, 0.14, 0.03, 0.14
28, 0., 0.03, 0.14
121,0., 0.03, 0.
122, 0.14, 0.03, 0.
123, 0.14, 0.03, 0.14
124, 0., 0.03, 0.14
125, 0., 0.06, 0.
126, 0.14, 0.06, 0.
127, 0.14, 0.06, 0.14
128, 0., 0.06, 0.14
*NSET, NSET=SPEC1_MODE2_TOP
125, 126, 127, 128
*NSET, NSET=SPEC1_MODE2_BOT
21, 22, 23, 24
*NSET, NSET=SPEC1_MODE2_TOP_SIDE
122, 123, 127, 126
*ELEMENT, TYPE=C3D8,
ELSET=SPEC1_MODE2
21, 21, 22, 26, 25, 24, 23, 27, 28
121, 121, 122, 126, 125, 124, 123, 127, 128
*ELEMENT,TYPE=COH3D8,ELSET=ALL
25, 25, 26, 122, 121, 28, 27, 123, 124
*SOLID SECTION,elset=spec1_mode2,material
=ice
*MATERIAL,NAME=ICE
*ELASTIC,TYPE=ISOTROPIC
200e6,0.3
*DENSITY
810
*COHESIVE
SECTION,elset=all,material=fb,response=traction
separation,stack direction=2
*MATERIAL, NAME=fb
*ELASTIC, type=traction
2.9e6,2.9e6,2.9e6
*DENSITY
810
*DAMAGE INITIATION, CRITERION=QUADS
10.5E3,10.5E3,10.5e3
*DAMAGE EVOLUTION, TYPE=ENERGY,
SOFTENING=LINEAR, MIXED MODE
```

```
SPEC1_MODE2_BOT
*BOUNDARY
NALL_BOT, 1, 3
SPEC1_MODE2_TOP, 2, 3
*ELSET, ELSET=QA_TEST_EALL
EALL_DISP
*NSET, NSET=QA_TEST_NALL
 SPEC1_MODE2
**##################################
######
**DYNAMIC, EXPLICIT  STEP
**##################################
######
*AMPLITUDE,NAME=AMP,DEFINITION=TABU
LAR
0.0,0.0,1.0,1.0
*STEP
*DYNAMIC, EXPLICIT
, 1.0
*BOUNDARY, TYPE=DISPLACEMENT,
AMPLITUDE=AMP
SPEC1_MODE2_TOP, 1, 1, 0.7e-3
*CONTACT
*CONTACT INCLUSIONS
SPEC1_MODE2_SURF1,SPEC1_MODE2_SURF2
*CONTACT PROPERTY ASSIGNMENT
SPEC1_MODE2_SURF1,SPEC1_MODE2_SURF2,C
OH_DISP
*OUTPUT, FIELD, TIME INTERVAL=0.01
***OUTPUT, FIELD, NUMBER INTERVAL=200,
TIME MARKS=YES
*ELEMENT OUTPUT
S,
E,
*NODE OUTPUT, NSET=QA_TEST_NALL
U,
*CONTACT OUTPUT
CSDMG,CSMAXUCRT
**CFORCE,CSTRESS
*OUTPUT, HISTORY, TIME INTERVAL=0.01
*ENERGY OUTPUT
ETOTAL, ALLWK
*OUTPUT, HISTORY, TIME INTERVAL=0.01
*NODE OUTPUT,NSET=SPEC1_MODE2_TOP
U1,
RF1
*CONTACT OUTPUT,
SURFACE=SPEC1_MODE2_SURF1
CFT,
*END STEP
```

```
BEHAVIOR=POWER LAW, POWER=1
24, 24, 24
*BOUNDARY
SPEC1_MODE2_BOT, 1, 3
SPEC1_MODE2_TOP, 2, 3
*AMPLITUDE,NAME=AMP,DEFINITION=TAB
ULAR
0.0,0.0,1.0,1.0
*STEP
*DYNAMIC, EXPLICIT
, 1.0
*BOUNDARY, TYPE=DISPLACEMENT,
AMPLITUDE=AMP
SPEC1_MODE2_TOP, 1, 1, 0.7e-3
*OUTPUT, FIELD, TIME INTERVAL=0.01
*ELEMENT OUTPUT
S,
E,
*NODE OUTPUT
U,
RF,
*OUTPUT,HISTORY,TIME INTERVAL=0.01
*NODE OUTPUT,NSET=SPEC1_MODE2_TOP
U1,
RF1
*END STEP
```

Appendix E

E - Scheme for Predicting Ice Loads on Structure

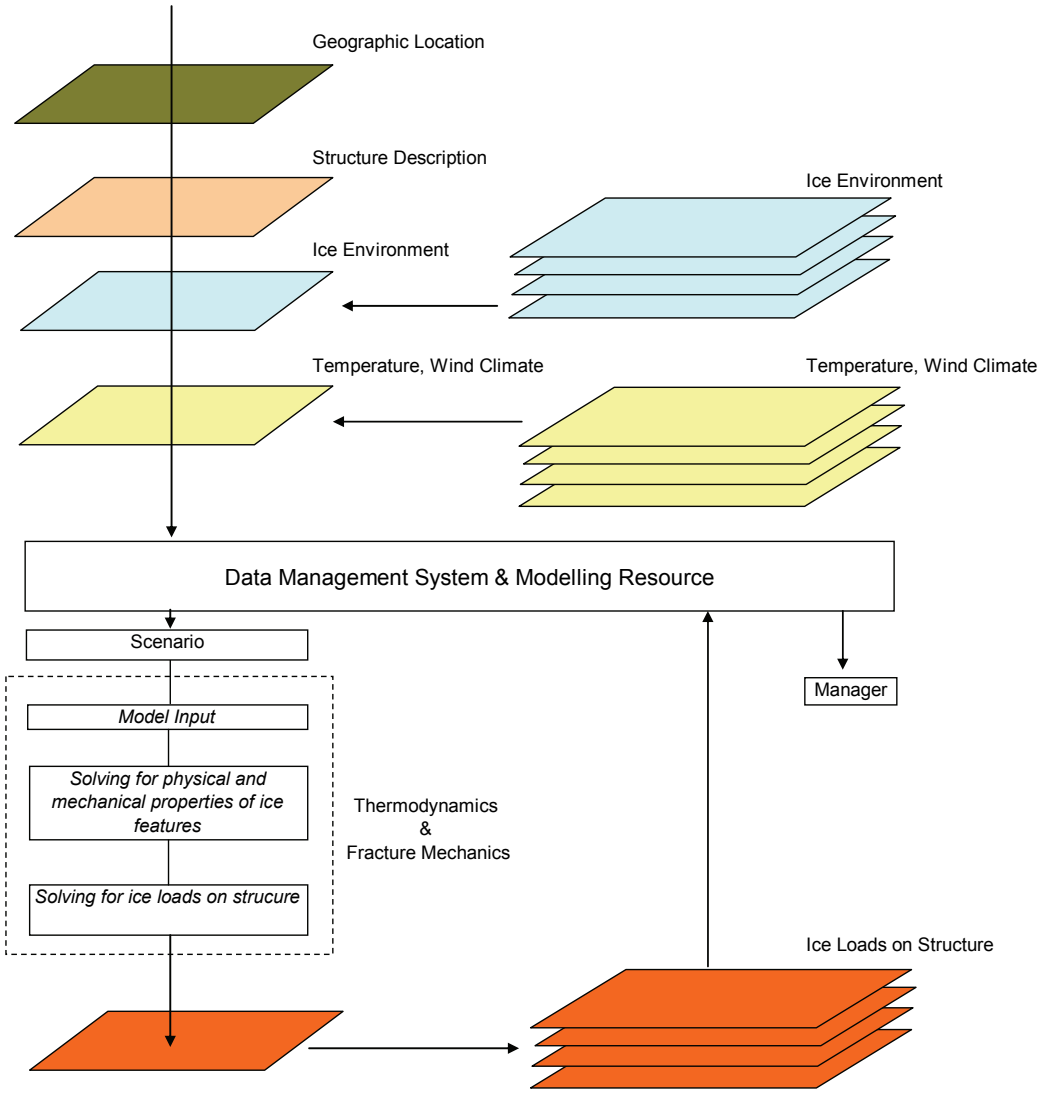

The idea was taken from Collins and Amos (2008).

Appendix F

F - Data Normality Test

Normal Probability Plot (NPP) method was used in order to check if data sets of *F1* and *U* are approximately normally distributed. NPPs of *F1* and *U* are shown in Figures F1 and F2 respectively. NPPs of *U* and R_s for ductile samples (criteria (i) and (ii)) are given in Figures F3 and F4 respectively. Data was plotted against a theoretical normal distribution in MATLAB (*normplot* command) in such way that the points should form an approximate straight line. Any departures from this straight line indicate departures from normality.

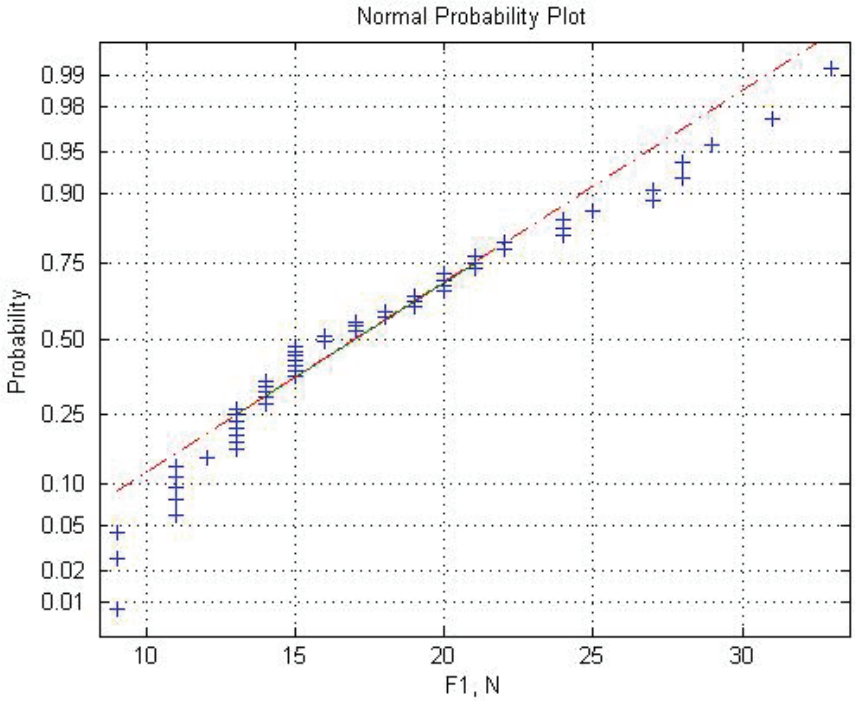

Figure F1 - Normal probability plot of force *(F1)* measured at the end of the first second after failure.

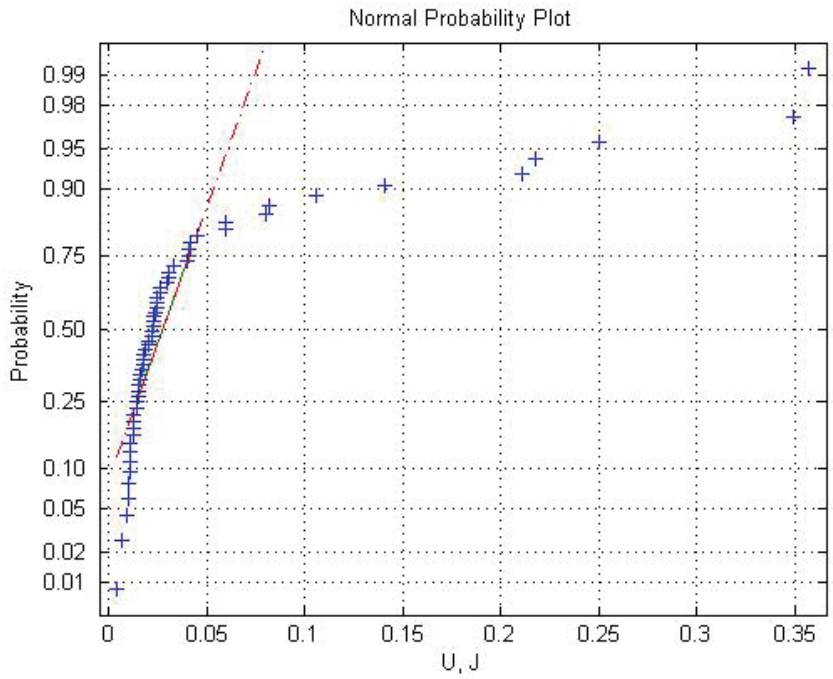

Figure F2 - Normal probability plot of energy input to the system *(U)*.

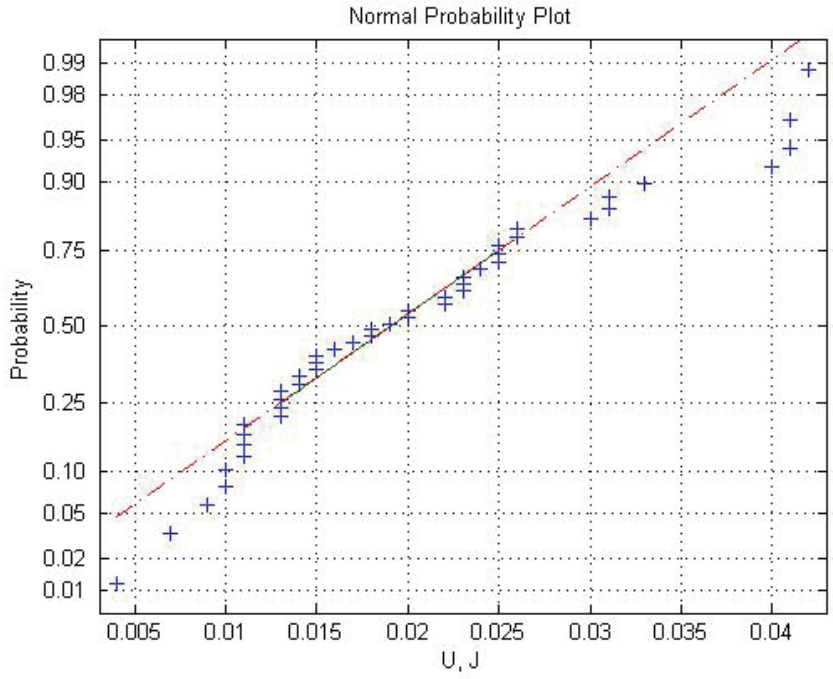

Figure F3 - Normal probability plot of energy input to the system *(U)* for ductile samples.

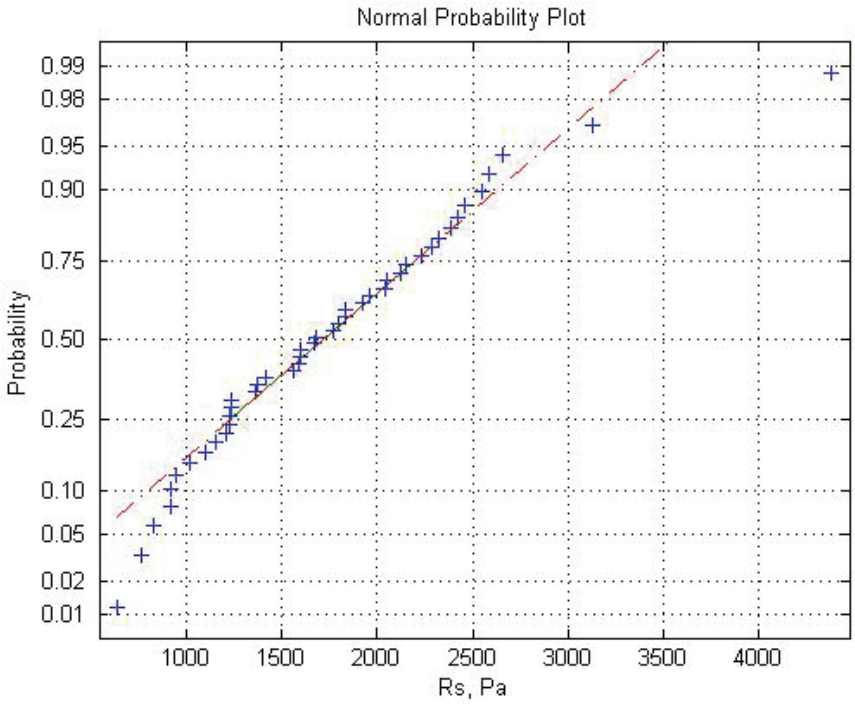

Figure F4 - Normal probability plot of freeze-bond shear capacity *(R_s)* for ductile samples based on criteria (i) and (ii).

In the plots from Figure F1 to F4 the plus signs show the empirical probability (vertical axis) versus the data value (horizontal axis) for each point in the data set. The solid line connects the 25th and 75th percentiles of the data and represents a linear fit. The dashed line extends the solid line to the ends of the sample. The scale of the vertical axis is not uniform (see MATLAB Documentation).

From the above plots the following conclusions can be made:

1. The NPPs of *F1* and *U*, R_s for ductile samples (Figure F1 and Figure F3, Figure F4 respectively) show a reasonably linear pattern in the center of data. However, tails, particularly the tails in Figure F4, show departures from the fitted line. Perhaps the distribution other than the normal distribution should be used for these data.

2. The NPP of *U* for the complete set of measurements (Figure F2) shows a strongly nonlinear pattern, therefore, the distribution of *U* is not normal.

NTNU
Innovation and Creativity